Electrochemical to Mechanical Energy Conversion

by

Timothy Edward Chin

B.S. Materials Science and Engineering
University of Washington, 2003

M.S. Materials Science and Engineering
University of Washington, 2004

MASSACHUSETTS INSTITUTE OF TECHNOLOGY
[redacted]
LIBRARIES

ARCHIVES

SUBMITTED TO THE DEPARTMENT OF MATERIALS SCIENCE AND ENGINEERING IN PARTIAL FULFILLMENT OF THE REQUIREMENTS FOR THE DEGREE OF

DOCTOR OF PHILOSOPHY IN MATERIALS SCIENCE AND ENGINEERING
AT THE
MASSACHUSETTS INSTITUTE OF TECHNOLOGY

FEBRUARY 2010

MASSACHUSETTS INSTITUTE OF TECHNOLOGY
JAN 0 3 2011
LIBRARIES

©2010 Massachusetts Institute of Technology. All Rights Reserved.

Signature of Author:_____
Department of Materials Science and Engineering
January 8, 2010

Certified By:_____
Yet-Ming Chiang
Kyocera Professor of Ceramics
Thesis Supervisor

Accepted By:_____
Christine Ortiz
Associate Professor of Materials Science and Engineering
Chairman, Committee for Graduate Students

Report Documentation Page

Form Approved
OMB No. 0704-0188

Public reporting burden for the collection of information is estimated to average 1 hour per response, including the time for reviewing instructions, searching existing data sources, gathering and maintaining the data needed, and completing and reviewing the collection of information. Send comments regarding this burden estimate or any other aspect of this collection of information, including suggestions for reducing this burden, to Washington Headquarters Services, Directorate for Information Operations and Reports, 1215 Jefferson Davis Highway, Suite 1204, Arlington VA 22202-4302. Respondents should be aware that notwithstanding any other provision of law, no person shall be subject to a penalty for failing to comply with a collection of information if it does not display a currently valid OMB control number.

1. REPORT DATE	2. REPORT TYPE	3. DATES COVERED
FEB 2010		**00-00-2010 to 00-00-2010**

4. TITLE AND SUBTITLE	5a. CONTRACT NUMBER
Electrochemical to Mechanical Energy Conversion	5b. GRANT NUMBER
	5c. PROGRAM ELEMENT NUMBER
6. AUTHOR(S)	5d. PROJECT NUMBER
	5e. TASK NUMBER
	5f. WORK UNIT NUMBER
7. PERFORMING ORGANIZATION NAME(S) AND ADDRESS(ES) **Massachusetts Institute of Technology,77 Massachusetts Avenue,Cambridge,MA,02139**	8. PERFORMING ORGANIZATION REPORT NUMBER
9. SPONSORING/MONITORING AGENCY NAME(S) AND ADDRESS(ES)	10. SPONSOR/MONITOR'S ACRONYM(S)
	11. SPONSOR/MONITOR'S REPORT NUMBER(S)

12. DISTRIBUTION/AVAILABILITY STATEMENT
Approved for public release; distribution unlimited

13. SUPPLEMENTARY NOTES

14. ABSTRACT

Electrode materials for rechargeable lithium ion batteries are well-known to undergo significant dimensional changes during lithium-ion insertion and extraction. In the battery community, this has often been looked upon negatively as a degradation mechanism. However, the crystallographic strains are large enough to warrant investigation for use as actuators. Lithium battery electrode materials lend themselves to two separate types of actuators. On one hand, intercalation oxides and graphite provide moderate strains, on the order of a few percent, with moderate bandwidth (frequency). Lithium intercalation of graphite can achieve actuation energy densities of 6700 kJ m-3 with strains up to 6.7%. Intercalation oxides provide strains on the order of a couple percent, but allow for increased bandwidth. Using a conventional stacked electrode design, a cell consisting of lithium iron phosphate (LiFePO4) and carbon achieved 1.2% strain with a mechanical power output of 1000 W m 3 . Metals, on the other hand, provide colossal strains (hundreds of percent) upon lithium alloying, but do not cycle well. Instead, a self-amplifying device was designed to provide continuous, prolonged, one-way actuation over longer time scales. This was still able to achieve an energy density of 1700 kJ n 3, significantly greater than other actuation technologies such as shape-memory alloys and conducting polymers, with displacements approaching 10 mm from a 1 mm thick disc. Further, by using lithium metal as the counterelectrode in an electrochemical couple, these actuation devices can be selfpowered mechanical energy and electrical energy can be extracted simultaneously.

15. SUBJECT TERMS

16. SECURITY CLASSIFICATION OF:			17. LIMITATION OF ABSTRACT	18. NUMBER OF PAGES	19a. NAME OF RESPONSIBLE PERSON
a. REPORT	b. ABSTRACT	c. THIS PAGE			
unclassified	**unclassified**	**unclassified**	**Same as Report (SAR)**	**153**	

Electrochemical to Mechanical Energy Conversion

by

Timothy Edward Chin

Submitted to the Department of Materials Science and Engineering on January 14, 2010 in Partial Fulfillment of the Requirements for the Degree of Doctor of Philosophy in Materials Science and Engineering

ABSTRACT

Electrode materials for rechargeable lithium ion batteries are well-known to undergo significant dimensional changes during lithium-ion insertion and extraction. In the battery community, this has often been looked upon negatively as a degradation mechanism. However, the crystallographic strains are large enough to warrant investigation for use as actuators. Lithium battery electrode materials lend themselves to two separate types of actuators. On one hand, intercalation oxides and graphite provide moderate strains, on the order of a few percent, with moderate bandwidth (frequency). Lithium intercalation of graphite can achieve actuation energy densities of 6700 kJ m^{-3} with strains up to 6.7%. Intercalation oxides provide strains on the order of a couple percent, but allow for increased bandwidth. Using a conventional stacked electrode design, a cell consisting of lithium iron phosphate ($LiFePO_4$) and carbon achieved 1.2% strain with a mechanical power output of 1000 W m^{-3}.

Metals, on the other hand, provide colossal strains (hundreds of percent) upon lithium alloying, but do not cycle well. Instead, a self-amplifying device was designed to provide continuous, prolonged, one-way actuation over longer time scales. This was still able to achieve an energy density of 1700 kJ m^{-3}, significantly greater than other actuation technologies such as shape-memory alloys and conducting polymers, with displacements approaching 10 mm from a 1 mm thick disc. Further, by using lithium metal as the counterelectrode in an electrochemical couple, these actuation devices can be self-powered: mechanical energy and electrical energy can be extracted simultaneously.

Thesis Supervisor: Yet-Ming Chiang
Title: Kyocera Professor of Ceramics

Acknowledgements

First and foremost, this thesis would not have been possible without the support and guidance from my advisor, Professor Yet-Ming Chiang. Fruitful discussions and directions were also provided from my other committee members, Professor Michael Cima and Professor Chris Schuh, Rick Gyory at Entra Pharmaceuticals, and Prof. Esther Takeuchi at the University of Buffalo.

Much of the work has been shared amongst and contributed to by other postdoctoral associates, visiting students, and graduate students. Contributing to the early work of this thesis were Dr. Yukinori Koyama, Urs Rhyner, Dimitrios Sapnaras, Georg Baetz, Dr. Eva Jud Sierra, and Fernando Tubilla Kuri. Later work was assisted by Dr. Malinda Tupper, Bryan Gortikov, Lenny Rigione, and Alex Pizzochero.

I would also like to thank funding from the National Science Foundation Graduate Research Fellowship Program, Defense Advanced Research Projects Agency, and the Deshpande Center

Table of Contents

List of Figures 9
List of Tables 15
1 Introduction / Motivation 13
1.1 Materials Selection 14
1.2 Electrochemical Cells 17
1.3 Actuators 20
1.4 Thermodynamics 23
1.5 Electrochemical Actuation in Literature 24
1.6 Thesis Scope and Organization 25
1.7 References 26
2 Electrochemical Actuation of Lithium Rechargeable Batteries 29
2.1 Electrochemical Actuation via Intercalation in Literature 29
2.2 Battery Construction 30
2.2.1 Materials 30
2.2.2 Construction 31
2.3 Methodology 31
2.3.1 Battery Types 31
2.3.2 Testing Equipment and Setup 32
2.4 Results and Discussion 33
2.4.1 Volume Changes Under Zero Stress 33
2.4.2 Linear Dimension Changes Under Zero Stress 34
2.4.3 Passive Mechanical Response of Commercial Batteries 35
2.4.4 Linear Dimension Changes Under Applied Stress 37
2.5 Summary 42
2.6 References 43
3 Designing Electrochemical Actuators Based on Lithium Rechargeable Batteries .. 44
3.1 Highly Oriented Pyrolytic Graphite Microactuators 44
3.1.1 Materials and Methods 45
3.1.2 Results and Discussion 46
3.2 Calendared Electrodes 51
3.2.1 Materials and Methods 51
3.2.2 Results and Discussion 53
3.3 High-rate Actuation 56
3.3.1 Materials and Methods 56
3.3.2 Results and Discussion 57
3.4 Summary 60
3.5 References 61
4 Actuation Based On Electrochemical Alloying 65
4.1 Test Setup 67
4.2 Results and Discussion 69
4.2.1 Actuation of Discs 69
4.2.2 Actuation of Controlled-Folding, Rectangular Actuator 72
4.3 Actuation Modeling 75

4.4 Bifurcation 84
4.5 Summary 87
4.6 References 87
5 Actuation Devices Based on Electrochemical Alloying 86
5.1 Materials Selection 87
5.1.1 Lithium-Aluminum System 89
5.1.2 Lithium-Tin System 91
5.2 Results and Discussion 92
5.2.1 Self-powered Actuation – Aluminum Versus Tin 92
5.2.2 Galvanostatically Discharged Aluminum Actuators 98
5.2.3 Self-powered Aluminum Electrochemistry, Morphology, and Microstructure 105
5.2.4 Actuation Energy Density 118
5.3 Summary 121
5.4 References 121
6 Controlled Folding Aluminum-based Actuator Design and Performance 123
6.1 Materials and Methods 123
6.2 Controlled Folding Circular Actuators 124
6.2.1 Actuation Results 125
6.2.2 Microstructure 127
6.3 Controlled Folding Rectangular Actuators 128
6.3.1 Self-Powered Actuation Results 128
6.3.2 Displacement Rate Control via Galvanostatic Discharge 131
6.4 Summary 136
7 Displacement Rate Control of Self-Powered Actuators 138
7.1 External Resistance 138
7.2 Duty Cycle 140
7.3 Substrate Thickness Effects 143
7.4 Summary 148
8 Future Directions 149
8.1 Intercalation Oxides and Graphite 149
8.2 Metal Alloying 149
8.3 References 151

List of Figures

Figure 1-1. Schematic of a typical lithium-ion battery. Lithium ions (red circles) are stored, generally via intercalation or alloying, in the electrodes. During charging or discharging processes, these ions and electrons move from one electrode to the other, creating phase changes and associated volume changes. 21
Figure 1-2. Illustrative example of an active material under different boundary conditions: a) prior to activation; b) activated under zero load; c) activated while clamped at both ends; and d) activated under stiffness-matched load. 24
Figure 1-3. Characteristic curves for a general active element (or actuator) for different activation states and loads. 26
Figure 2-1. Volume change and potential for commercial lithium ion batteries during galvanostatic cycling at C/5. The batteries expand during charging and contract during discharging, reversibly around 1.5%. 36
Figure 2-2. Viscoelastic behavior of commercial batteries. (a) Stress relaxation of battery type A upon repeated loadings to 10 MPa in 10 minute intervals while holding the displacement constant during the interval. (b) Creep strain of battery type C2 while loaded at 20 MPa. 38
Figure 2-3. Thickness changes during C/3 galvanostatic cycling for a battery of type A under stresses of (a) 5 MPa, (b) 10 MPa, (c) 15 MPa, and (d) 20 MPa. Maximum displacements are evident at lower stresses, with complete charging and discharging also available. Capacity fade and corresponding reduced strain is evident at higher stresses. Also evident is a background creep strain. The initial thicknesses of the batteries were ~5.2 mm. 40
Figure 2-4. Actuation strain and work output at different applied stress levels for commercial lithium ion batteries. Actuation strain decreases with increasing stress. Work output is maximized at an intermediate stress level where strain is still significant. 42
Figure 2-5. Actuation curves during 4.5 V potentiostatic charging up to 250 mAh for a battery of type C2 under 2 and 5 MPa. Over 1% strain is achievable on the order of one minute. 44
Figure 3-1. (a) Three-quarter view schematic of the highly-oriented pyrolytic graphite (HOPG) cell. The blue posts represent the HOPG posts while the surrounding red section is the lithium counterelectrode. (b) Profile view of the HOPG cell. The HOPG posts protrude over the counterelectrode and are the only load-bearing active element. (c) SEM micrograph of the laser-machined HOPG posts. The [0001] direction is parallel to the post axis. (d) Macro shot of the HOPG cell. 48
Figure 3-2. Electrochemically induced expansion and contraction of HOPG microactuator under various stress levels, shown against the corresponding cell voltage (li metal counterelectrode). (a) HOPG bonded to aluminum oxide substrate with Cu foil prior to laser micromachining. Against a 10 MPa constant stress, a constant voltage discharge at 0.01 V (~-0.1 V overpotential) results in 6.7% graphite expansion at a composition of $Li_{0.546}C_6$, producing mechanical

work of 670 kJ m^{-3} (310 J kg^{-1}). The voltage relaxes to 0.1 V during an open-circuit hold, showing that the graphite is not Li saturated. The strain is completely reversed upon charging at a constant voltage of 0.5 V (~0.4 V overpotential). (b) Against 100 MPa stress, constant current test conditions resulted in lower, kinetically limited intercalation reaching 1.3% reversible strain and a mechanical work of 1300 kJ m^{-3} (602 J kg^{-1}). 52
Figure 3-3. Summary of strain and work output of HOPG microactuators under various stress levels. At 50 MPa and below, actuators were tested under constant-voltage conditions. At 100 MPa and above, actuators were tested under constant-current conditions. 53
Figure 3-4. Schematic and photographs of a high-density electrode cell. (a) Schematic of a bilayer cell. The graphite anode has a preferential orientation even in powder-based form. (b) The individual electrodes of $LiCoO_2$ and graphite, measuring 30 x 50 mm. (c) Metal can holding a 22 layer stack of the high density electrodes with dimensions 6 x 30 x 50 mm. 54
Figure 3-5. Under 1 MPa prestress, a 22 layer cell cycled under constant current-constant voltage conditions results in 4.1% actuation strain in 5.5 hours, significantly greater than commercial batteries. 57
Figure 3-6. Strain and voltage profiles for a bilayer cell under (a) 10 MPa and (b) 17 MPa prestress, both cycled under constant current conditions between 3.0 – 4.2 V. Under 10 MPa, 2.3% actuation strain is achieved. This decreases to 1.85% under 17 MPa due to decreased cell capacity. 57
Figure 3-7. Strain and voltage profiles for a LFP/LTO cell undergoing constant-voltage cycling under 1 MPa prestress. This chemistry contracts upon charging and expands upon discharging, achieving a reversible strain of 2.3%. 60
Figure 3-8. Displacement and voltage profile for a LFP/graphite cell under 1 MPa prestress undergoing constant-voltage cycling. The actuation strain of 1.2% is achieved in 60 seconds 61
Figure 3-9. Comparison of specific actuation stress versus actuation strain for actuation technologies.[5] Diagonal lines are lines of constant specific actuation energy. Electrochemical actuators have the largest specific actuation energy of any electrically operated mechanism. 63
Figure 4-1. (a) Schematic of a lithium-aluminum actuator. Upon discharge, lithium ions are stripped from the lithium electrode and form an alloy on the surface of the aluminum electrode, creating a unimorph structure. The increased molar volume induces bending shown on the right. The separator is omitted for clarity. (b) A sample before discharge (left) and after discharge (right) illustrating the deformation. 66
Figure 4-2. Cross sections of aluminum-based actuation elements illustrating (a) "bottlecapping" and (b) "folding" deformation modes 66
Figure 4-3. Schematic of the open cell test setup. 67
Figure 4-4. Disc actuator (left) and controlled folding rectangular actuator (right). The edges of the rectangular actuator are masked so the reaction is limited to the center strip which is ¼ in wide and 22 mm long while the masked regions provide displacement amplification. 68

Figure 4-5. Comparison in displacement between an open cell and packaged cell. The open cell shows 40% more displacement than the packaged cell at capacities greater than 40 mAh. Upon charge, only 0.1 mm of displacement is recovered upon charging indicating a majority of the displacement is a result of plastic deformation. 70
Figure 4-6. Cross section of an aluminum disc-shaped actuator after discharging to 100 mAh and recharging 90 mAh (final discharge capacity of 10 mAh) showing the principal curvature axis of larger curvature. Significant permanent damage is seen on the top surface where the lithium intermetallic had formed. The scale bar is 1 mm. 71
Figure 4-7. Comparion of an open cell sample (squares) to packaged samples (lines, at different external mechanical loads) of a controlled folding, rectangular actuator. Two separate samples (solid and dashed lines) are shown at each load. Similar displacements are seen for both types of samples. 73
Figure 4-8. Cross section of a controlled folding, rectangular aluminum actuator. This sample folded nearly 180 degrees in 250 mAh of discharge. The scale bar is 1 mm. 74
Figure 4-9. Schematic of a cross section of an actuator undergoing bending. The vertical displacement, film thickness, substrate thickness, and radius of curvature are labeled. 75
Figure 4-10. Schematic of an actuator cross-section fit to a circular profile with radius R, arc length s, and lever arms l contributing to displacements y_1 (for a disc actuator alone) and y_2 (for a controlled folding actuator). 77
Figure 4-11. Open cell data and calculated displacements for a disc actuator. Models are based on effective elastic or plastic moduli and the assumptions of constant total thickness or constant substrate thickness. The model using effective plastic moduli and assuming constant total thickness gives the best fit for the data. 83
Figure 4-12. Open cell data and calculated displacements for a controlled folding, rectangular actuator. Models are based on effective elastic or plastic moduli and the assumptions of constant total thickness or constant substrate thickness. The model using effective plastic moduli and assuming constant total thickness gives the best fit for the data. 84
Figure 4-13. Displacement versus capacity actuation curves for packaged disc samples at discrete mechanical loads. The bifurcation point is indicated. 86
Figure 4-14. Representative deformation of an actuator suppressed from folding (left) and an actuator that has folded (right). 86
Figure 4-15. Cross section of an aluminum-based actuator suppressed from folding. The bifurcation manifests itself through a curvature discontinuity point near the center of the sample. The scale bar is 1 mm. 86
Figure 5-1. Packaged aluminum-based actuators in different deformation states. From left to right, an as assembled actuator, an actuator discharged into the non-linear deformation regime, and a bifurcated actuator. 88
Figure 5-2. Plot of molar volume per host metal relative to the molar volume of the pure host metal versus lithium content. Many metals show an increased molar volume with added lithium. Aluminum has a high partial molar volume while tin has a low partial molar volume with respect to lithium. 89

Figure 5-3. Phase diagram for the lithium - aluminum system.[8] Only three equilibrium intermetallics form between Li and Al. 92
Figure 5-4. The NaTl crystal structure of LiAl. The structure consists of two interpenetrating diamond lattices.[9] 92
Figure 5-5. Phase diagram for the lithium - tin system.[11] Seven Li – Sn intermetallics can form equilibrium phases. 93
Figure 5-6. Displacement and current curves for aluminum- and tin-based actuators undergoing discharge through a fixed 10 ohm resistor 95
Figure 5-7. Nyquist plots taken between 0.01 Hz and 1 MHz for (a) aluminum- and (b) tin-based actuators at various states of discharge. The charge transfer resistance for the aluminum electrode decreases as LiAl is formed initially. For the tin electrode, the impedance grows quickly with increasing discharge capacity. 97
Figure 5-8. Displacement versus capacity curves for aluminum- and tin-based actuators. Tin shows an initially greater displacement per capacity which is later suppressed by the force of the LVDT. The arrows indicate the incubation capacity – the minimum capacity needed before measurable deformation. 97
Figure 5-9. Calculated displacement versus capacity models for tin- and aluminum-based actuators from the constant total thickness, plastic model presented in Chapter 4, using the same mismatch strain for both systems. Tin displays a greater displacement per capacity due to greater ratio of yield strength of the film versus substrate. 99
Figure 5-10. Displacement versus capacity curves for aluminum-based actuators discharged galvanostatically between 0.5 and 10 mA. Greater displacements are observed at 4 mA and greater. 101
Figure 5-11. Cross sections of galvonstatically discharged samples at 0.5, 2, 4, and 8 mA after removal from the packaging. All samples were discharged to 100 mAh. The scale bar for each picture is 1 mm. Increased curvature is seen at higher currents. 102
Figure 5-12. Nyquist plots for aluminum-based actuators discharged galvanostatically to 100 mAh. Dashed lines indicate a separate sample. The charge transfer resistance is seen to decrease at higher currents 104
Figure 5-13. Image illustrating the columnar morphology of the LiAl intermetallic film. Feature heights and widths are defined by their orientation to the LiAl/Al interface. This was for an actuator galvanostatically discharged at 10 mA to 100 mAh. 105
Figure 5-14. (Previous page) Optical micrographs from separate samples of the microstructure of intermetallic films from aluminum-based actuators for samples discharged at 2, 4, 6, and 8 mA to 100 mAh. 107
Figure 5-15. Feature heights and widths for samples discharged galvanostatically to 100 mAh. Feature heights decrease with increasing current while feature widths do not significantly vary. 107
Figure 5-16. Displacement and current curves versus capacity for aluminum-based actuators discharged through a fixed 10 ohm resistor for 2, 4, 6, 8, or 10 hours. The displacements are reasonably reproducible in the overlapping time periods while the current is between 11 – 13 mA for a majority of the discharge. 109
Figure 5-17. Nyquist impedance plots for aluminum-based actuators discharged through a fixed 10 ohm resistor for 2, 4, 6, 8, and 10 hours. The discharge capacities for these

samples are greater than for those shown in Figure 5-7 and show increasing impedance with increasing discharge. 110
Figure 5-18. Schematic of a three electrode cell showing placement of a lithium metal 'flag' reference electrode in between the aluminum working electrode and lithium metal reference electrode. 111
Figure 5-19. The potential of the aluminum working electrode and lithium metal counter electrode versus a lithium metal reference electrode and the overall cell voltage for two separate actuators. The overpotential at the aluminum electrode is indicated by the green arrows. 111
Figure 5-20. Cross sections of aluminum-based actuators discharged through a fixed 10 ohm resistor for the indicated time illustrating the evolution of the intermetallic film thickness and overall curvature during discharge. Scale bars are 1 mm. Unreacted areas are circled 113
Figure 5-21. Film thickness versus capacity for aluminum-based actuators discharged through a fixed 10 ohm resistor for a given time. Also plotted are the expected thicknesses of the three Li-Al intermetallics. The data are linear and follow the LiAl line indicating that as the reaction product. 114
Figure 5-22. XRD spectra for aluminum-based actuators discharged through a fixed 10 ohm resistor. The only phases detected are LiAl and Al. LiAl reference intensities with corresponding planes are also given. 115
Figure 5-23. Two-dimensional x-ray spectra centered at 20 degrees 2-theta for a sample discharged to 115 mAh (10 h discharge through a 10 ohm resistor). The bright ring is from the (111) plane and the even intensities throughout indicate there is no texturing. 116
Figure 5-24. (Previous page) Optical micrographs of the intermetallic film formed for separate samples discharged through a fixed 10 ohm resistor for 2, 4, 6, and 8 hours. The scale bars are 100 μm. 119
Figure 5-25. Feature heights and widths for aluminum-based actuators discharged through a fixed 10 ohm resistor for a given time. Feature heights decrease with inreasing discharge while feature widths do not significantly vary. 119
Figure 5-26. Displacement at 200 mAh and work-per-cycle for aluminum-based actuators discharged through a fixed 10 ohm resistor at discrete external mechanical loads. Large displacements are achieved at low loads due to bifurcation/folding whereas smaller displacements are realized at higher loads as the samples take a 'bottlecapped' shape. 121
Figure 5-27. Cross-section of an aluminum-based actuator discharged through a fixed 10 ohm resistor for 24 hours under 6 N load. The center of the sample is convex compared to the typical concave downward. 122
Figure 6-1. Controlled folding samples in (a) a circular geometry and (b) a rectangular geometry. The center strip is the reaction area of exposed aluminum while the rest of the surface has been masked. 126
Figure 6-2. (a) Displacement and current versus time and (b) displacement versus capacity density compared between unmasked ('full') disc and controlled folding disc actuators. The full disc actuators demonstrate higher rates on both scales. 127
Figure 6-3. Calculated displacements for a full disc and controlled folding actuator. 128

Figure 6-4. Cross sections of the actuation element in a controlled folding circular actuator (a) perpendicular and (b) parallel to the folding axis after actuation and removal from the packaging. 129
Figure 6-5. Displacement versus capacity curves for samples pre-bent prior to discharge compared to non-pre-bent samples all under a 200 g load. Pre-bent samples exhibit greater displacements. 132
Figure 6-6. Displacement curves for 1.5 mm thick, controlled folding, rectangular actuators at various fixed loads. These exhibit greater displacement and less load sensitivity than 1.0 mm thick samples. 133
Figure 6-7. Displacement and potential versus capacity for galvanostatically discharged rectangular controlled folding actuators. At high currents, an inflection in the displacement curves correspond with irregularities in the potential curves, as indicated by the vertical arrows, giving a bimodal displacement rate. 135
Figure 6-8. Displacement rate versus galvanostatic current for 1.5 mm and 2.0 mm thick rectangular controlled folding samples. The standard deviation of the displacement rate increases significantly at high currents due to the bimodal slopes in the displacement curves (Figure 6-7) 137
Figure 6-9. Calculated displacements versus capacity for controlled folding rectangles 1.5 and 2.0 mm thick. The displacement for a 1.5 mm thick actuator is 1.78 – 1.94 times greater than for a 2.0 mm thick actuator. 138
Figure 7-1. (a) Displacement curves for self-powered, aluminum-based disc actuators with different fixed external resistances. (b) Average displacement rates for curves in (a). Increasing the external resistance decreases the displacement rate, but the resolution is low. 141
Figure 7-2. Current response for self-powered aluminum-based disc actuators undergoing self-powered discharge at various fixed resistances. At high resistances, the current profiles are flat because the external resistance dominates over the internal impedance. 142
Figure 7-3. (a) Displacement and current response for a tin-based actuator under self-powered discharge through a 10 ohm resistor with varying duty cycles. (b) Average displacement rate during each duty cycle segment. The displacement rate varies linearly with duty cycle percentage. 144
Figure 7-4. Current and voltage response during a 16% duty cycle through a 10 ohm resistor for a tin-based disc actuator. During off times, the current is zero and the voltage increases due to relaxation in the polarization. This increases the current compared to continuous discharge when the circuit is switched back on. 145
Figure 7-5. Displacement curves for aluminum-based disc actuators of different thickensses. Thinner samples show increased displacement and less incubation. . 148
Figure 7-6. Average displacement rate after incubation for aluminum-based disc actuators of different thicknesses. 148
Figure 7-7. Bending moment versus inertia at the observed incubation capacity for aluminum-based disc actuators of different thicknesses. The linear trend verifies the increased bending moment needed to overcome the bending stiffness of the samples. 149

List of Tables

Table 1-1. Selected lithium storage electrodes and their volume and linear strain associated with specified composition changes as determined by experiment..... 18
Table 2-1. Specifications of prismatic lithium-ion batteries tested. 34
Table 4-1. List of variables used in the models for the two different geometries of actuators. 81
Table 4-2. List of material properties used in the displacement models. 81
Table 5-1. Potential and change in volume with respect to pure aluminum for the lithium-aluminum intermetallic compounds..... 91
Table 5-2. Potential and volume change with respect to pure tin for the lithium-tin intermetallics..... 93

1 Introduction / Motivation

Solid intercalation compounds constitute a broad class of materials having the capability for ion insertion (intercalation) and removal, often reversibly and at room temperature. Within this class there are many that undergo significant dimensional change upon the insertion and removal of the ions and which could, in principle, be used as an actuator to deliver mechanical work on demand. It is useful here to distinguish between purely chemical versus electrochemical intercalation – the former refers to ion insertion (typically from a liquid solution) driven by chemical potential difference alone, while the latter refers to electrically driven insertion of ions, resulting in crystallographic changes in a host crystal or sometimes alloying of amorphous materials or the formation of new phases by displacement reactions. I am concerned with exploring the potential of electrochemical actuation materials and devices and understanding their advantages and limitations compared to other technologies.

Actuators provide force and motion control in a variety of applications from micropositioning and medical stents to presses and lifting equipment, requiring a broad range of performance. Metrics include actuation stroke (strain), actuation force (stress), operating frequency (bandwidth), strain resolution, and energy conversion efficiency. Many types of actuation technologies exist that can provide different performance envelopes.[1] Existing actuation technologies excel in certain metrics while being limited in others. For example, piezoelectrics and magnetostrictors offer high frequency (up to 10^7 Hz) and precise strain resolution (10^{-6} – 10^{-9}), but at overall small strains, often on the order of 10^{-3}. Shape memory metals are amongst the highest energy density active materials and can deliver several percent strain with high actuation stress (10^2 MPa), but

are intrinsically slower, relying on thermal phase transistions, and require careful temperature control. The high specific gravity (6000 kg m^{-3}) of the lead-based oxides and metals constituting most of these inorganic actuation materials is also detrimental to weight-based performance metrics. Polymer and gel actuators, on the other hand, can typically provide larger strains ($10^{-1} - 10^{0}$) and have low specific gravity. Their tradeoffs are generally lower elastic moduli (as low as 1 MPa) limiting actuation energy density and force.

1.1 Materials Selection

Electrochemical actuation requires compounds that are both electronically and ionically conductive (i.e., mixed conductors). Numerous examples derive from the field of lithium battery materials. A variety of materials have been investigated for use in these systems, including metals and alloys, layered dichalcogenides and oxides, spinels, and olivines. Table 1[2] lists a number of compounds known to be lithium storage hosts, organized according to those typically prepared as a lithiated material from which lithium is then extracted, and those into which lithium is typically inserted in an electrochemical reaction. Their associated volume changes are also listed, along with their average potential versus Li/Li^{+}, for their range of lithium stoichiometries. The mechanical properties and the behavior upon lithiation of these material systems vary greatly, giving a wide range of actuation properties achievable through electrochemical means which can be tailored depending on the device design. I will cover two classes of devices here with different performance envelopes.

Table 1-1. Selected lithium storage electrodes and their volume and linear strain associated with specified composition changes as determined by experiment.

Lithium Storage Compound	Limiting Composition	Volume Strain $\Delta V/V_0$	Linear Strain* $\Delta L/L_0$	Potential vs. Li/Li^+
Li-extraction				
$LiCoO_2$	$Li_{0.5}CoO_2$	+1.9 %	+0.6 %	3.9 V
$LiFePO_4$	$FePO_4$	-6.5 %	-2.2 %	3.4 V
$LiMn_2O_4$	Mn_2O_4	-7.3 %	-2.5 %	4.0 V
$LiNiO_2$	$Li_{0.3}NiO_2$	-2.8 %	-0.9 %	3.8 V
Li-insertion				
C (graphite)	1/6 LiC_6	+13.1 %	+4.2 %	0.1 V
$Li_4Ti_5O_{12}$	$Li_7Ti_5O_{12}$	0.0 %	0.0 %	1.5 V
Si	$Li_{4.4}Si$	+311 %	+60 %	0.3 V
β-Sn	$Li_{4.4}Sn$	+260 %	+53 %	0.4 V

* Assuming isotropic expansion/contraction such as with powder-based, randomly-oriented electrodes.

One class involves high specific energy actuators with moderate operating frequency. A high mechanical energy density is needed for actuators that induce structural shape change in a relatively stiff object. Also, lower weight is beneficial if the actuator is used in moving vehicles, especially air vehicles. Although the shape change doesn't need to cycle continuously, the operating frequency of the device would need to be fast enough to allow for an acceptably quick transition between the actuated and non-actuated state. Piezoelectrics typically have high power densities due to large bandwidth, but don't have high energy density for these types of applications.

Electrochemical actuators based on graphite and intercalation dichalcogenides and oxides are promising for this class of actuator because they combine large, reversible crystallographic strains and intrinsically high elastic moduli signifying the potential for high specific energies and force. The energy density of active materials can be estimated by a theoretical work cycle in which the active material is actuated to its maximum free strain, ε_{max}, then compressed back to its original dimensions, giving a stored elastic

energy density ½ $E_e\varepsilon_{max}^2$ (assuming linear-elastic response) where E_e is Young's modulus. Taking graphite as an exemplar, lithiation to the saturated composition LiC_6 results in a free strain of 10% in the [0001] direction, along which E_e = 35 GPa.[3] If it were possible to maintain full lithiation at any stress state the theoretical energy density is 175,000 kJ/m^3 (neglecting nonlinearities and composition-dependent elastic constants), which is more than 10^3 greater than typical lead-zirconium-titanate (PZT) piezoelectric ceramics (~100 kJ m^{-3}). Further accounting for the difference in specific gravity of these two materials (2100 kg m^{-3} vs. 7500 kg m^{-3}), the disparity in specific energy is even greater, i.e., 83,000 J kg^{-1} vs. ~14 J kg^{-1}.

The second class of actuators includes large displacement, moderate stress, single-stroke devices. Various medical devices such as infusion pumps and control valves could take advantage of these properties. Metal alloys fit these requirements as many of them dilate in excess of 100% when alloyed with lithium. Aluminum, in particular, is known to have a volumetric expansion of 195% when converted to LiAl. The dilation in metal alloys can be utilized directly or it can be amplified using a unimorph construction. Aluminum also has a Young's modulus of E_e = 70 GPa which yields a theoretical stored elastic energy of 2,188 MJ m^{-3}, assuming isotropic expansion, and specific energy of 810,000 J kg^{-1}. In the lithium battery field, these large dilations have been viewed as an undesirable source of degradation. Thin film tin batteries, for example, show significant hysteresis between lithiation and delithiation meaning actuators based on metal alloys are best suited for single-use applications.

1.2 Electrochemical Cells

Lithium ion batteries are comprised of two electrodes separated by an insulating layer wetted with electrolyte. During charging and discharging, electrons are dissociated at one electrode and flow through an external circuit while lithium ions flow through the separator to the other electrode (Figure 1-1). The electrodes store the lithium generally by intercalation or alloying which results in a phase change and is usually accompanied with a volume change. For example, a typical lithium ion battery system is lithium cobalt oxide (LCO) and graphite. During charging, the half-reactions at each electrode are:

$$LiCoO_2 \rightarrow Li_{0.5}CoO_2 + \tfrac{1}{2}Li^+ + \tfrac{1}{2}e^- \tag{1.1}$$

and

$$6C + Li^+ + e^- \rightarrow LiC_6 \tag{1.2}$$

LCO is an intriguing material as it has a negative partial molar volume of lithium meaning it actually expands as it loses lithium. In going from a fully lithiated state ($LiCoO_2$) to the limit $Li_{0.5}CoO_2$ (only half of the lithium is extracted for safety purposes), there is a net volume change, ΔV, of +1.9%. Graphite also expands during the charging process by 13.1%, primarily in the c-axis direction [0001]. As battery electrodes are typically comprised of randomly-oriented powders, isotropic expansion can be assumed, giving the LCO and graphite linear expansions of 0.6% and 4.7%, respectively. These are greater than typical strains for piezoelectrics, magnetostrictors, and electrostrictors.

The electric potential, E, of each half reaction is determined by the Nernst equation:

$$E = E^0 + \frac{RT}{zF} \ln \frac{a_O}{a_R} \tag{1.3}$$

where E^0 is the standard potential of the reaction, R is the universal gas constant, T is the temperature, z is the number of electrons involved in the reaction, F is the Faraday constant, a_O is the activity of oxidation species, and a_R is the activity of the reduction species. The standard potential is measured under conditions when all species are in their standard states. The average potential for reaction (1.1) is 3.9 V[4] and for reaction (1.2) is 0.1 V.[5] The total standard cell voltage, E^0_{cell}, is the difference between the potential of the cathode and anode, in this case giving an average voltage of 3.8 V.

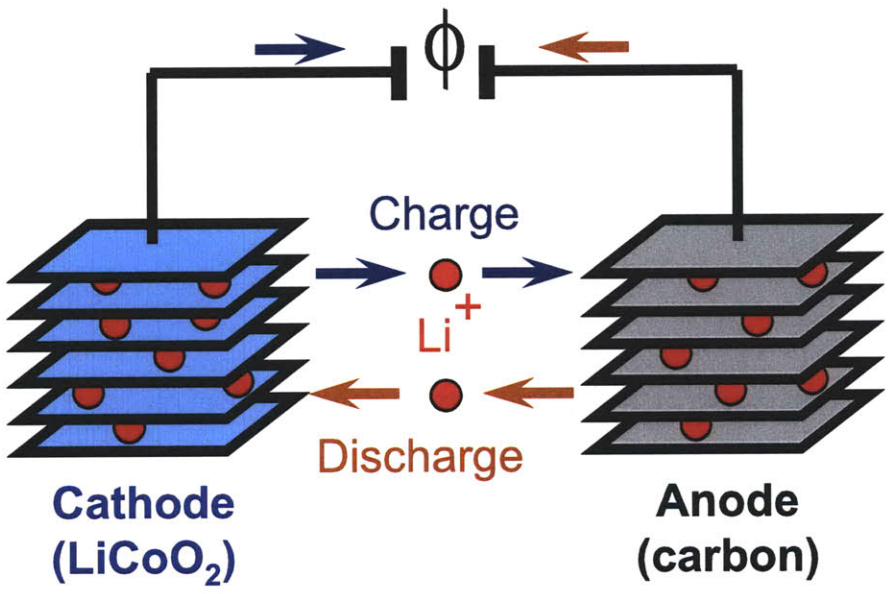


Figure 1-1. Schematic of a typical lithium-ion battery. Lithium ions (red circles) are stored, generally via intercalation or alloying, in the electrodes. During charging or discharging processes, these ions and electrons move from one electrode to the other, creating phase changes and associated volume changes.

The degree of volume change in any given system though will be determined by the amount of lithium that has passed from one electrode to the other, although this may

not necessarily be linear in all materials. Graphite, for example, forms multiple staging compounds with lithium[5] and has a higher partial molar volume at lower lithium stoichiometries. In battery terminology, the amount of charge passed is known as the capacity, Q (mAh), where

$$Q = \int_0^{t_0} I dt \tag{1.4}$$

and I is the current (mA) and t is the time (h). For normalization purposes, this may also be referred to as an areal capacity density, q (mAh cm^{-2}), where

$$q = \frac{Q}{A} \tag{1.5}$$

and A is the surface area of the electrode (cm^2).

The theoretical total capacity, Q_T, of an electrode can be calculated from the stoichiometry limits of the material:

$$Q_T = nF \tag{1.6}$$

where n is the number of moles of lithium between the stoichiometry limits and F is the Faraday constant (96,485 C mol^{-1}), with a conversion factor of 1 mAh = 3.6 C. Using this reference an electrode can be characterized by its state of charge (SOC) or discharge (SOD) as a percentage of the total capacity. For example, if a graphite electrode was intercalated at LiC_{18} ($Li_{1/3}C_6$), this would be a 33% SOC or equivalently a 67% SOD.

Finally, the rate of charge or discharge of a battery is measured in terms of a 'C-rate'. This number is the reciprocal of the number of hours it would theoretically take to completely charge or discharge the cell based on Q_T. For example, if a cell had a Q_T of 10

mAh and was charged at 1 mA, it would theoretically take 10 hours to completely charge the cell so the 1 mA rate is C/10. Conversely, if the 10 mAh cell was charged at 60 mA, a complete charge would theoretically take $1/6^{th}$ of an hour, so the 60 mA rate is 6C. These theoretical values do not account for polarization losses likely to occur.

1.3 Actuators

Here we review the modeling of a general active material, where the actuating force is generated by constraining the linear elastic material. This is the same model proposed by F. Tubilla Kuri.[6]

> Consider a block of an expansive element of modulus E_e, supported from its bottom surface and free at the top, as shown in Figure 1-2a. Upon activation, the material experiences a free strain ε_f, which produces a displacement q_f on its top surface, as shown in Figure 1-2b. Since no external load was initially applied to the block, no useful work is obtained from this expansion. If we now compress the activated material to its original dimensions, a stress, σ, equal to $E_e\varepsilon_f$ is generated, assuming linear elastic behavior. By the principle of linear superposition, this corresponds exactly to the case shown in Figure 1-2c, where the material was clamped from both surfaces *before* the activation, although in this case the elastic energy stored in the material comes from the activation process rather than from the external compressing agent. The compressive load developed is called the blocked load Q_b, and it constitutes the limit load that the active material is capable of actuating against. For any load between zero and Q_b,

different amounts of useful energy will be obtained from the active material. In the case where a spring load with the same stiffness as the material is applied (Figure 1-2d), the amount of energy transferred to the load reaches its maximum and the displacement equals one-half of the free displacement q_f.

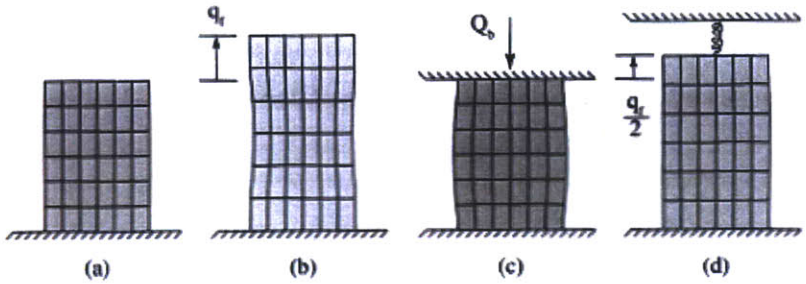


Figure 1-2. Illustrative example of an active material under different boundary conditions: a) prior to activation; b) activated under zero load; c) activated while clamped at both ends; and d) activated under stiffness-matched load.

The above discussion has considered only uniaxially induced normal-stains, but this could of course be extended to other axes and to shear strains. From the above discussion, we see that the uniaxial linear model of the active material can be written as:

$$\varepsilon = \frac{\sigma}{E_e} + M\phi \tag{1.7}$$

where φ denotes the activation state of the material and M is the strain coupling factor.

Figure 1-3 describes graphically the linear actuator model, by means of a load-displacement plot. The solid lines represent the actuator characteristic

curves, which extend outwards for different activation states, and relate the actuator load to the output displacement. The outermost black line constitutes the characteristic curve for the state of full activation, which joins the points (q_f, 0) and (0, Q_b). The grayed area below this line corresponds to the total available mechanical energy, given by

$$W = \frac{1}{2} Q_b q_f \tag{1.8}$$

If we divide by above expression by the volume of the active element V_e, we obtain the energy density of the material, w, which is independent of its geometry and constitutes a useful metric for comparing different active material technologies. We can thus write

$$w = \frac{1}{2} \sigma_b \varepsilon_f = \frac{1}{2} E_e \varepsilon_f^2 \tag{1.9}$$

The specific energy can be calculated by dividing this expression by the density of the active material, giving a weight-based performance metric.

Figure 1-3 also shows a series of dotted lines representing loads of varying stiffness. As mentioned above, we see in the figure that not all of the material mechanical energy will be available at the output. For the case of the impedance-matched load, the maximum possible amount of energy is extracted, corresponding to one-fourth of W and an output displacement of $q_f/2$.

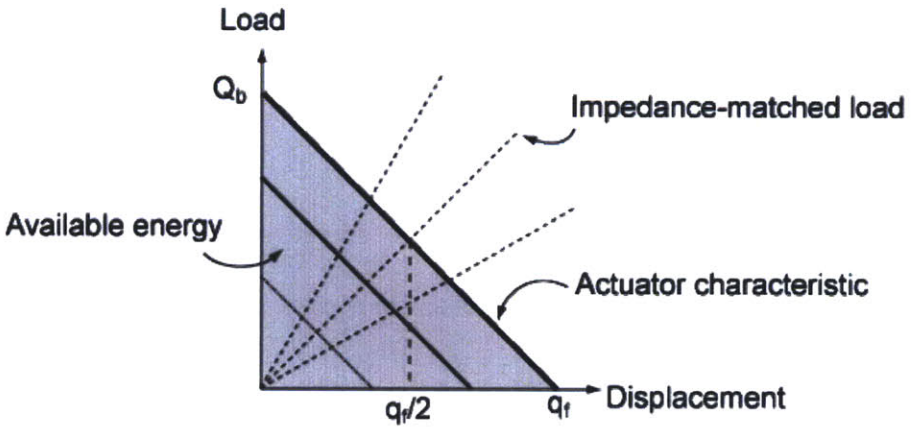


Figure 1-3. Characteristic curves for a general active element (or actuator) for different activation states and loads.

In addition to these metrics explained by Kuri, the frequency *f*, or bandwidth, is the speed required for one complete actuation cycle. The power density can be calculated by the product *wf*. Similarly, this can also be converted to specific power by dividing by the density of the active material. For single-stroke actuators that don't cycle, the overall displacement rate (dy/dt) or single-stroke power output ($\sigma\varepsilon/t$) are critical metrics.

Finally, the efficiency, η, is the ratio of the output energy to the input energy. For electrochemical actuators, the form of input energy is electrical while the output energy is mechanical.

1.4 Thermodynamics

The cell potential, E^0_{cell}, is related to the Gibbs free energy by:

$$\Delta G^0 = -zFE^0_{cell} \tag{1.10}$$

For the LCO/C system, this equates to 36 kJ mol^{-1}. The stored elastic energy of a material undergoing deformation is, assuming linear elastic behavior:

$$\Delta G = \frac{1}{2}\sigma\varepsilon = \frac{1}{2}\frac{\sigma^2}{E_e} \tag{1.11}$$

Comparing (1.10) and (1.11), we see that the driving force for electrochemical intercalation overwhelms the elastic energy of typical inorganic materials at their failure stress. Taking graphite as an example, which has an E_e = 35 GPa in the c-axis direction, a cell voltage of 3.7 V is approximately equal to a 69 GPa applied stress – much higher than typical failure stresses (e.g. 1 GPa, which is equivalent to 7.8 x 10^{-4} V). It is clear that high stresses should have a negligible impact on the thermodynamic voltage of the active materials in the cell. From an actuation perspective, this indicates that the potential of electrochemical actuators of this type does not need to be high for effective actuation, unlike field-driven actuators such as piezoelectrics. Also, the state of strain should be readily maintained in open circuit conditions, even in the presence of high stresses, providing a set-and-forget characteristic.

1.5 Electrochemical Actuation in Literature

Electrochemical actuation has been demonstrated before utilizing several mechanisms. One class of actuators based on pneumatics use electrolysis to generate gas pressure.[7] Others have used surface double-layer charging to generate a dimensional change.[8,9] Actuation based on electrochemical intercalation has been demonstrated using silver-conducting compounds[10], vanadium oxide nanofibers[11], and graphite[12], however most of these studies have only explored the stress regime from 0 to 6 MPa. In contrast, this thesis will include experiments on lithium intercalation up to 200 MPa. In addition, electrochemical actuation based on lithium alloying will be discussed using an intrinsic,

displacement-amplifying design. Further, electrochemically actuated redox polymers have been described.[13-15] The volume expansion of commercial lithium-ion batteries of various chemistries has also been investigated to a small degree.[16-18] Details about the literature work will be cited in the relevant discussions later.

1.6 Thesis Scope and Organization

While the general phase changes, and associated unit cell dimensions, of battery materials are well-characterized, the utilization of this mechanism to produce useful mechanical work is not. The primary goal of this thesis is to characterize the actuation performance of these materials under the metrics outlined above. Due to the nature of electrochemical systems though, the characterization will be done primarily on the device level rather than strictly the material level. There are two different classes of electrochemical actuation technologies though: a lower strain, moderate bandwidth technology enabled by intercalation oxides and graphite and a higher strain, single-use technology enabled by lithium alloying.

Chapter 1 has given a general background on the relevant aspects of electrochemistry and actuation. Chapters 2 and 3 will focus on the lower strain, high specific energy, moderate bandwidth actuators based on intercalation oxides and graphite. These derive directly from commercially available cells which provide a convenient baseline on which to make improvements. Chapter 4 discusses the deformation behavior of an aluminum sample undergoing lithium alloying. Chapters 5, 6, and 7 discuss the actuation characteristics of a device based on lithium alloying. Finally, Chapter 8 will be a discussion on future directions in the field of electrochemical actuators.

1.7 References

1. Huber J, Fleck N, Ashby M. Selection of mechanical actuators based on performance indices. *Proceedings of the Royal Society of London, Series A: Mathematical, Physical and Engineering Sciences*. 1997;453(1965):2185-2205.
2. Koyama Y, Chin TE, Rhyner U, et al. Harnessing the actuation potential of solid-state intercalation compounds. *Advanced Functional Materials*. 2006;16(4):492-498.
3. Woo KC, Kamitakahara WA, DiVincenzo DP, et al. Effect of In-Plane Density on the Structural and Elastic Properties of Graphite Intercalation Compounds. *Phys. Rev. Lett.* 1983;50(3):182.
4. Linden D, Reddy TB eds. *Handbook of Batteries*. 3rd ed. New York: McGraw-Hill; 2002.
5. Ohzuku T, Iwakoshi Y, Sawai K. Formation of lithium-graphite intercalation compounds in nonaqueous electrolytes and their application as a negative electrode for a lithium ion (shuttlecock) cell. *Journal of the Electrochemical Society*. 1993;140(9):2490 - 2497.
6. Tubilla Kuri F. Development of a Morphing Helicopter Blade with Electrochemical Actuators. 2007.
7. Neagu CR, Gardeniers JG, Elwenspoek M, Kelly JJ. Electrochemical microactuator: principle and first results. *Journal of Microelectromechanical Systems*. 1996;5(1):2-9.
8. Spinks G, Wallace G, Fifield L, et al. Pneumatic carbon nanotube actuators. *Advanced Materials*. 2002;14(23):1728-1732.
9. Weissmuller J, Viswanath RN, Kramer D, et al. Charge-induced reversible strain in a metal. *Science*. 2003;300(5617):312 - 315.
10. Takada K, Kondo S. Electrochemical actuator with silver vanadium bronzes. *Solid State Ionics*. 1992;53-56(pt 1):339-342.
11. Gu G, Schmid M, Chiu P, et al. V2O5 nanofibre sheet actuators. *Nature Materials*. 2003;2(5):316-319.
12. Massey CG, McKnight G, Barvosa-Carter W, Liu P. Reversible work by electrochemical intercalation of graphitic materials. In: *Smart Structures and Materials 2005 - Electroactive Polymer Actuators and Devices (EAPAD), Mar 7-10 2005*.Vol 5759. Proceedings of SPIE - The International Society for Optical Engineering. San Diego, CA, United States: International Society for Optical Engineering, Bellingham, WA 98227-0010, United States; 2005:322-330. Available at: http://dx.doi.org/10.1117/12.601491.
13. Anquetil PA, Rinderknecht D, Vandesteeg NA, Madden JD, Hunter IW. Large strain actuation in polypyrrole actuators. In: *Smart Structures and Materials 2004 - Electroactive Polymer Actuators and Devices (EAPAD), Mar 15-18 2004*.Vol 5385. Proceedings of SPIE - The International Society for Optical Engineering. San Diego, CA, United Kingdom: International Society for Optical Engineering, Bellingham, WA 98227-0010, United States; 2004:380-387. Available at: http://dx.doi.org/10.1117/12.540141.
14. Lu W, Fadeev AG, Qi B, et al. Use of Ionic Liquids for pi -Conjugated Polymer Electrochemical Devices. *Science*. 2002;297(5583):983-987.

15. Wang H-, Gao J, Sansinena J-, McCarthy P. Fabrication and Characterization of Polyaniline Monolithic Actuators Based on a Novel Configuration: Integrally Skinned Asymmetric Membrane. *Chem. Mater.* 2002;14(6):2546-2552.
16. Lee JH, Lee HM, Ahn S. Battery dimensional changes occurring during charge/discharge cycles - Thin rectangular lithium ion and polymer cells. In: *Journal of Power Sources*.Vol 119-121. Monterey, CA, United states; 2003:833 - 837. Available at: http://dx.doi.org/10.1016/S0378-7753(03)00281-7.
17. Wang X, Sone Y, Kuwajima S. In Situ Investigation of the Volume Change in Li-ion Cell with Charging and Discharging: Satellite Power Applications. *Journal of the Electrochemical Society*. 2004;151(2):A273 - A280.
18. Wilkinson D, Wainwright D. In-situ study of electrode stack growth in rechargeable cells at constant-pressure. *Journal of Electroanalytical Chemistry*. 1993;355(1-2):193-203.

2 Electrochemical Actuation of Lithium Rechargeable Batteries

Characterizing the actuation performance of commercially available lithium-ion batteries provides a useful baseline and insight on how to optimize their actuation performance. One of the most common chemistries is $LiCoO_2$/graphite, as mentioned in Chapter 1. Upon charging, the total cell reaction is

$$2LiCoO_2 + 6C \rightarrow 2Li_{0.5}CoO_2 + LiC_6 \tag{2.1}$$

The net volume change for a balanced cell is 6.9%, however, most actuators take advantage of linear strain. Assuming isotropic expansion due to randomly oriented powder electrodes, the theoretical linear strain is 2.3%, which is significantly greater than most piezoelectrics. Piezoelectrics offer a useful comparison since they are also electrically operated.

2.1 Electrochemical Actuation via Intercalation in Literature

As mentioned in Chapter 1, there has been some research into the expansion of batteries already. Wilkinson and Wainwright[1] investigated Li/Li_xMnO_2 and C/Li_xMnO_2 electrode stacks up to stresses of 3 MPa which showed no more than 10 μm and 2 μm displacements, respectively, for stacks of original thicknesses of 273 μm and 245 μm. They attribute the larger thickness change for the cell utilizing a metallic Li anode to dendritic growth of Li. Lee et al.[2] looked at the expansion of commercially available cells from LG Chemical Ltd and other manufacturers. They ascribed volume changes to lithium ion de-/intercalation, irreversible volume changes due to reaction deposits, and

dead volume and pressure changes depending on battery construction. Pouch cells expanded from 0.07 – 0.14 mm (2 – 4%) in thickness. Metal can enclosed cells expanded up to 0.2 mm (6%), primarily due to internal gas pressure. Wang et al.[3] also tested commercial LCO/C cells and found a 6% thickness change was achievable. Two other references[4,5] tested multiple commercial LCO/C cells and found only 1.6% thickness change during cycling. Barker[4] showed $LiMn_2O_4$/C cells demonstrate a smaller 0.2% thickness change and this maximum was at a 45% SOC. Finally, commercial thin-film batteries utilizing a Li/LCO chemistry has been characterized.[6] The expansion mechanism here combines the volume change of LCO with reversible Li electroplating. The maximum strain of the battery was 0.27% and could withstand up to 2.0 MPa. These results will be compared to the current research in the relevant sections.

2.2 Battery Construction

2.2.1 Materials

Here is a brief synopsis of the materials that go in to a lithium ion battery. Electrodes are usually fabricated from powders of the active material mixed in with carbon to enhance conductivity and polymer binders to aid adhesion to the current collector. The current collectors are typically metal foil, copper for the negative electrode (graphite) and aluminum for the positive electrode (LCO). The electrodes are isolated from each other by a porous polymer separator. A liquid electrolyte of a lithium salt dissolved in non-aqueous solvents is used for lithium ion transport across the separator. The battery is often sealed inside a metallized polymer laminate or a welded metal can.

2.2.2 Construction

There are different battery constructions which can have significant influence on their actuation behavior. In a stacked configuration, current collectors are coated on both sides with the electrodes and are alternately stacked between layers of separator. These will often take the form of a rectangular prismatic battery. Similar electrodes are connected electrically in parallel to increase capacity. The Bellcore construction refers to special processing and assembly steps using plasticizers, however the configuration remains similar to a stacked battery.[7] Another method of construction is the spiral wound, or 'jelly-roll', configuration. Here, two strips of current collectors are again coated on each side with the electrode and isolated with a separator layer. To make the battery, these are then rolled up forming a spiral cross section. These often end up as cylindrical cells, but can also have a prismatic form-factor as well.

2.3 Methodology

2.3.1 Battery Types

A summary of the batteries used for these experiments can be found in Table 2-1. The discharge C-rate is the maximum recommended by the manufacturer. Batteries from three different manufacturers were used: A, Amperex Technology Limited (ATL; Hong Kong); B, Saehan Enertech (Seoul, Korea); and C, Kokam (Kyunggi-Do, Korea). All of these batteries are pouch-type, sealed in a metallized polymer laminate.

Table 2-1. Specifications of prismatic lithium-ion batteries tested.

Cell ID	Construction	Dimensions (mm)	Capacity (mAh)	Discharge C-rate
A	Bellcore	25.0 x 10.0 x 5.28	150	1C
B1	Wound	27.0 x 10.5 x 3.74	120	1C
B2	Stacked	26.5 x 16.0 x 4.09	200	1C
C1	Stacked	53.0 x 30.0 x 4.20	640	15C
C2	Stacked	53.0 x 31.0 x 5.00	740	20C

2.3.2 Testing Equipment and Setup

Batteries were controlled using a Maccor 4300 battery tester (Maccor, Inc., Tulsa, OK, USA), Solartron SI 1260 with SI 1287, and Solartron SI 1284 (Solartron, Farnborough, UK). Charging protocol varied using constant current (CC, galvanostatic), constant voltage (CV, potentiostatic), and constant current-constant voltage (CC-CV) methods. Mechanical loads were applied using an Instron Microtester 8848, Instron 5569, and Instron 5567 (Instron, Norwood, MA, USA) materials testing machines. Manual measurements were carried out with a CD-6" CS micrometer (Mitutoyo, Japan).

Volume expansion measurements were carried out by submerging the batteries in silicon oil (Avocado Research Chemicals, Heysam, UK) inside a glass vial. A rubber stopper capped the vial with feedthroughs to connect to the battery, a thermocouple, and a glass capillary. As the battery was cycled, volume changes could be measured by the level of the silicon oil in the capillary. The whole setup was contained in an oven set at 30°C to minimize thermal effects.

Linear dimensional changes were measured with the Instron materials testing machines. Batteries were compressed between platens and held at various load levels. This uniaxial stress was always oriented normal to the large prism face (i.e., the thickness direction). Cycling of the battery required the crossheads to move to maintain the original

load. Similarly, blocked force testing could be conducted in a similar fashion by holding the displacement constant and measuring the load response.

2.4 Results and Discussion

2.4.1 Volume Changes Under Zero Stress

The volume changes during cycling were measured for batteries A, B1, and B2 using the silicon oil setup. The batteries were cycled at a C/5 or C/2.5 rate between the limits of 3.0 and 4.2 V. Typical volume expansion and potential curves are shown in Figure 2-1. The volume and potential track very well with expansion occurring upon charging and contraction occurring upon discharging. Battery A expanded 1.55%, battery B1 expanded 1.25%, and battery B2 expanded 1.55%.

These values are significantly less than the theoretical 6.9% volume expansion predicted by (2.1). The 6.9% prediction though accounts only for the active materials. The inactive additives, current collectors, separator, and packaging serve to decrease the relative amount of expansion achievable. Further, any volume trapped during sealing will also reduce the measurable expansion as the active components will fill these spaces without changes to the external dimensions of the battery. Given the capacities, it is possible to calculate the amount of active material in these batteries, which ranged from 27 – 30% by volume. Therefore, the predicted volume expansion of these batteries falls to 1.90 – 2.10%.

As the electrodes are formed from powders and generally not sintered, there is some porosity in the electrode itself. This may also account for trapped volume. Further, the electrodes are adhered to current collectors and will be constrained in two dimensions.

The batteries with Bellcore and stacked constructions showed greater volume change than the wound battery. The wound construction also has current collectors aligned in the thickness direction providing even more constraint on the battery.

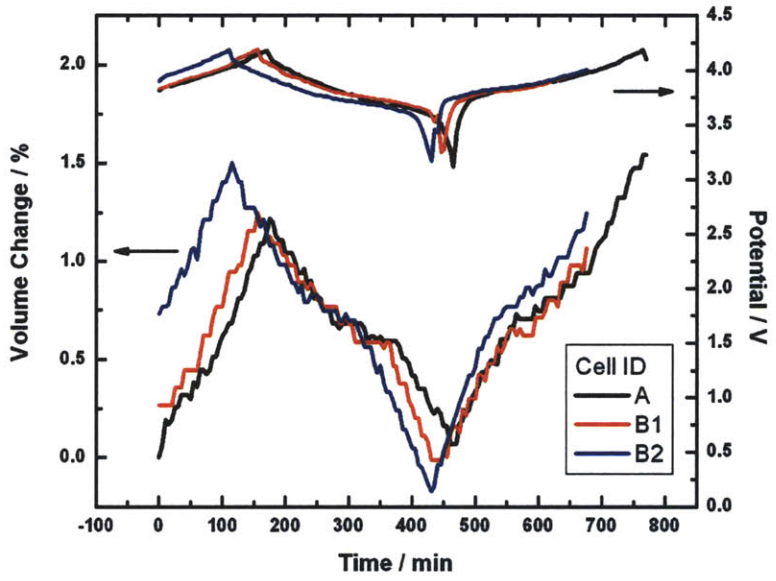


Figure 2-1. Volume change and potential for commercial lithium ion batteries during galvanostatic cycling at C/5. The batteries expand during charging and contract during discharging, reversibly around 1.5%.

2.4.2 Linear Dimension Changes Under Zero Stress

The linear (thickness) change of the batteries under zero applied stress was measured separately under C/2.5 cycling conditions with a micrometer. Battery A displayed 2.0% linear expansion, battery B1 showed 3.0%, while battery B2 demonstrated 2.5% linear expansion. All of these are greater than their respective volume changes, but are comparable to the predicted linear expansion from (2.1). In fact, battery B1 showed the least volume change but the greatest thickness change. These values are slightly greater than some reported in literature (1.6%)[4,5] although much less than one of

the reported values (6%).[3] The reported 6% value seems erroneously large considering the volume of inactive material in the batteries as outlined above. The 1.6% values seem more reasonable. The larger expansions that we measure could be due to measurement error and inhomogeneous expansion of the cell. Some distortion of the battery can also occur, especially for a spiral wound construction.[2]

The total volume dilation should be the sum of the linear strains. That the thickness expansion measured here is larger than the total volume expansion indicates that there may be contraction in the in-plane directions. Some of this can be attributed to the current collector constraints as discussed in the previous section. This may also lead to a Poisson effect where the planar dimensions change, although this wasn't experimentally verified. Expansion in the thickness direction could pull in the walls of the pouch cell, minimizing overall volume expansion. Other factors include bulging, or non-uniform expansion of the thickness so that the middle of the battery is thicker than at the edges.[2] Further, measurement error could also lead to inaccurate values. In any case, it is clear that the battery expands primarily through the thickness.

2.4.3 Passive Mechanical Response of Commercial Batteries

Viscoelastic response was evident in mechanical testing of the commercial batteries. All cells exhibited an initial rapid compression as free volume was removed, followed by stress relaxation under a constant displacement and creep strain under constant stress. In Figure 2-2a, stress relaxation under constant displacement is illustrated, whereby a 10 MPa stress was repeatedly applied to an as-received sample of battery type A, following which the displacement was held constant. It can be seen that the stress

relaxes quickly at constant displacement, although the creep eventually saturates.In Figure 2-2b, the strain vs. loading of as-received battery type C2 is shown. Upon application of a 20 MPa uniaxial stress, there is an initial strain of nearly 25%, following which a period of slower creep strain under constant stress occurs. From these results, it is clearly desirable to prestress the cells in order to remove as much free volume and creep as possible prior to use as electrochemical actuators.

Much of the viscoelastic behavior can be attributed to the 'soft' construction of these batteries. As mentioned in section 2.2, batteries comprise of, in part, powder based electrodes and a polymer separator in a laminate packaging. Viscoelastic response is typical for polymeric materials such as the separator, electrode additives, and layers in the packaging. Further, free volume associated with the powder packing of the electrodes or the sealing process will aid in stress relaxation and creep strain.

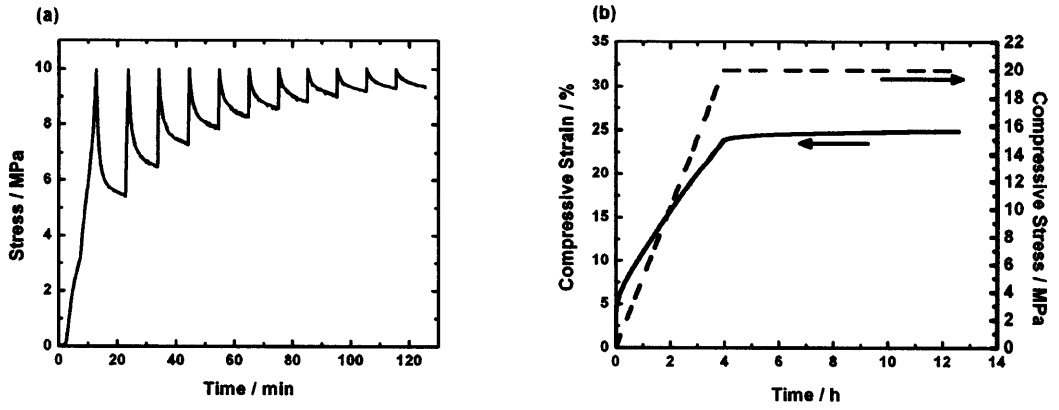


Figure 2-2. Viscoelastic behavior of commercial batteries. (a) Stress relaxation of battery type A upon repeated loadings to 10 MPa in 10 minute intervals while holding the displacement constant during the interval. (b) Creep strain of battery type C2 while loaded at 20 MPa.

2.4.4 Linear Dimension Changes Under Applied Stress

While the free expansion gives an indication of the reversible dimensional changes, no work is extracted since there is no opposing mechanical load. In order to characterize the actuation potential of commercial batteries, stresses up to 20 MPa were applied in the thickness direction of a battery of type A while it was cycled galvanostatically at a C/3 rate between 3.0 – 4.2 V. The resulting displacement and potential profiles are shown in Figure 2-3. A few different effects are evident as the applied stress increases. The strain curves each show background creep, superimposed upon which is a cyclic actuation strain of 1-2% depending on the applied stress. With increasing stress, the actuation strain is reduced, and it is clear that above about 15 MPa, the actuation strain dampens quickly with increased cycling. The simulataneous loss of strain and loss of capacity at higher stresses indicates that increased stress limits the ability of the cells to cycle through kinetic factors, rather than the inability of the active material to actuate under the applied potential. We base this conclusion in part on the thermodynamic analysis presented in section 1.4, but also on the demonstration[8] that graphite microactuators of a different construction can actuate under much higher stresses. One possible explanation for the decreased rate capability of the cells under stresses greater than 10 MPa is compression of the microporous separator film causing closure of porosity and limiting transport through the separator. Another is that densification of either the positive or negative electrode under pressure, and possibly with creep assisted by the cyclic actuation, results in a decreased rate of ion transport. These results may also be relevant to the use of prismatic lithium ion cells in pack designs where significant stresses are applied. While additional work is necessary to explicitly identify the rate-

limiting components of the current actuators, it is clear that improvements in mechanical design that allow the laminated actuators to bear significant load without creep and loss of rate capability will be desirable in any optimized electrochemical actuator.

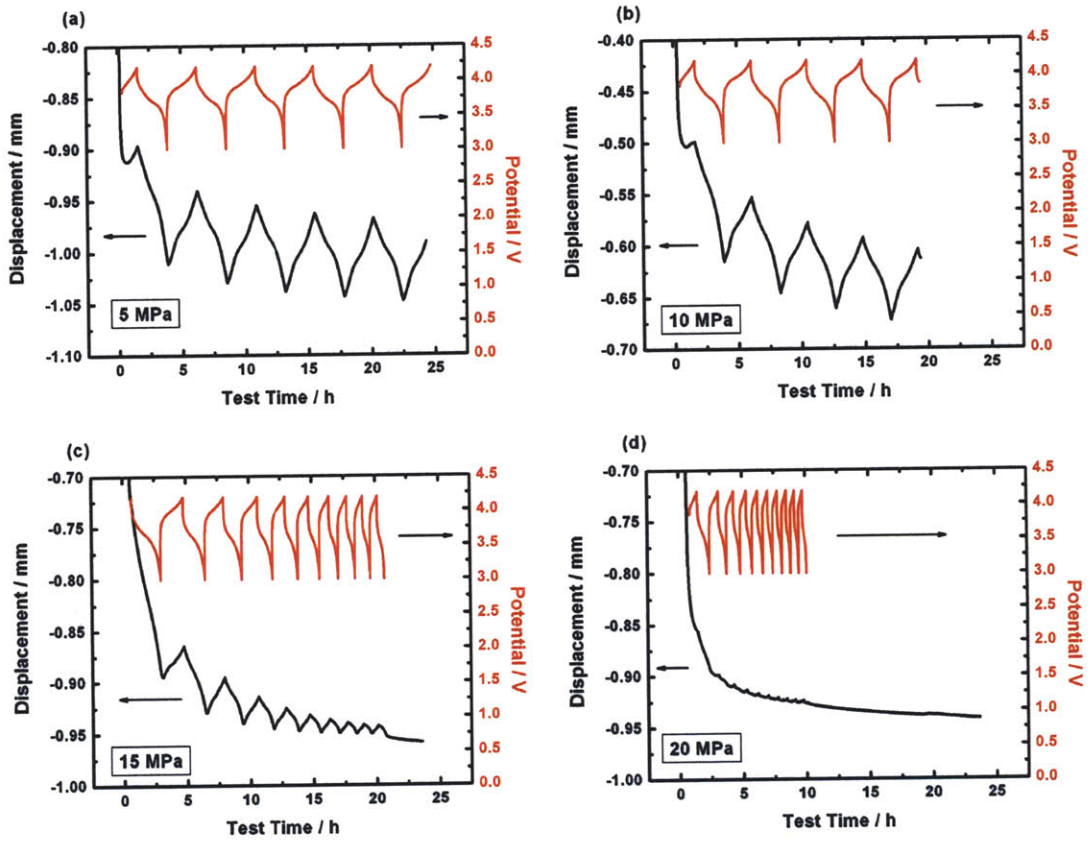


Figure 2-3. Thickness changes during C/3 galvanostatic cycling for a battery of type A under stresses of (a) 5 MPa, (b) 10 MPa, (c) 15 MPa, and (d) 20 MPa. Maximum displacements are evident at lower stresses, with complete charging and discharging also available. Capacity fade and corresponding reduced strain is evident at higher stresses. Also evident is a background creep strain. The initial thicknesses of the batteries were ~5.2 mm.

Despite these limitations, we found that the mechanical work output of these devices was considerable, and exceeded that of high strain piezoelectrics. In Figure 2-4, the actuation strain and mechanical work output of three cells are shown as a function of applied stress. Battery A showed the least fall-off in strain with increasing stress, and

maintained actuation strains exceeding 1.5% for stresses up to 10 MPa. The corresponding mechanical work curve shows a maximum at intermediate stress values where stresses are significant and the actuation strains have not yet fallen off. For battery A this maximum work output is ~150 kJ m^{-3} at a stress of ~10 MPa.

Although the blocked force was not measured directly here, the results in Figure 2-4 suggest that is on the order of 20 MPa, a relatively low value due to the soft construction of these batteries. However, this is greater than the 2 MPa limiting stress for thin-film batteries.[6] Taking a free strain of 3% and a blocked stress of 20 MPa, the actuation strain energy density of the present actuators is ~300 kJ m^{-3}. This is a factor of three greater than the actuation strain energy density of good lead-zirconium-titanate (PZT) piezoelectric ceramics (~100 kJ m^{-3}). Further accounting for the difference in specific gravity of the two device types (2500 vs 7500 kg m^{-3}), the advantage of the electrochemical actuator in specific energy is nearly an order of magnitude, 120 vs ~13 J kg^{-1}.

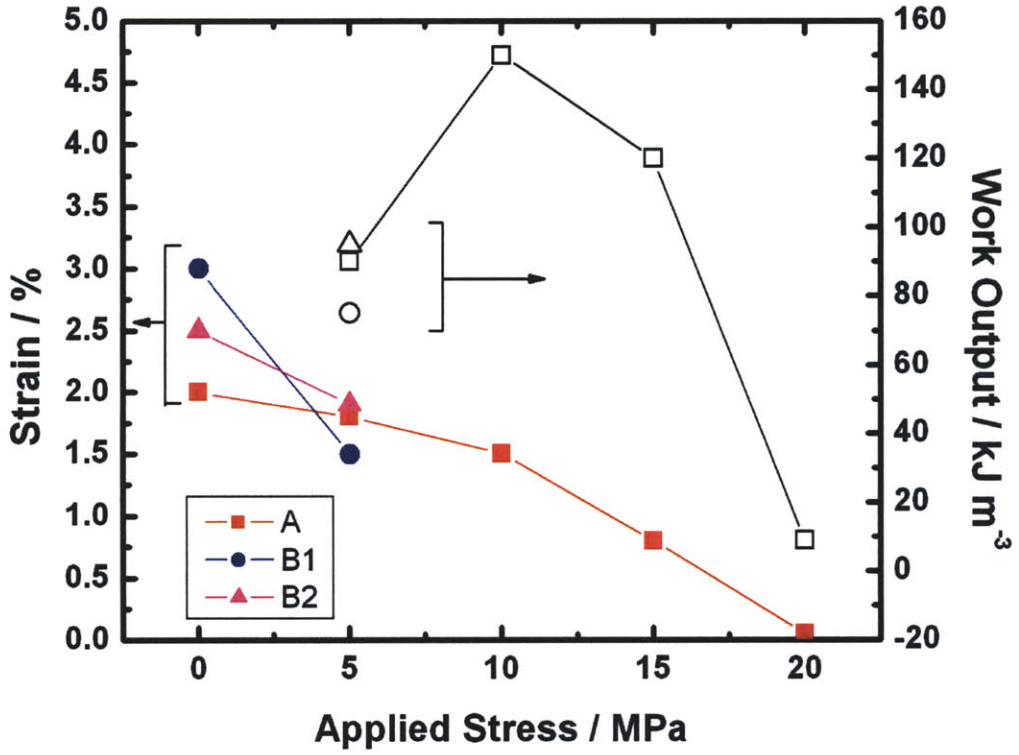


Figure 2-4. Actuation strain and work output at different applied stress levels for commercial lithium ion batteries. Actuation strain decreases with increasing stress. Work output is maximized at an intermediate stress level where strain is still significant.

Piezoelectrics have a clear advantage in actuation bandwidth, however, and can be driven to kilohertz frequencies while maintaining <0.1% strain. We evaluated the actuation speed possible in the cells of type C in Table 2-1, designed for high discharge C-rate, in order to determine the actuation bandwidth of typical, currently available high rate lithium ion cells. First we considered possible charging protocols. In energy storage applications, rechargeable batteries may be cycled in a variety of modes such as constant current-constant voltage (CC-CV) profiles in order to obtain maximum state of charge (SOC), to pulse charge and discharge at intermediate SOC values for maximum power. Here, we aimed to obtain maximum speed of actuation over the SOC regime that

provides the greatest expansion per unit charge capacity. Most tests were conducted using cell type C2, a 740 mAh cell rated for up to 20C discharge. First, we measured the linear strain as a function of the SOC under 2 MPa stress. It was observed that the steepest slope of strain vs SOC occurs over the first 50% of SOC. Thus we conducted rate tests utilizing the initial one-third of SOC, up to a capacity of 250 mAh, corresponding to actuation up to approximately 1% linear strain. Using the low SOC regime was also desirable to prevent overcharging of the $LiCoO_2$ cathode during high rate charging.

CC, CC-CV, and CV charging protocols were tested. The fastest actuation (fastest charging rate) was observed using a CV protocol in which the voltage was instantaneously raised to a predetermined value and allowed to charge with an upper current limit in excess of 20C (14.8 A). The variation in strain and voltage during this protocol is shown in Figure 2-5 for a charging voltage of 4.5 V and applied stresses of 2 and 5 MPa. It is seen that the strain curves are nearly linear and reach strains of slightly over 1% at 250 mAh capacity. The 2 MPa test exhibits slight creep expansion during the high rate test, while the 5 MPa test returns nearly to the original displacement after each expansion/contraction cycle. The actuation speed for a single expansion stroke to 1% strain against 2 to 5 MPa stress is 80 – 100 s; a complete cycle has an actuation frequency of 5 mHz. Tests were also done at 4.2 V (not shown) and yielded similar strains, although the rate was slightly slower. During CV charge there is a momentary (1 – 2 s) increase in current to the 20C limit, after it is limited by the unimpeded current draw of the cell. Increasing the upper current limit during the test beyond 20C did not detectably increase the charge rate or actuation performance of the cell, showing that the internal resistance of the cell is rate-limiting. The strain rates of 0.014 % s^{-1} and 0.010 % s^{-1} at 2 and 5 MPa,

respectively are high compared to what has been achieved with Li electroplating.[6] The reported 0.01 and 0.005 % s^{-1} are referenced to an estimated thickness of the active structure, therefore, the strain rate of the entire battery is actually less. However, it is pointed out that since the actuation is based on kinetic processes, the strain rate should increase exponentially with temperature.

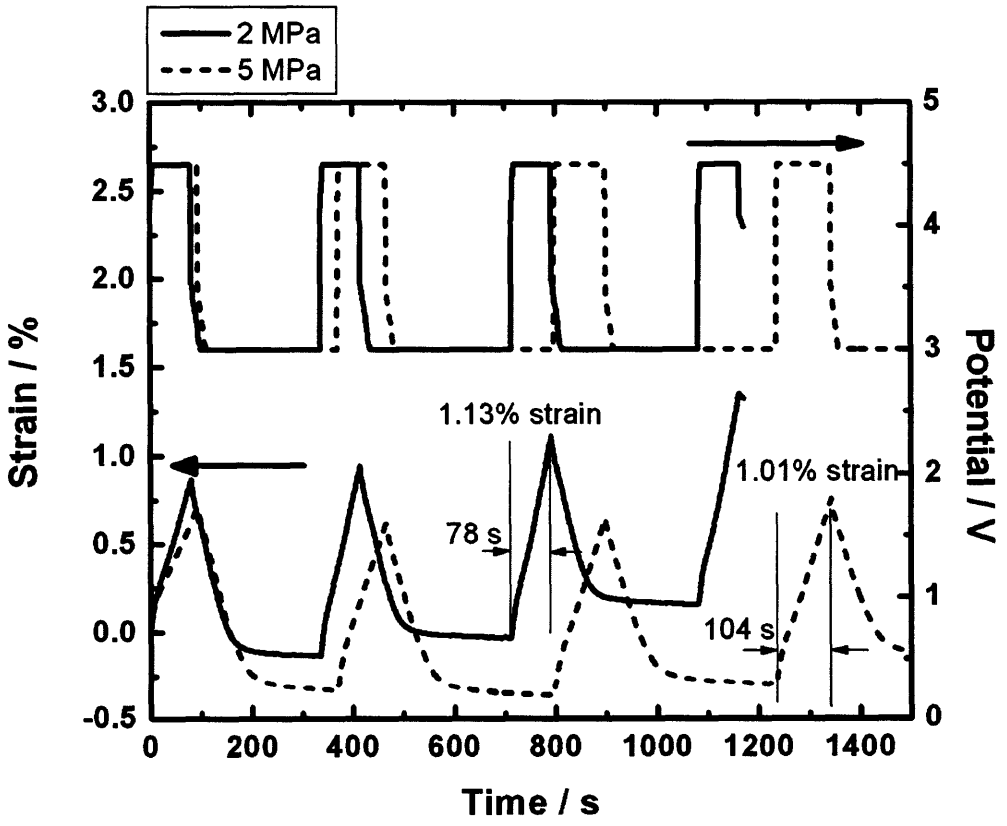


Figure 2-5. Actuation curves during 4.5 V potentiostatic charging up to 250 mAh for a battery of type C2 under 2 and 5 MPa. Over 1% strain is achievable on the order of one minute.

2.5 Summary

These results show that even in a highly unoptimized state, commercially available lithium rechargeable batteries can perform significant mechanical work at rates

that could be useful in applications where larger displacements than piezoelectrics are needed, but slower actuation speeds (of the order of minutes) are acceptable. The main limitations of these types of batteries are their soft construction and limited bandwidth. The following chapter will investigate ways to optimize electrochemical actuators to overcome these limitations.

2.6 References

1. Wilkinson, D. & Wainwright, D. In-situ study of electrode stack growth in rechargeable cells at constant-pressure. *Journal of Electroanalytical Chemistry* **355**, 193-203(1993).
2. Lee, J.H., Lee, H.M. & Ahn, S. Battery dimensional changes occurring during charge/discharge cycles - Thin rectangular lithium ion and polymer cells. *Journal of Power Sources* **119-121**, 833 - 837(2003).
3. Wang, X., Sone, Y. & Kuwajima, S. In Situ Investigation of the Volume Change in Li-ion Cell with Charging and Discharging: Satellite Power Applications. *Journal of the Electrochemical Society* **151**, A273 - A280(2004).
4. Barker, J. In-situ measurement of the thickness changes associated with cycling of prismatic lithium ion batteries based on LiMn2O4 and LiCoO2. *Electrochimica Acta* **45**, 235 - 242(1999).
5. Soga, I. & Kinoshita, Y. In-situ thickness measurement of Li-ion polymer battery. *Japanese Journal of Applied Physics, Part 1: Regular Papers and Short Notes and Review Papers* **41**, 6616 - 6617(2002).
6. Barvosa-Carter, W. et al. Solid-state actuation based on reversible Li electroplating. *Smart Structures and Materials 2005 - Active Materials: Behavior and Mechanics, Mar 7-10 2005* **5761**, 90-97(2005).
7. *Handbook of Batteries*. (McGraw-Hill: New York, 2002).
8. Koyama, Y. et al. Harnessing the actuation potential of solid-state intercalation compounds. *Advanced Functional Materials* **16**, 492-498(2006).

3 Designing Electrochemical Actuators Based on Lithium Rechargeable Batteries

The previous chapter illuminated the performance of commercial lithium rechargeable batteries as electrochemical actuators. Even in an unoptimized state, they deliver performance exceeding that of piezoelectrics in terms of mechanical energy density and specific energy. There are, however, some challenges, namely low bandwidth, soft construction leading to passive mechanical response, and inactive materials limiting the overall actuation strain. In this chapter, we will address these issues by designing electrochemical actuators without regard to energy storage.

3.1 Highly Oriented Pyrolytic Graphite Microactuators

In the commercial lithium rechargeable batteries, the carbon anode is responsible for a majority of the overall volume expansion. The powder-based electrodes are randomly oriented, so the total expansion can be estimated as isotropic. However, in graphite form, intercalation of lithium is known to produce highly anisotropic expansions: 10% in the c-axis and 1% in the a-axis.[1] Further, the inactive materials in series with the anode only serve to reduce the overall actuation strain at the device level. In this section, we investigate ways to utilize this anisotropy and maximize the amount of actuation strain achievable through lithium intercalation by using oriented graphite and minimizing the inactive materials in the actuation direction.

3.1.1 Materials and Methods

Highly-oriented pyrolytic graphite (HOPG; Structure Probe, Inc., West Chester, PA, USA), which has an angular spread of the c-axis crystallites of less than 1°, was used to maximize the utilization of the large c-axis expansion. However, HOPG crystals of macroscopic size do not exhibit significant lithium storage in the standard electrochemical tests due to kinetic limitations. Lithium ion chemical diffusion is highly anistropic in graphite as well and is fastest along the graphite basal plane with a chemical diffusion coefficient of $\sim 10^{-14}$ m^2 s^{-1}.[2] Therefore, it was necessary to laser machine single pieces of HOPG into a load-bearing array of posts with widths of ~200 μm to allow for substantial lithiation within reasonable test times. In one setup, HOPG pieces of 5 mm square by 0.4 mm thick were bonded with copper foil to an aluminum oxide substrate in vacuum at 650°C with pressure. The array of posts was laser-micromachined (Mound Laser and Photonics Center, Inc., Miamisburg, OH, USA) into the HOPG. In a second configuration, the array of posts were laser-micromachined directly into an HOPG coupon (i.e., the substrate was unmachined HOPG). Mechanical loading was applied along the axis of the posts, corresponding to the <0001> direction of graphite. Due to the taper imparted by laser machining, the geometrically averaged cross section was used to compute the applied stress. The machined array was used as the load-bearing electrode with a surrounding lithium metal counterelectrode. The assembly was sealed in an aluminum-polymer laminate packaging with a 1 M $LiPF_6$-based non-aqueous electrolyte. A schematic and photographs of the battery is shown in Figure 3-1.

Strain and electrochemical tests were conducted at room temperature with a custom-designed strain apparatus described elsewhere,[3] in which adjustable spring

preload up to 2000 N could be applied. An Instron 5567 (Instron, Norwood, MA, USA) materials testing machine was also used for select tests. The batteries were electrochemically controlled with a Maccor 4300 battery tester (Maccor, Inc., Tulsa, OK, USA).

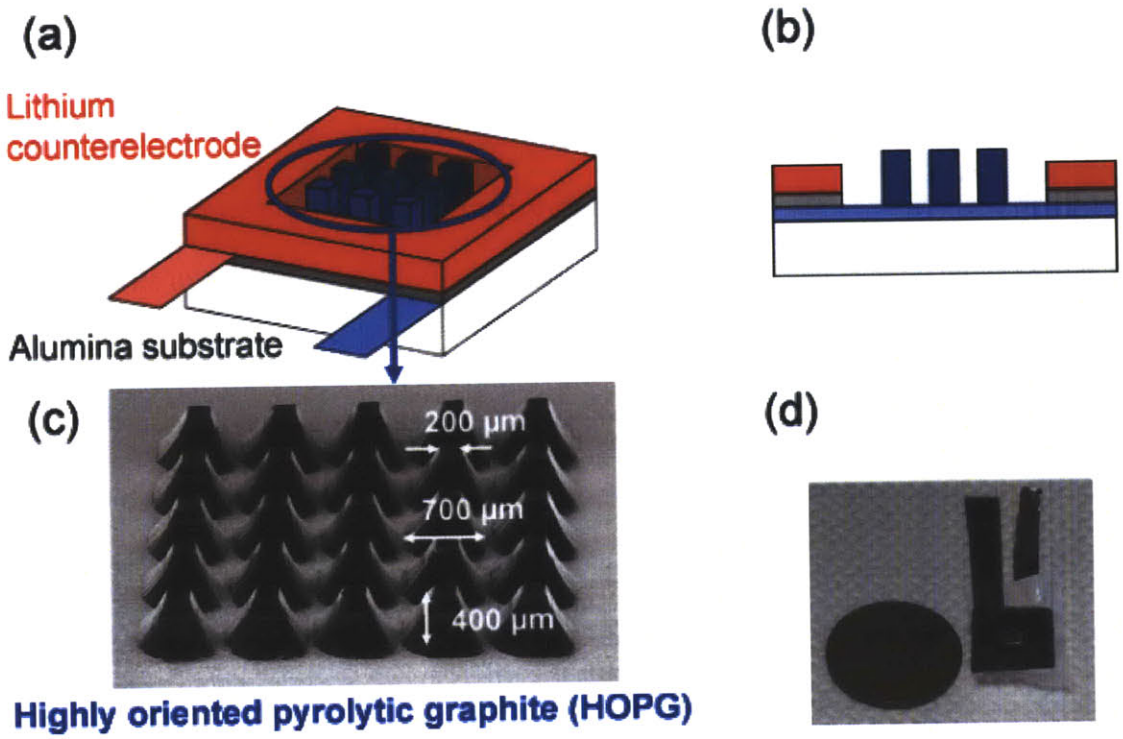


Figure 3-1. (a) Three-quarter view schematic of the highly-oriented pyrolytic graphite (HOPG) cell. The blue posts represent the HOPG posts while the surrounding red section is the lithium counterelectrode. (b) Profile view of the HOPG cell. The HOPG posts protrude over the counterelectrode and are the only load-bearing active element. (c) SEM micrograph of the laser-machined HOPG posts. The [0001] direction is parallel to the post axis. (d) Macro shot of the HOPG cell.

3.1.2 Results and Discussion

Electrochemical actuation of the micromachined HOPG against a constant applied stress is shown in Figure 3-2 for two different discharge/charge protocols. It was found

that a constant-voltage (CV) testing protocol yielded the highest levels of lithiation. Figure 3-2a shows that holding the voltage at a constant value of 0.01 V to effect discharge (graphite lithiation) against a 10 MPa constant stress, an expansion strain of 6.7% was produced which corresponds to a composition $Li_{0.546}C_6$ (54.6% of the theoretical storage capacity). Upon subsequent charging at a constant 0.5 V voltage, the strain is completely reversed. Note that the strain curve is not proportional to time during CV testing since the ion current is allowed to fluctuate in proportion to the electrical driving force (overpotential), which is the difference between the applied voltage and the equilibrium cell voltage. The equilibrium voltage decreases monotonically with increasing x in Li_xC_6[1,4] from an initial value of ~2.5 V and, correspondingly, the magnitudes of the overpotential and the current in Figure 3-2a drop continuously during CV discharge. Note that the 6.7% expansion actually exceeds the theoretical strain for graphite at x=0.546. This is attributed to the non-uniform lithiation of the graphite posts during the dynamic process; presumably the edges of the posts are more highly lithiated and are bearing a greater proportion of the mechanical load than the interior portions. The relaxation of the cell voltage to ~0.1 V during an open-circuit hold following discharge (Figure 3-2a) confirms that the graphite is partially intercalated. Simultaneously, the strain relaxes to ~5.5% as might be expected upon some homogenization of the Li concentration through diffusion. Interestingly, the contraction rate upon charging of the cell is faster than the expansion rate upon discharging, presumably due to the larger overpotential used during charging (~0.4 V) versus that during discharging (-0.09 V). While a lower negative cut-off voltage could be used to obtain greater intercalation upon discharge, plating out of Li metal is thermodynamically possible and complicates the

interpretation of storage capacity and actuation strain. The mechanical work (stress x strain) performed by the graphite (which has a measured density of 2160 kg m^{-3}) during electrochemical expansion is 670 kJ m^{-3} (310 J kg^{-1}).

Under a higher prestress of 30 MPa, the same CV protocol gave 4.3% strain and a lower charge capacity of 35.3% of the theoretical value (Figure 3-3); the mechanical work reached 1290 kJ m^{-3} (597 J kg^{-1}). Under 50 MPa prestress, the strain reached 3.5% and the capacity was 33.6% of the theoretical value, yielding mechanical work of 1750 kJ m^{-3} (810 J kg^{-1}). The strain remains slightly greater than expected from the extent of lithiation while the charge capacity decreases, suggesting slower transport kinetics under stress. Electrical shorting of the sample under higher applied stresses prevented continued testing. In another sample configuration, however, we were able to conduct tests up to 200 MPa. Figure 3-2b shows test results for samples consisting of array of posts micromachined directly onto HOPG coupons, here tested under a CC protocol, which allows a higher rate of testing and linear strain versus time, but yields lower absolute values of ion concentration. The discharge and charge cycles were terminated when the cell voltage reached 0.01 and 2.0 V, respectively. A substantially higher stress of 100 MPa stress was used for the test in Figure 3-2b, under which a reversible strain of 1.3% was obtained, resulting in a work of 1300 kJ m^{-3} (602 J kg^{-1}). The same cell under 200 MPa stress reached a strain of 0.7% and the work obtained was 1400 kJ m^{-3} (648 J kg^{-1}), shown in Figure 3-3. Figure 3-2b shows a hesitation in expansion at the midpoint that is characteristic of graphite; here there occurs a reaction between LiC_{12} and LiC_{18} that does not change the stage of intercalation[1] and little expansion is expected.

These results allow us to deduce a practical actuation energy density for oriented graphite as an actuation material, for comparison with other materials. As mentioned earlier (equation 1.9), the theoretical energy density $\frac{1}{2} E_e \varepsilon_f^2$ assumes that the actuation strain declines from its free strain value ε_f in direct proportion to the applied stress, reaching zero at the blocked stress. The data in Figure 3-3 suggests a lower limit to the blocked stress, possibly limited by deformation through basal slip of the graphite, of about 200 MPa. Taking the 6.7% strain measurement under 10 MPa as a minimum achievable free strain, we obtain an actuation energy density of 6700 kJ m^{-3} (3101 J kg^{-1}). While this is only 3.8% of the theoretical value of 175,000 kJ m^{-3} (81,000 J kg^{-1}), which would require a blocked stress of 3.5 GPa, it is more than one hundred times any existing electrically operated actuation mechanism and is comparable to shape-memory alloys.[5]

The actuation speed of the micromachined graphite is clearly limited by diffusion. Since diffusion time is proportional to the square of distance, smaller cross sections achievable with improved laser machining or other microfabrication processes are desirable and would allow not only faster lithiation, but also more complete lithiation and larger strain. This would raise the estimates of practical actuation energy density from the relatively conservative values above. By minimizing the amount of inactive material and orienting the graphite, much larger actuation strains and stresses are achievable than in commercial lithium rechargeable batteries.

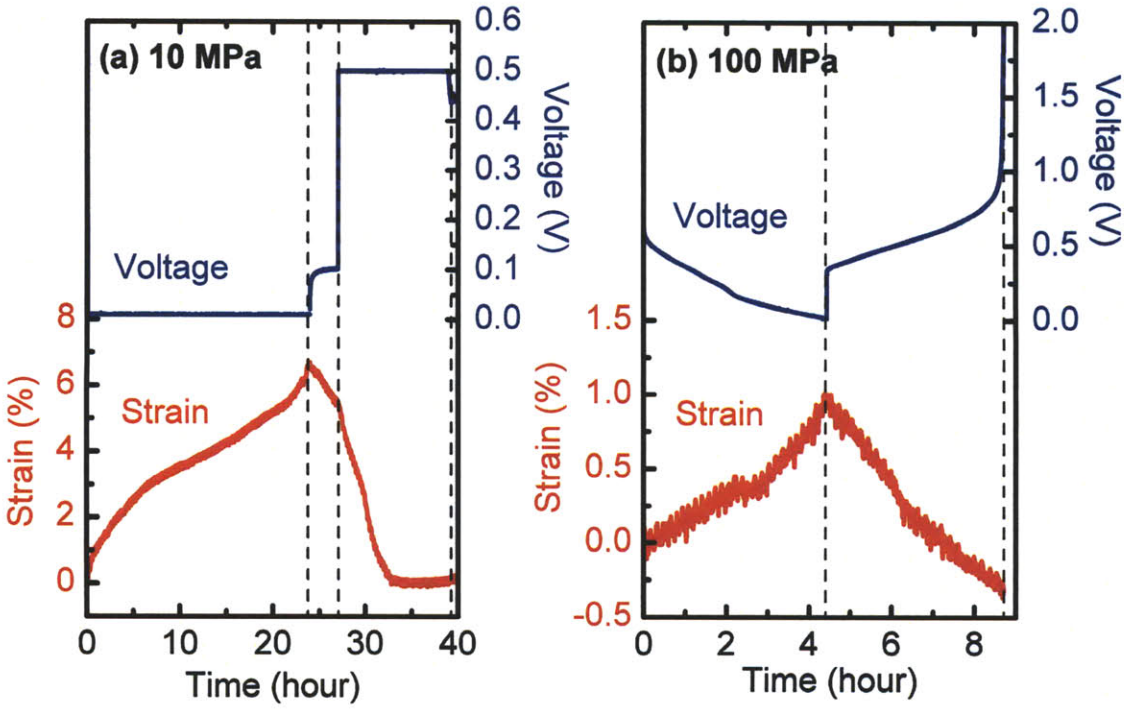


Figure 3-2. Electrochemically induced expansion and contraction of HOPG microactuator under various stress levels, shown against the corresponding cell voltage (li metal counterelectrode). (a) HOPG bonded to aluminum oxide substrate with Cu foil prior to laser micromachining. Against a 10 MPa constant stress, a constant voltage discharge at 0.01 V (~-0.1 V overpotential) results in 6.7% graphite expansion at a composition of $Li_{0.546}C_6$, producing mechanical work of 670 kJ m^{-3} (310 J kg^{-1}). The voltage relaxes to 0.1 V during an open-circuit hold, showing that the graphite is not Li saturated. The strain is completely reversed upon charging at a constant voltage of 0.5 V (~0.4 V overpotential). (b) Against 100 MPa stress, constant current test conditions resulted in lower, kinetically limited intercalation reaching 1.3% reversible strain and a mechanical work of 1300 kJ m^{-3} (602 J kg^{-1}).

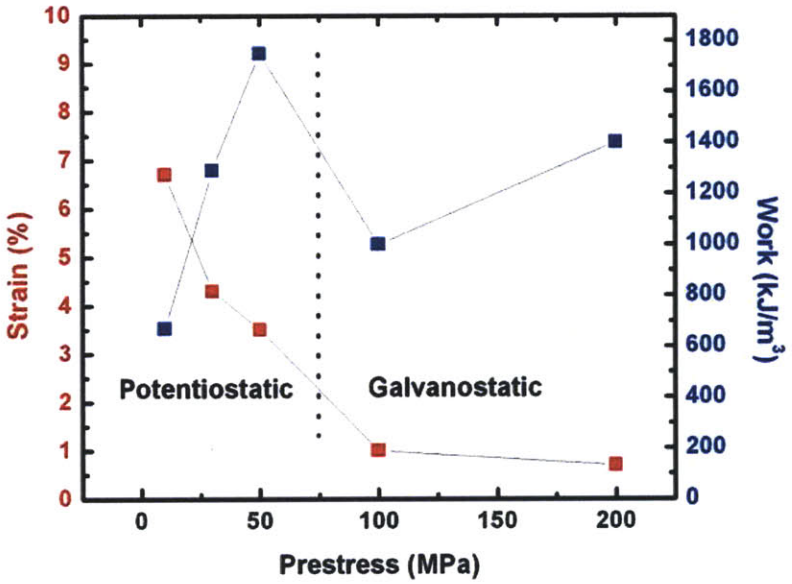


Figure 3-3. Summary of strain and work output of HOPG microactuators under various stress levels. At 50 MPa and below, actuators were tested under constant-voltage conditions. At 100 MPa and above, actuators were tested under constant-current conditions.

3.2 Calendared Electrodes

Although the large strains achievable using HOPG are promising, the bandwidth is clearly limiting. In an effort to combine the large strains with faster actuation from powder-based electrodes, this next set of experiments focuses on oriented powder-based electrodes in a conventional prismatic battery form factor.

3.2.1 Materials and Methods

Battery electrodes were formulated using lithium cobalt oxide (LCO) and graphite with a few weight percent by weight of poly(vinylidene fluoride)-based binder and conductive carbon additive. The LCO and graphite mixtures were cast from suspensions of the constituents in organic solvent onto aluminum and copper foil, respectively, as the positive and negative current collectors. The electrodes were dried and calendared to high

density, the procedure imparting some preferred [0001] orientation to the graphite negative electrode. Cells were assembled using a microporous polymer separator, a liquid electrolyte based on $LiPF_6$ salt in a mixture of non-aqueous solvents. Bilayer cells with a single pair of electrodes that had 34 mm x 50 mm footprints (Figure 3-4) were heat-sealed in an aluminum-polymer laminate packaging. Multilayer stacks containing 22 layers of electrodes were also fabricated and tested and sealed inside a metal can. The mechanical and electrochemical testing equipment were same used for the HOPG tests (section 3.1.1).

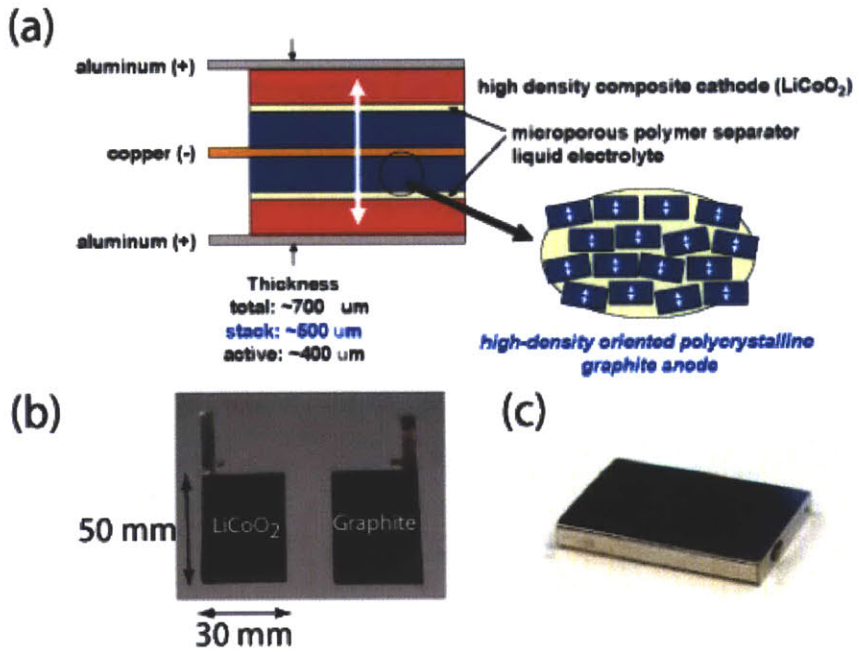


Figure 3-4. Schematic and photographs of a high-density electrode cell. (a) Schematic of a bilayer cell. The graphite anode has a preferential orientation even in powder-based form. (b) The individual electrodes of $LiCoO_2$ and graphite, measuring 30 x 50 mm. (c) Metal can holding a 22 layer stack of the high density electrodes with dimensions 6 x 30 x 50 mm.

3.2.2 Results and Discussion

Figure 3-5 shows strain versus charging time for a multilayer stack under 1 MPa stress, measured using a two stage constant current-constant voltage (CC-CV) protocol. The linear strain upon charging is 4.1%, nearly twice the expected strain for randomly oriented LCO and graphite (chapter 2), even though the measured capacity of the cell was only 86% of the theoretical value based on the active material mass. The higher-than-expected strain is attributed to the preferred orientation of the anode, which takes advantage of the anistropic expansion of the graphite as in the case of the HOPG samples. Much like in the commercial batteries, mechanical clamping of the active layers by the metal foils may reduce the in-plane expansion of the electrodes and increase the through-thickness strain. Figure 3-6 shows CC test results from a bilayer cell under stresses of 10 and 17 MPa. The strain decreased from the low stress value (3% at 1 MPa) with increasing stress, as did the capacity of the cell. At 10 MPa, the actuation strain was 2.3%, while the capacity of the cell decreased proportionally less being 93% of the value at 1 MPa. At 17 MPa, the actuation strain was 1.8%, while the capacity decreased to 76% of the 1 MPa value. Given that the strain varies nearly linearly with the capacity of these cells, the more rapid decrease in actuation strain than cell capacity with increasing stress suggests that internal strain-accommodation mechanisms are coming into play in the composite electrodes. At stresses greater than 20 MPa, the charging rate of the cells dropped precipitously, probably due to closure of the pores in the polymer separator. Assuming a practical blocked stress of 20 MPa (similar to that of commercial batteries) and a free strain of 4.1%, the actuation-energy density at the device level is 410 kJ m^{-3} (164 J kg^{-1}). This is several times greater (on a volume basis) that other electrically

actuated materials (piezoelectrics and electrostrictors), and, due to the low bulk density of the cells (~2500 kg m^{-3}), more than ten times greater on a weight basis. A clear advantage of the multilayer stacked actuator design is its similarity to prismatic lithium batteries, which would facilitate scalable fabrication. It is also clear that the actuation-energy density is limited more by the ability to function at higher blocked stresses than by the achievable strain.

These higher strain values, work capacities, and actuation-energy densities are made possible by the custom fabrication of these electrodes versus commercial lithium rechargeable batteries, as discussed in Chapter 2. Similar to the HOPG electrodes though, the biggest drawback is bandwidth. The higher density of the electrodes may limit electrolyte penetration reducing the active surface area of the electrodes and increasing diffusion lengths. The conventional assembly of these cells similar to commercial batteries yields a significant passive mechanical response.

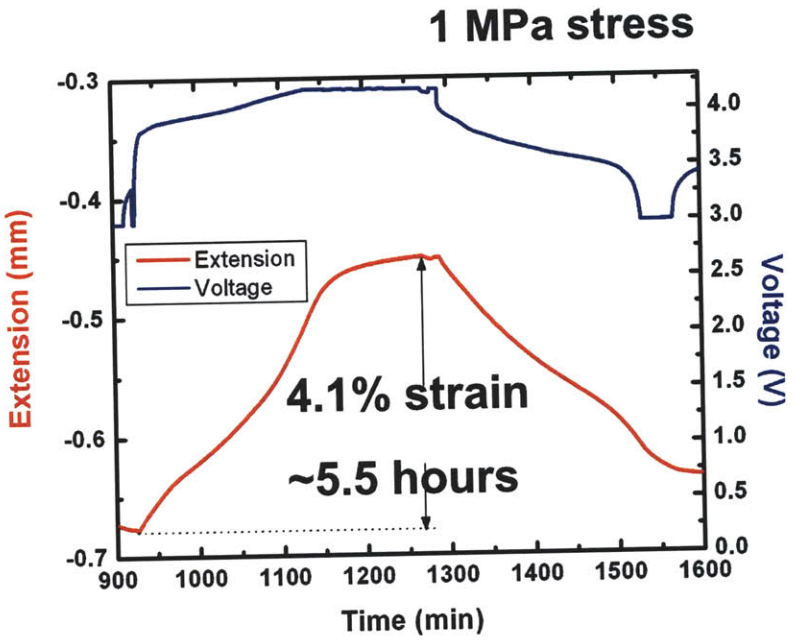


Figure 3-5. Under 1 MPa prestress, a 22 layer cell cycled under constant current-constant voltage conditions results in 4.1% actuation strain in 5.5 hours, significantly greater than commercial batteries.

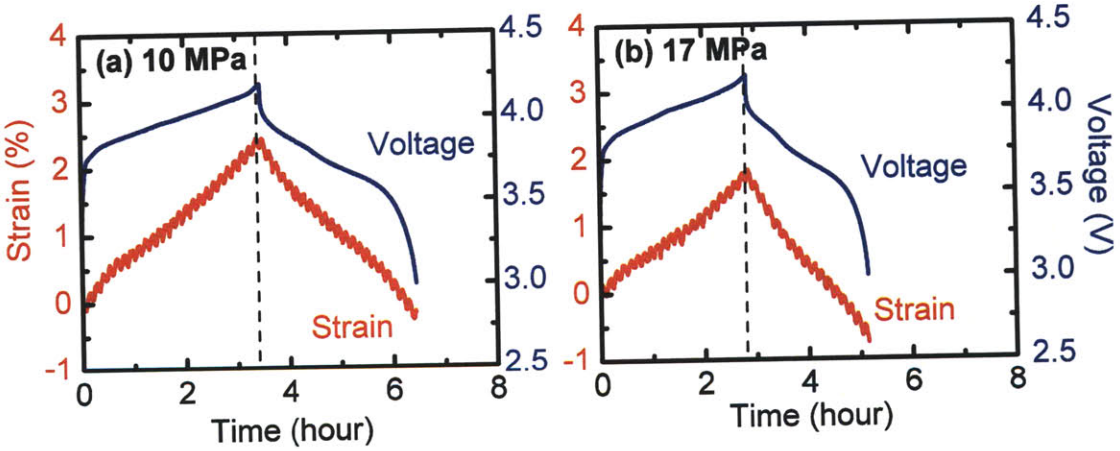


Figure 3-6. Strain and voltage profiles for a bilayer cell under (a) 10 MPa and (b) 17 MPa prestress, both cycled under constant current conditions between 3.0 – 4.2 V. Under 10 MPa, 2.3% actuation strain is achieved. This decreases to 1.85% under 17 MPa due to decreased cell capacity.

3.3 High-rate Actuation

In order to address the bandwidth limitations of electrochemical actuators up to this point, a change in the chemistry of the systems was implemented. There has been a keen interest in using $LiFePO_4$ as a cathode in the battery field for high power applications since early work in the late 90s.[6-9] Similarly, on the anode side, $Li_4Ti_5O_{12}$ has piqued interest due to its zero-strain behavior throughout its useful lithium composition range.[10] However, it's relatively high potential versus lithium metal (~1.55 V) decreases the amount of electrical energy available if it's used in a battery system. This is of little consequence for electrochemical actuators; it even serves to increase the efficiency as it reduces the overall input energy.

3.3.1 Materials and Methods

Battery electrodes were formulated similarly to the high density calendared electrodes (3.2.1), using conventional powder-based processing. $LiFePO_4$ (LFP) was used for the cathode while both $Li_4Ti_5O_{12}$ (LTO) and graphite were used as anode materials for separate experiments. The cells were assembled with a single pair of electrodes with a conventional microporous separator, and a $LiPF_6$-based electrolyte in non-aqueous solvents. The assembly was heat-sealed in an aluminum-polymer laminate packaging. Mechanical testing was conducted on an Instron 5567 materials testing machine and electrochemical control of the battery was performed by a Maccor 4300 battery tester, as mentioned previously.

As the primary goal for these cells were for high power, these were tested only under 1 MPa prestress using a CV protocol. The LFP/LTO cells were cycled between 0.8 and 2.7 V. The LFP/graphite cells were cycled between 2.0 and 4.8 V.

3.3.2 Results and Discussion

The displacement and voltage curves for the LFP/LTO cell is shown in Figure 3-7. Upon charging, the cell actually contracts as lithium moves from the LFP to the LTO according to the following reaction.

$$LiFePO_4 + Li[Li_{1/3}Ti_{5/3}]O_4 \rightarrow FePO_4 + Li_2[Li_{1/3}Ti_{5/3}]O_4 \quad (3.1)$$

The strain is fully recovered upon discharging. While the absolute displacement is small, the resulting strain is quite high at 2.3% since the battery consisted of only a single pair of electrodes. This was achievable in 230 seconds for single-stroke actuation. Assuming a 20 MPa blocked stress due to the conventional assembly of the cell, this equates to an actuation-energy density of 200 kJ m^{-3}. Accounting for the bandwidth, the power density is then 435 W m^{-3}.

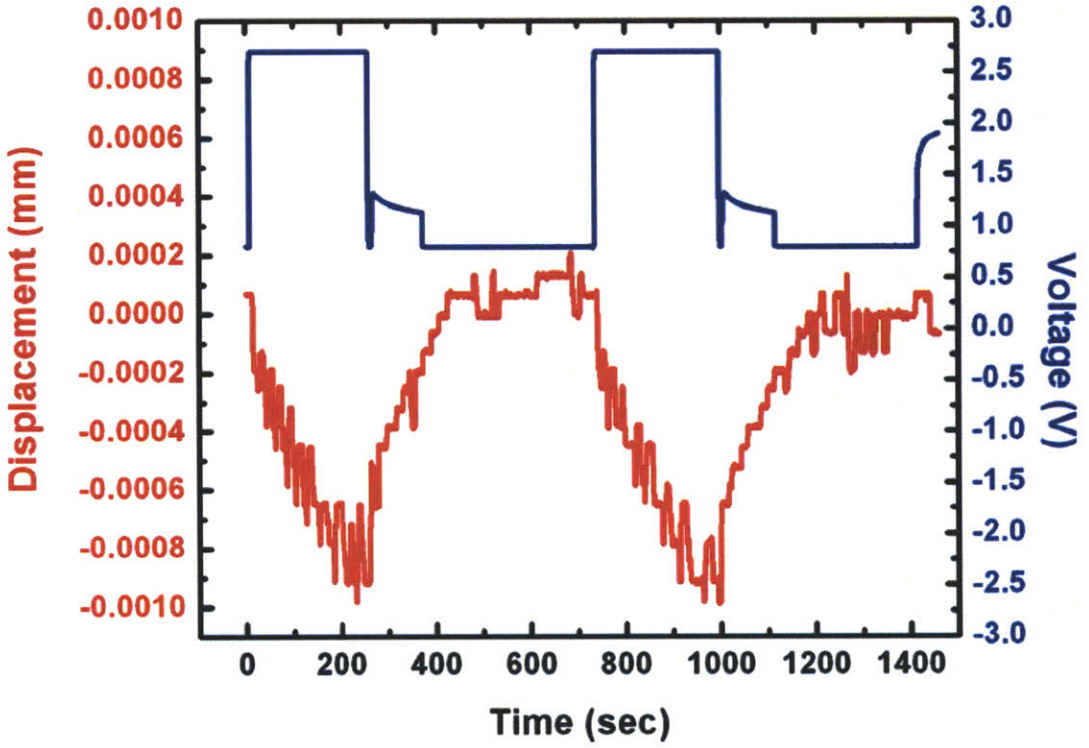


Figure 3-7. Strain and voltage profiles for a LFP/LTO cell undergoing constant-voltage cycling under 1 MPa prestress. This chemistry contracts upon charging and expands upon discharging, achieving a reversible strain of 2.3%.

Similar tests were conducted on the LFP/graphite cell with the results shown in Figure 3-8. The charging reaction is as follows:

$$6LiFePO_4 + 6C \rightarrow 6FePO_4 + LiC_6 \tag{3.2}$$

As the cell is charged, lithium ions move from the LFP to the graphite, creating a net expansion of the cell. Overall, 1.2% strain was achieved in 60 seconds for a single stroke actuation. The slower contraction of the cell is due to a slower discharge (less overpotential). While the actuation-energy density drops to 120 kJ m^{-3} (compared to 200

kJ m^{-3} for the LFP/LTO cell), the power density actually increases substantially to 1000 W m^{-3} due to the increased bandwidth.

Further optimizations to increase the power density could prove even more beneficial. Reduction in particle sizes of the electrodes would serve to decrease the diffusion lengths, decreasing the overall cycling times. Further, moving away from conventional battery assembly and geometries could also lead to improvements such as an increased blocked stress and a reduction of inactive materials so the device strain is more comparable to the active material expansion.

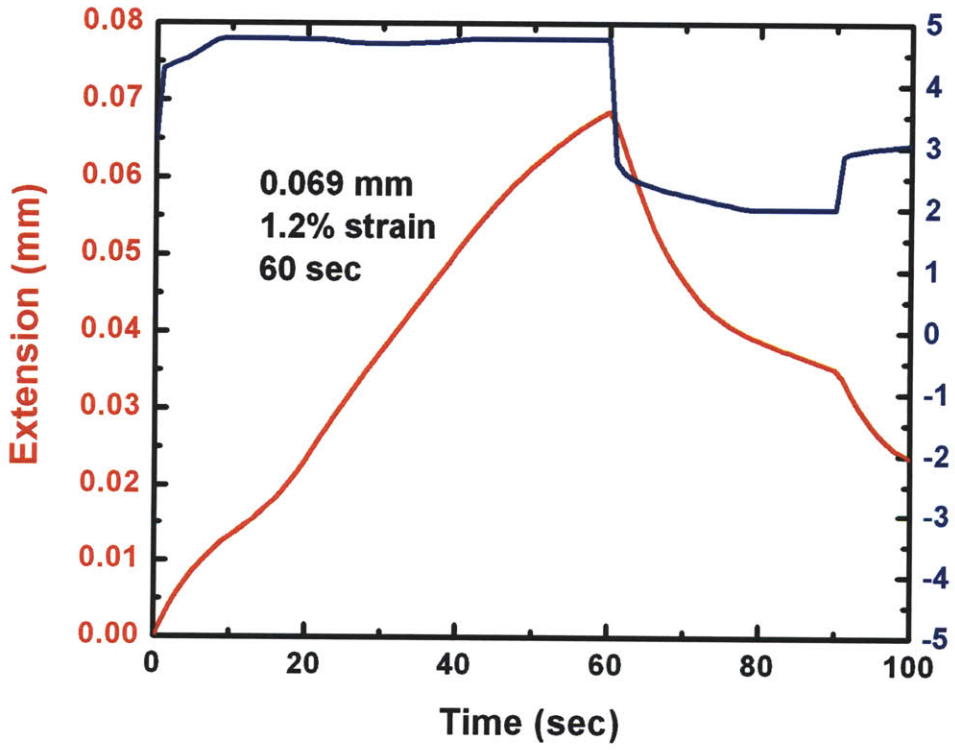


Figure 3-8. Displacement and voltage profile for a LFP/graphite cell under 1 MPa prestress undergoing constant-voltage cycling. The actuation strain of 1.2% is achieved in 60 seconds.

3.4 Summary

While commercially available lithium rechargeable batteries provide surprising actuation performance, a use for which they are not intended, there are optimizations that can be made to increase their performance. Actuation energy density can be maximized by minimizing the soft components in series with the actuation direction (Figure 3-9). The anisotropic expansion of certain materials, particularly graphite, can also be utilized by using preferentially oriented electrodes. Further, different material systems can provide improved energy and power densities, which remain to be explored in full.

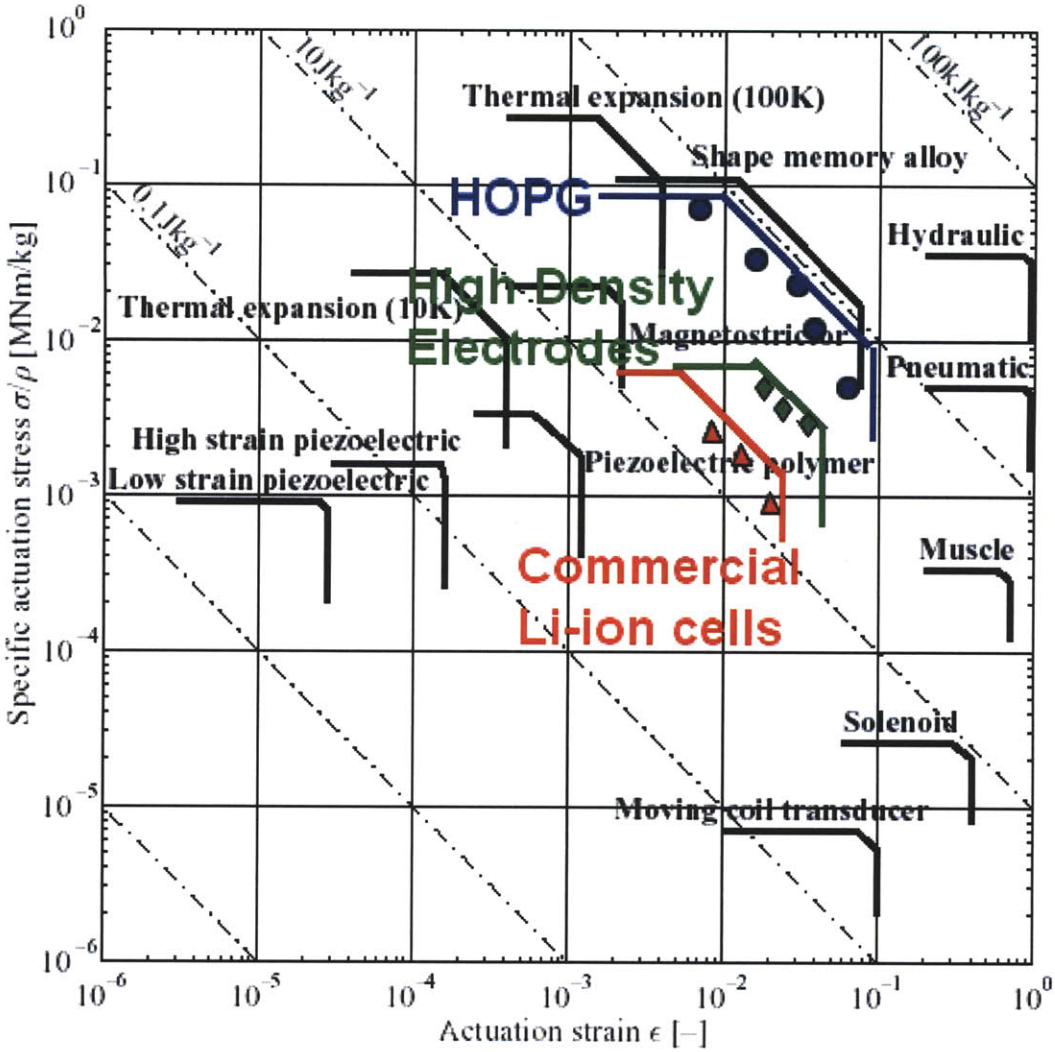


Figure 3-9. Comparison of specific actuation stress versus actuation strain for actuation technologies.[5] Diagonal lines are lines of constant specific actuation energy. Electrochemical actuators have the largest specific actuation energy of any electrically operated mechanism.

3.5 References

1. Ohzuku, T., Iwakoshi, Y. & Sawai, K. Formation of lithium-graphite intercalation compounds in nonaqueous electrolytes and their application as a negative electrode for a lithium ion (shuttlecock) cell. *Journal of the Electrochemical Society* **140**, 2490 - 2497(1993).
2. Yu, P. et al. Determination of the Lithium Ion Diffusion Coefficient in Graphite. *Journal of The Electrochemical Society* **146**, 8-14(1999).
3. Nunes, B. Edge-defined film-fed growth of single-crystal piezoelectrics. (2001).

4. Woo, K.C. et al. Effect of In-Plane Density on the Structural and Elastic Properties of Graphite Intercalation Compounds. *Phys. Rev. Lett.* **50**, 182(1983).
5. Huber, J., Fleck, N. & Ashby, M. Selection of mechanical actuators based on performance indices. *Proceedings of the Royal Society of London, Series A: Mathematical, Physical and Engineering Sciences* **453**, 2185-2205(1997).
6. Chung, S., Bloking, J.T. & Chiang, Y. Electronically conductive phospho-olivines as lithium storage electrodes. *Nature Materials* **1**, 123 - 128(2002).
7. Nanjundaswamy, K.S. et al. Synthesis, redox potential evaluation and electrochemical characteristics of NASICON-related-3D framework compounds. *Solid State Ionics* **92**, 1 - 10(1996).
8. Padhi, A.K. et al. Effect of structure on the Fe3+/Fe2+ redox couple in iron phosphates. *Journal of the Electrochemical Society* **144**, 1609 - 1613(1997).
9. Padhi, A.K., Nanjundaswamy, K.S. & Goodenough, J.B. Phospho-olivines as positive-electrode materials for rechargeable lithium batteries. *Journal of the Electrochemical Society* **144**, 1188 - 1194(1997).
10. Ohzuku, T., Ueda, A. & Yamamoto, N. Zero-Strain Insertion Material of Li[Li[sub⅓]Ti[sub 5/3]]O[sub 4] for Rechargeable Lithium Cells. *Journal of The Electrochemical Society* **142**, 1431-1435(1995).

4 Actuation Based On Electrochemical Alloying

The second class of actuators is based on electrochemical alloying of lithium with a host metal, which often results in molar volume expansions past 300%, in contrast to the few percent expansion achieved by lithium intercalation. This gives way to a separate class of actuators capable of extremely large displacements in a lightweight package. In this chapter, we discuss how we take advantage of this actuation mechanism and model the resulting mechanical behavior.

The new actuator operates as an electrochemical analogue to the bimetal strip, generating out-of-plane bending by utilizing a difference in chemical expansion rather than thermal expansion. Rather than utilizing the volume expansion directly, this design uses a displacement amplification mechanism. It is comprised of a host metal working electrode (typically aluminum or tin) and a lithium metal counterelectrode sandwiched around an insulating separator. Upon discharge, a lithium intermetallic forms on the surface of the working electrode, creating a bi-layer, unimorph structure within the electrode (Figure 4-1a). The intermetallic has a larger molar volume per host atom creating a mismatched strain between the layers and inducing significant out-of-plane-bending of the disc, concave away from the lithium (Figure 4-1a). The amount of bending is controlled by the thickness of the intermetallic film which can be calculated from the capacity (Equation (1.4)). The conversion will be detailed in section 4.3.

This leads to multiple modes of deformation that are intrinsically self-amplifying. The bending manifests itself initially as a spherical cap (Figure 4-1b). Further actuation tends to lead to "bottlecapping," a non-uniform deformation with increased curvature near the edges of the device relative to the center (Figure 4-2a). Over long discharge

periods, the curvatures bifurcate and the sample appears to 'fold' (Figure 4-2b). Folding can also be controlled by manipulating the reaction area of the electrode and will be discussed later. The mechanical mechanisms behind these deformation modes will be discussed in section 4.2.2.

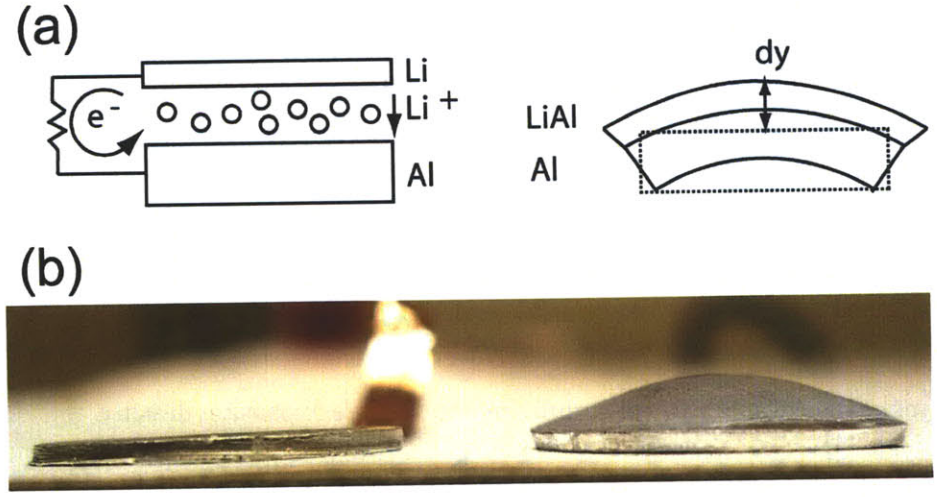


Figure 4-1. (a) Schematic of a lithium-aluminum actuator. Upon discharge, lithium ions are stripped from the lithium electrode and form an alloy on the surface of the aluminum electrode, creating a unimorph structure. The increased molar volume induces bending shown on the right. The separator is omitted for clarity. (b) A sample before discharge (left) and after discharge (right) illustrating the deformation.

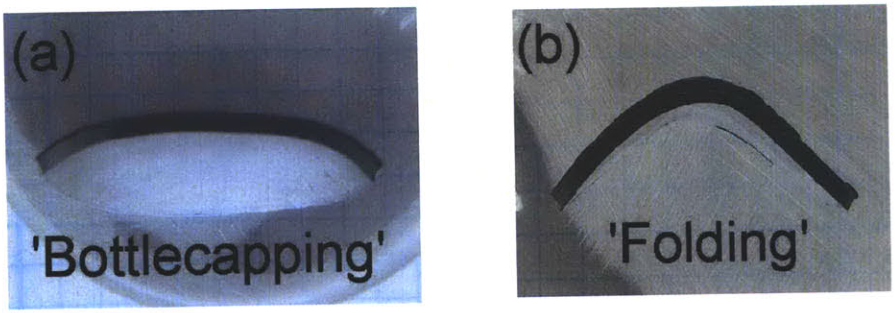


Figure 4-2. Cross sections of aluminum-based actuation elements illustrating (a) "bottlecapping" and (b) "folding" deformation modes.

4.1 Test Setup

An electrochemical actuation device is typically packaged and sealed inside a metallized polymer pouch, adding a counterelectrode and separator in series with the active actuation electrode. In order to better characterize the intrinsic displacement of the active aluminum electrode, open cell tests were run in an argon-filled glove box. Here, the cell components were placed in a beaker and flooded with electrolyte. A lithium metal electrode was on the bottom of the beaker followed by a separator and then an aluminum working electrode (active actuation element), allowing the aluminum to deform concave up without any restrictions (Figure 4-3). The electrodes were spot-welded to copper strips acting as current collectors. Upon discharge, lithium will react with the surface of the aluminum forming LiAl (verified in Chapter 5), which has a 93% increase in molar volume per aluminum atom. Assuming this expansion is isotropic (both Al and LiAl are based on cubic lattices), this corresponds to a 25% uniaxial expansion. This creates significant stress and induces the bending.

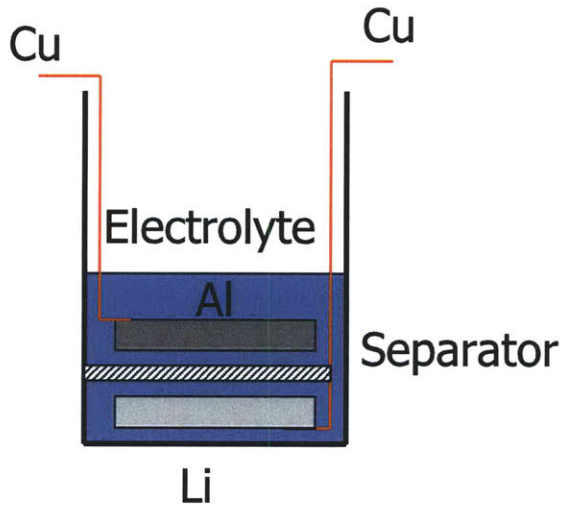


Figure 4-3. Schematic of the open cell test setup.

Two different types of samples were tested. The first type was a disc actuator, ¾-in in diameter and 1.0 mm thick (Figure 4-4 left). The second type was a controlled folding rectangular actuator, nominally 22 x 26 mm and 1.5 mm thick. The sample was masked such that there was only a ¼-in wide strip across the short width of the sample that was exposed for reaction which would ensure folding along this axis while the masked areas would provide displacement amplification (Figure 4-4 right).

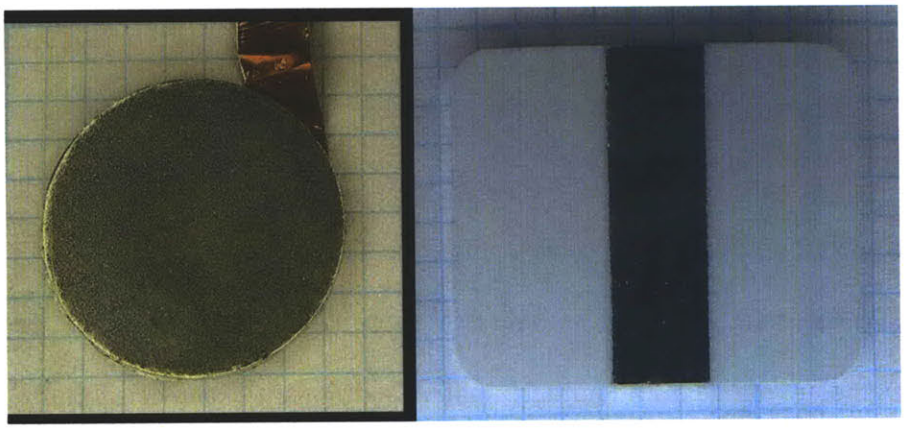


Figure 4-4. Disc actuator (left) and controlled folding rectangular actuator (right). The edges of the rectangular actuator are masked so the reaction is limited to the center strip which is ¼ in wide and 22 mm long while the masked regions provide displacement amplification.

For comparison, these open cell experiments will be compared to those of packaged actuators where the same components have been vacuum-sealed in a metallized polymer laminate pouch. Further details of these packaged actuators will be described in Chapter 5. The displacement for the packaged disc actuators was measured continuously using a spring-loaded linear variable differential transformer (LVDT) inductive gaging sensor (Micro Epsilon DTA-3G-1.5-CA) which applies a nominal force of 100 g (1 N) to the actuator. Packaged controlled folding rectangular actuators were tested under discrete loads (up to 800 g) and measured using a Keyence displacement sensor.

4.2 Results and Discussion

4.2.1 Actuation of Discs

The ¾-inch diameter aluminum disc electrode was discharged at 10 mA in 1 hour increments, between which displacement measurements were taken, up to a total of 100 mAh. These results are compared to a packaged actuator that was discharged continuously at 10 mA to the same capacity. The displacement for the open cell configuration is about 40% greater than displacement for the packaged cell (Figure 4-5). The packaging and load from the LVDT suppress the deformation, acting in the opposite direction of the bending moment imposed by the intermetallic film. Therefore, a thicker intermetallic film (greater discharge capacity) is required to generate the necessary bending moment to achieve a given deformation for the packaged sample. The bending moment per unit length around the periphery, M, introduced by the film growth is:

$$M = \frac{1}{2} h_s \varepsilon_m M_f h_f \tag{4.1}$$

where h_s is the substrate thickness, ε_m is the mismatch strain between the film and the substrate, M_f is the biaxial modulus of the film, and h_f is the film thickness. The total bending moment, depending on the thickness of the film, is generally on the order of 10^{-1} to 10^{-2} N m. The bending moment per unit length, M_r, imparted by the load, P, from the LVDT applied to the center of the disc is[1]:

$$M_r = \frac{P}{4\pi}(1+\nu)\log\frac{a}{r} \tag{4.2}$$

where ν is Poisson's ratio, a is the radius of the disc, and r is the distance from the center of the disc. The bending moment is at a maximum near the center of the disc and the total

moment is approximately 0.01 N m, acting oppositely to the bending moment imparted by the film. This is not insignificant at early stages of film growth and will depress deformation and, particularly, the onset of deformation. The lithium counterelectrode and separator will also be in series with the actuation, but their contribution to the overall stiffness is likely small. However, these forces will also act against the film moment, reducing the overall displacement compared to the open cell as is observed.

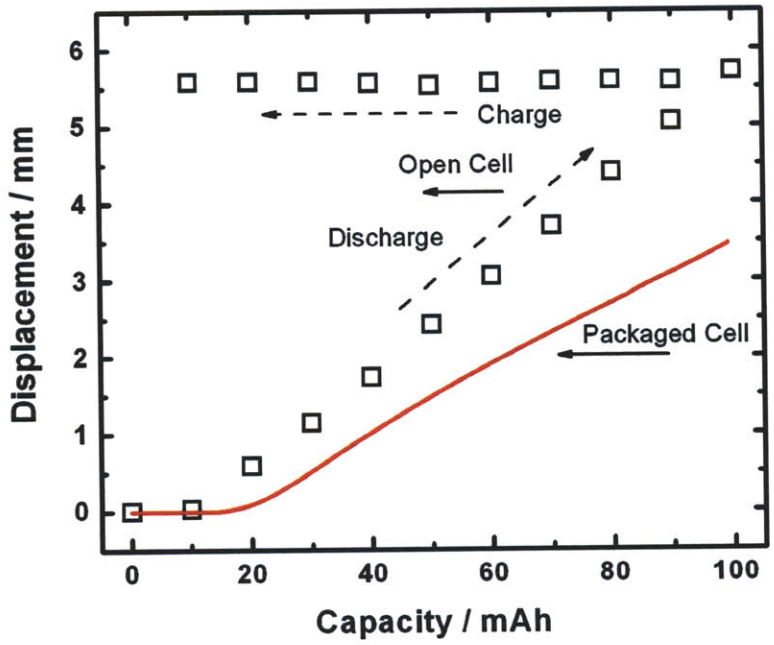


Figure 4-5. Comparison in displacement between an open cell and packaged cell. The open cell shows 40% more displacement than the packaged cell at capacities greater than 40 mAh. Upon charge, only 0.1 mm of displacement is recovered upon charging indicating a majority of the displacement is a result of plastic deformation.

The open cell sample was also charged in a similar manner, de-alloying lithium from the LiAl and plating it back out on the lithium metal electrode (Figure 4-5). Only 0.1 mm displacement was recovered and this occurred only after the first charge step. The

displacement remained unchanged for the remaining 90 mAh charge process. This verifies that virtually all of the displacement during discharge results from plastic deformation.

Cross-sectioning the re-charged sample shows a porous region at the surface of the aluminum to a depth equal to the lithium penetration depth (Figure 4-6). This has been observed in literature[2] as well and is attributed to the large volume changes during lithiation. During de-lithiation, the aluminum is unable to coalesce together to the original microstructure, resulting in cracks and voids. The Vickers hardness in the porous region was measured at 27.14 +/- 5.14 kg mm^{-2}, slightly harder than the aluminum substrate at 21.49 +/- 1.81 kg mm^{-2}. This hardness increase is likely due to the small amount of lithium remaining in this layer since it was not fully charged.[3]

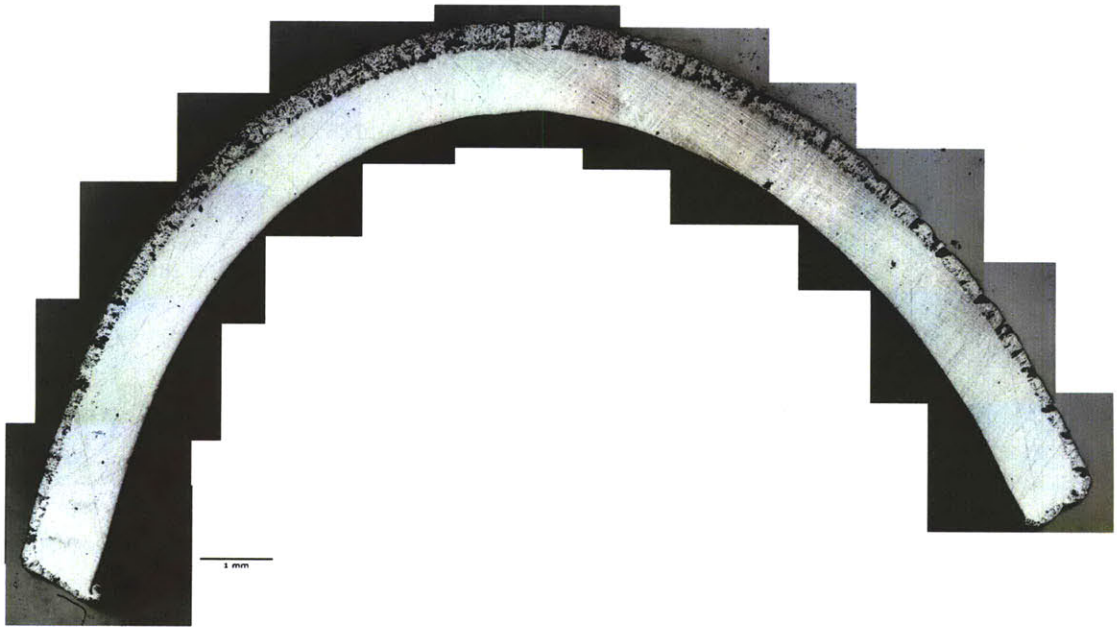


Figure 4-6. Cross section of an aluminum disc-shaped actuator after discharging to 100 mAh and recharging 90 mAh (final discharge capacity of 10 mAh) showing the principal curvature axis of larger curvature. Significant permanent damage is seen on the top surface where the lithium intermetallic had formed. The scale bar is 1 mm.

One drawback of using an open cell is that as the aluminum deforms, the edges pull away from the lithium creating a larger electrolyte gap and limiting the reaction. As seen in Figure 4-6, the penetration depth of the lithium is around 350 μm near the center of the sample compared to only 200 μm near the edges. The total thickness of the sample also varies along the sample. In the center, the total thickness is now 1.3 mm thick whereas it is only 1.1 mm thick at the edges indicating non-uniformity in the reaction. The amount of thickness increase also points to anisotropic volume expansion, primarily being accommodated for by expanding in the thickness direction.

4.2.2 Actuation of Controlled-Folding, Rectangular Actuator

An open cell test was also conducted on a 1.5 mm thick rectangular controlled folding aluminum sample, again discharging at 10 mA in 1 hour increments. Contrary to the open cell results for the disc, the displacement curve for this followed nicely with those for a similar packaged actuator under mechanical loads of up to 400 g (Figure 4-7), indicating that the internal stiffness of the aluminum itself dominates over that added by the packaging and external loads. The bending stiffness per unit peripheral length, D, for cylindrical bending is given by[1]:

$$D = \frac{Eh^3}{12\left(1-\nu^2\right)} \tag{4.3}$$

where E is the Young's modulus and υ is the Poisson's ratio. Here we see the effective modulus for cylindrical bending, $E/(1-\nu^2)$. For spherical bending, the effective modulus would be $E/(1-\nu)$. An increase in thickness of 50% over the disc samples increases the bending stiffness by 338%, much greater than the 50% increase in bending moment imparted by the film growth, explaining the internal stiffness limitation of these

rectangular controlled folding samples. Both the packaged and open cell rectangular controlled folding actuators were pre-lithiated to 15 mAh (galvanostatic discharge at 10 mA for 1.5 h) before actuation, generating some plastic deformation in these samples before the measured actuation curves. This open cell was discharged to 250 mAh which imparted a near-180 degree bend in the sample (Figure 4-8).

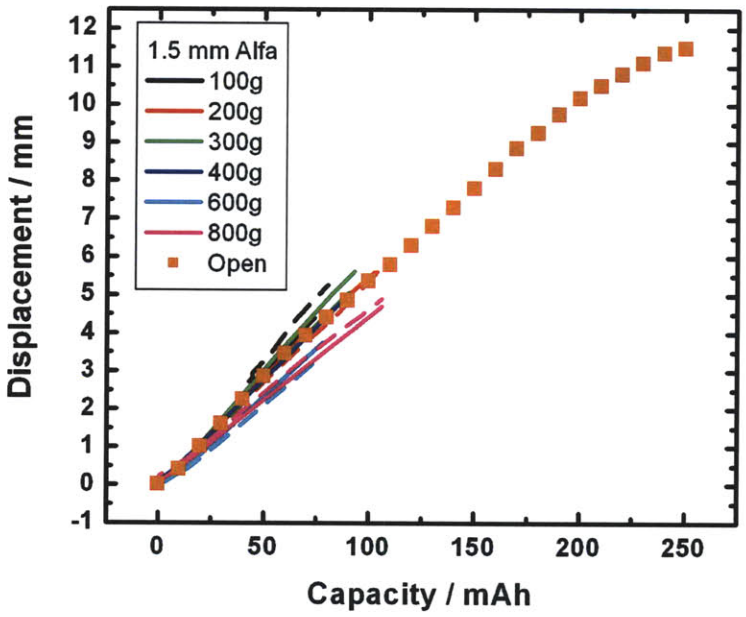


Figure 4-7. Comparion of an open cell sample (squares) to packaged samples (lines, at different external mechanical loads) of a controlled folding, rectangular actuator. Two separate samples (solid and dashed lines) are shown at each load. Similar displacements are seen for both types of samples.



Figure 4-8. Cross section of a controlled folding, rectangular aluminum actuator. This sample folded nearly 180 degrees in 250 mAh of discharge. The scale bar is 1 mm.

With the smaller reaction area of these samples, the areal discharge capacity density (see Equation (1.5)) is over twice as much as any disc sample tested. However, this does not manifest itself in the intermetallic film thickness, as the average thickness is only 441.6 μm although there are regions over 800 μm. More interesting is that less than 300 μm of aluminum has been reacted. In comparison, full disc samples show much

greater depths of reacted aluminum even when discharged to much lower capacity densities. This indicates that some of the current is not going into forming the intermetallic reaction product but may be contributing to non-Faradaic processes such as electrical double-layer charging due to the larger electrolyte gap formed by the sample deforming away from the lithium metal electrode and separator.

4.3 Actuation Modeling

Bending in a film/substrate system has been investigated to a great extent for microeletromechanical systems (MEMS) and in electronics processing.[4] Typically elastic strains arise during epitaxial film growth due to lattice mismatch or thermal cycling. Here, we have a similar structure with a LiAl film on an aluminum substrate (Figure 4-9) so the bending can be analyzed in a similar manner.

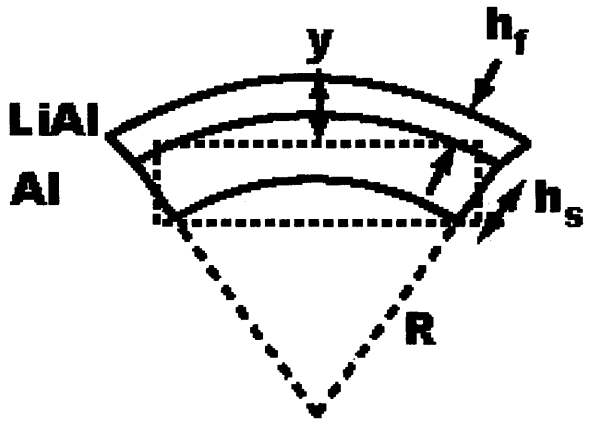


Figure 4-9. Schematic of a cross section of an actuator undergoing bending. The vertical displacement, film thickness, substrate thickness, and radius of curvature are labeled.

In order to predict the expected displacement, it is necessary to first determine the curvature. In calculating the curvature, κ, three regimes can be distinguished as the bending progresses. Initially, the deformation is linear with respect to the film thickness

and the curvature is spherical. This regime is accurately described by analysis based on Stoney's equation:

$$\kappa = \frac{6M_f \varepsilon_m h_f}{M_s\left(h_s^2 + h_f h_s\right)} \tag{4.4}$$

where M is the effective modulus, ε_m is the elastic mismatch strain, h is a layer thickness, and the subscripts f and s refer to the film and substrate, respectively. The curvature is equal to $1/R$ where R is the radius of curvature (Figure 4-9). The effective modulus depends on the mode of deformation. For spherical deformation, $M = E/(1-\nu)$ and for cylindrical deformation $M = E/(1-\nu^2)$, where E is the Young's modulus and ν is Poisson's ratio. The following values are used for the LiAl on Al system: M_f is 44.9 GPa,[5] υ_f is 0.35,[5] M_s is 70 GPa,[6] and υ_s is 0.34.[6] The bending eventually transitions to non-linear behavior (described earlier as 'bottlecapping', see Figure 4-2a) although the curvature remains axially symmetric. Here, the substrate midplane has to deform extensionally in order to maintain a spherical cap shape and contributions from rotation to the strain can be as significant as the linear effect. The stiffness against extension is much greater than the stiffness against bending, therefore the curvature is reduced relative to the linear model for a given film thickness. In addition, although the deformation may be axially symmetric, the curvature distribution along a radius is not uniform. Greater curvature is observed near the edges and smaller curvatures are observed near the center of the disc. Further actuation will lead to cylindrical bending, or bifurcation, since this can occur without any midplane extension. In this case, the deformation becomes asymmetric with the curvature increasing in one direction and decreasing in an orthogonal direction. In the limiting case, the sample takes a cylindrical shape as one of the principal curvatures approach zero and it is clear the non-zero curvature will be the only contribution to the

deflection. Taking a cross-section perpendicular to the zero curvature axis, this can appear as 'folding' as seen in Figure 4-2b.

Exact general solutions in the non-linear and bifurcation regimes require numerical methods. Simplified solutions for special cases exist for the non-linear regime though. However, at present, we will extend the linear model expecting an overpredicted displacement through the non-linear regime. The limit of bifurcation will be discussed in more detail later.

If the sample does not have a high degree of symmetry, the principal curvatures are unequal from the onset of deformation. For example, given a rectangle with edge lengths L_x and L_y such that $L_x > L_y$, there will be a larger principal curvature along the longer dimension L_x. In this way, it is possible to control the 'folding' shape of an actuator, which was seen in Chapter 4.2.2 above for the masked sample and will be further discussed in Chapter 6.

The calculated curvature can be translated to a vertical displacement for both a disc and controlled folding rectangular sample using a simple profile of circular geometry (Figure 4-10).

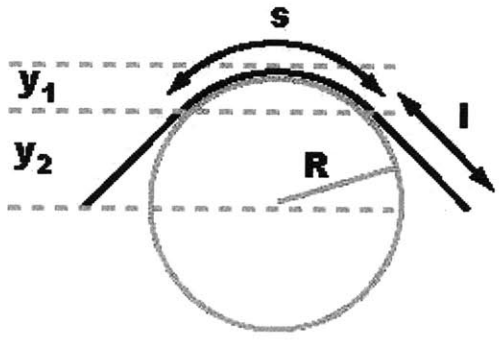


Figure 4-10. Schematic of an actuator cross-section fit to a circular profile with radius R, arc length s, and lever arms l contributing to displacements y_1 (for a disc actuator alone) and y_2 (for a controlled folding actuator).

Assuming a constant arc length, s, equal to the diameter of a disc or the width of the reaction area for the controlled folding rectangle, the vertical displacement, y, can be calculated as:

$$y = \frac{1}{\kappa}\left(1 - \cos\left(\frac{s\kappa}{2}\right)\right) \tag{4.5}$$

For controlled folding actuators, where the reaction area is limited by masking off certain sections of the sample, the amplification is accounted for by:

$$y = \frac{1}{\kappa}\left(1 - \cos\left(\frac{s\kappa}{2}\right)\right) + l\sin\left(\frac{s\kappa}{2}\right) \tag{4.6}$$

where l is the length of the masked 'leg' or 'lever arm' providing the amplification. The constant arc length assumption is equivalent to assuming there is a neutral axis in the aluminum substrate which is not stretched or compressed during deformation.

While the Stoney equation provides exceptional analysis for systems undergoing small strains in the elastic range, these results are not expected to accurately extend to large plastic deformations. Hence, we look to account for plasticity by assuming an elastic-perfectly plastic behavior and using 'effective' plastic moduli based on the yield strength of the materials to provide an upper bound for the deformation of these actuators while the elastic analysis should provide a lower bound. The yield strengths can be determined from the hardness values of the materials. Vickers hardness testing on two samples galvanostatically discharged to 100 mAh at 1 and 10 mA gave hardness values HV_{Al} = 25.88 +/- 1.76 kg mm^{-2} and HV_{LiAl} = 54.92 +/- 3.69 kg mm^{-2}. While the aluminum value is slightly greater than the one measured for the open cell sample, for comparison it is better to take these values as they were measured at the same time on the same sample. As the hardness is directly proportional to the yield strength,[7] σ_y:

$$HV = 2.9\sigma_y \tag{4.7}$$

the yield strengths are calculated to be $\sigma_{y,Al} = 86$ MPa and $\sigma_{y,LiAl} = 183$ MPa. The yield strength for the intermetallic is relatively low and the material is known to be brittle, fracturing in the elastic regime.[8] Closer observation of the micrsotructure reveals cracking within the intermetallic film, indicative of failure from high compressive stresses. As such, the use of effective plastic moduli for both the film and the substrate is justified. The effective plastic modulus is the yield strength divided by the strain of the material. However, as the curvature only depends on the ratio of the moduli and the strains should be similar to a first aproximation, the yield strength values can be used.

Another difficulty is determining how h_f and h_s vary during discharge. At one extreme, we can consider the LiAl film depositing on top of the substrate. At another extreme, we can consider that the LiAl corrodes the substrate and the total thickness remains constant. From the cross-sections, it is apparent the real case lies somewhere between these two scenarios. It is clear the aluminum substrate is being corroded away, but the total thickness increases, accommodating the volume expansion of the LiAl. This gives another set of two bounding limits, either consider a constant substrate thickness (lower bound) or constant total thickness (upper bound).

For epitaxial film growth, elastic mismatch strain is defined by the difference in lattice parameters of the film and substrate with respect to the film. Here, we must use something else because we cannot assume isotropic expansion. The 25% uniaxial expansion calculated earlier assumes isotropy and clearly does not manifest itself in the system as a majority of the volume expansion is accommodated out-of-plane. Using this for the mismatch strain grossly overpredicts the displacement. Given that the film

thickness can be very well calculated using the original reaction area (shown in Chapter 5), there is clearly minimal in-plane expansion. From typical cross-sections of pre-bifurcation samples, the surface strain relative to the midplane ranges between 0.0 – 0.08. For the purposes of this model, a mismatch strain of 0.04 will be used.

It is also necessary to relate the film height h_f to capacity, Q, or areal capacity density, q, in order to correlate the models with the measured data. The capacity, or amount of lithium that has been reacted, is measured in mAh. This is easily converted to coulombs which further can be converted to moles of lithium by the Faraday constant (96485 C mol^{-1}). As the reaction product is LiAl, the number of moles of lithium reacted equals the number of moles of LiAl formed. Using the molar volume of LiAl (1.95 x 10^{-5} m^3 mol^{-1}) we know the volume of the intermetallic film. Further dividing by the reaction area yields the thickness h_f of the intermetallic film. Leaving out this last step would convert the areal capacity density q to film thickness h_f. For a ¾ in diameter disc, the reaction area is 2.85 cm^2 and the conversion factor is 2.55 x 10^{-6} m/mAh. For the controlled folding rectangle, the reaction area is 1.397 cm^2 and the conversion factor is 5.21 x 10^{-6} m/mAh. By using the original reaction area of the sample, we are further assuming no in-plane extension.

From Equations 4.4, 4.5, and 4.6, we can plot the predicted behavior of the actuators (Figure 4-11 for disc actuators and Figure 4-12 for controlled folding rectangular actuators). Each plot has four calculated displacements combining the two options from two parameters: elastic or plastic moduli and constant substrate thickness or constant total thickness. Table 1 summarizes the geometric-dependent variables used in these models while Table 2 lists the material properties used. The constant total thickness

case predicts greater displacements than does the constant substrate thickness case. This is expected as the thickness ratio between the film and substrate is increasing at a faster rate, thereby also increasing the curvature and displacement at a faster rate. Using the elastic moduli, both the constant substrate thickness and constant total thickness models dramatically underpredict the displacement of both of the actuators. This is also expected as virtually all of the deformation is plastic. Displacement calculated from the effective plastic moduli and the constant total thickness constraint though agrees closely with the data in both cases, particularly at lower capacities. Further references will be made only to this model assuming effective plastic moduli and constant substrate thickness.

Table 4-1. List of variables used in the models for the two different geometries of actuators.

Geometry	Arc length mm	Lever arm mm	Reaction area cm^2	Thickness conversion μm/mAh
Disc	19.05	0	2.85	2.55
Controlled Folding	6.35	9.825	1.397	5.21

Table 4-2. List of material properties used in the displacement models.

Mismatch strain	Elastic moduli		Plastic moduli	
	M_s	M_f	M_s	M_f
4%	70 GPa	44.9 GPa	183 MPa	86 MPa

For the disc actuator (Figure 4-11), the maximum predicted displacement from the model is 6.9 mm at 124 mAh. The expected displacement for a perfect hemisphere would

be 6.1 mm (0.01905 m / π) which occurs at 94 mAh, so the model is predicting a slightly larger maximum displacement than this as the hemisphere would start curling underneath itself. In the extreme case, the model predicts the sample to form a sphere. Even though the sample has bifurcated, the cross-section in Figure 4-6 was taken parallel to the larger curvature axis and has taken a shape approximating that of a semicircle, which is a cross-section of a hemisphere. The curvature is rather uniform across the diameter of this cross-section. The measured displacement of 5.71 mm is not far off the predicted 6.1 mm for this shape, especially considering the cross-section isn't a perfect semicircle. This model remains reasonably valid as long as the curvature is uniform along the radius of the larger principal curvature axis. Upon severe folding, the curvature will be significantly greater near the center of the sample relative to the ends, invalidating the model. The measured displacements at this point will increase significantly (Figure 4-13 and Figure 4-14). The model predicts a perfect hemisphere to be reached at 94 mAh, however, this still hasn't occurred by 100 mAh of discharge on the open cell sample. The model does not account for an initial film formation and predicts immediate bending, whereas the measured displacement is 0.03 mm after 10 mAh before the displacement starts increasing at a more appreciable rate. This delay is associated with nucleation and growth of the intermetallic film before enough stress is generated across the sample to induce significant deformation. This delay accounts for the discrepancy in capacity for the semicircular cross-section. The slopes of the model and data are very similar, so shifting the model to account for this incubation would place it virtually on the data.

For the controlled folding actuator (Figure 4-12), deformation is cylindrical from the onset; that is, there are two axes of principal curvatures and one the curvature is

significantly larger in one direction than the other. Here the maximum measured displacement is 11.5 mm whereas the maximum calculated displacement is 11.87 mm, assuming the reaction width bends to a perfect semicircular profile. The cross-section in Figure 4-8 shows the left lever arm slightly lower than the right one, indicating the bending may have been slightly off-center. The lever arms are also not completely parallel. These discrepancies from ideal account for the reduced measured displacement. At around 100 mAh, the measured data begins to diverge from the model. This may be due to the aluminum bending away from the lithium so the intermetallic does not form uniformly across the whole reaction area and does not induce as much bending. Additionally, from the cross-section in Figure 4-8, the film thickness was observed to be less than expected for the given capacity, likely due to the current contributing to non-Faradaic processes, which would also serve to keep the measured displacement lower.

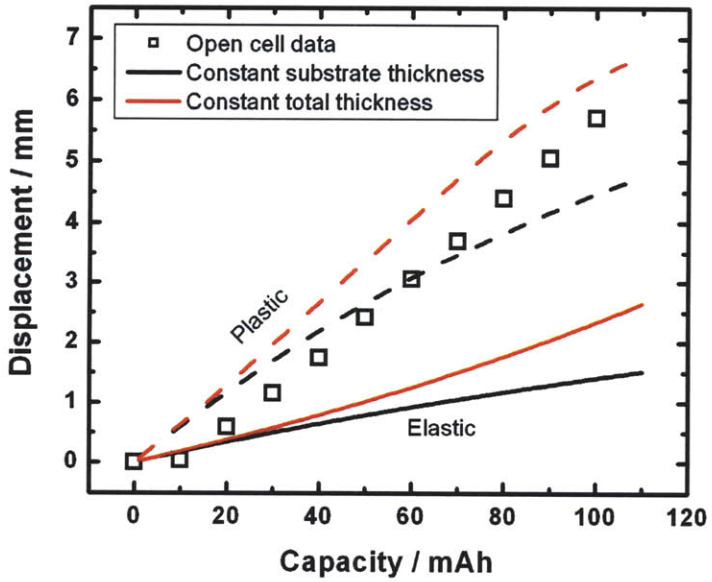


Figure 4-11. Open cell data and calculated displacements for a disc actuator. Models are based on effective elastic or plastic moduli and the assumptions of constant total

thickness or constant substrate thickness. The model using effective plastic moduli and assuming constant total thickness gives the best fit for the data.

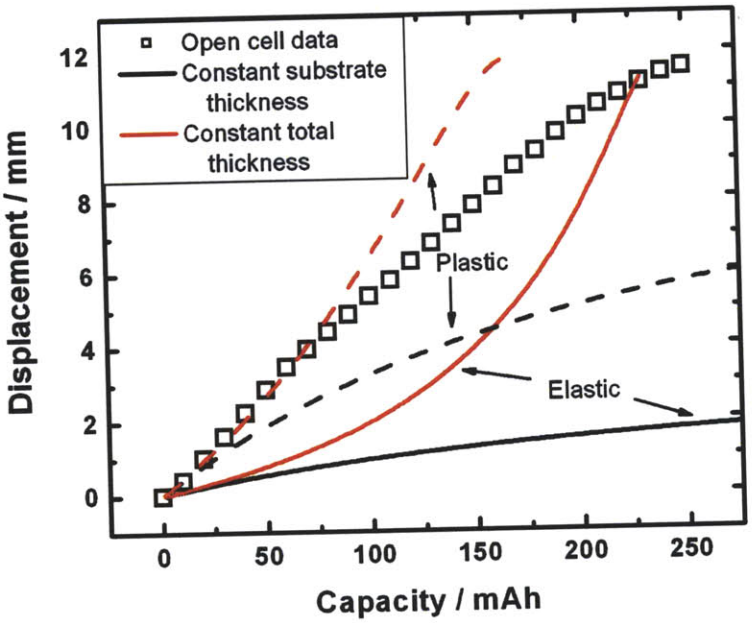


Figure 4-12. Open cell data and calculated displacements for a controlled folding, rectangular actuator. Models are based on effective elastic or plastic moduli and the assumptions of constant total thickness or constant substrate thickness. The model using effective plastic moduli and assuming constant total thickness gives the best fit for the data.

4.4 Bifurcation

One point of interest that can be calculated for a disc actuator is the critical curvature for bifurcation, κ_{bif}:

$$\kappa_{bif} = \frac{4}{\sqrt{1+\nu}} \frac{h_s}{a^2} \left(1 + \frac{h_f}{h_s}\right) \tag{4.8}$$

where a is the radius of the disc. For a ¾ in diameter, 1 mm thick disc, this is calculated to be 37.9 m^{-1} taking h_f/h_s to be small. This corresponds to a displacement of 1.7 mm

based on a circular profile. Up to the bifurcation point, spherical curvature yields a stable configuration so assuming a circular profile is valid.

This was verified using packaged actuator devices. For these tests, actuators were discharged through a fixed 10 ohm resistor for 24 hours at discrete mechanical loads applied by an Instron materials testing machine (Instron 5567). From the displacement versus capacity curves (Figure 4-13), the bifurcation point manifests itself where samples discharged at low mechanical loads start to fold and the displacement diverges from the curves suppressed from folding at higher mechanical loads. These devices are pictured in Figure 4-14. The bifurcation point is around 1.5 mm displacement, agreeing closely with the predicted value. It should be noted that the measured displacement value here is of the entire device and includes creep losses from the lithium and separator as well as thickness loss from the stripping of the lithium for the reaction. Therefore, it is expected that this measured value will be slightly less than the calculated number as the displacement of the aluminum itself should be greater than the measured displacement of the device.

Even at higher loads, the displacement still increases beyond the predicted critical bifurcation point. In these samples, the bifurcation exhibited itself in a different manner, taking a curvature discontinuity point near the center of the sample. Macroscopically, this appeared as a dimple in the center of the circular disc. The cross-section in Figure 4-15 shows concave downward curvature on the left and right sides of the disc, but a slight concave upward curvature near the center.

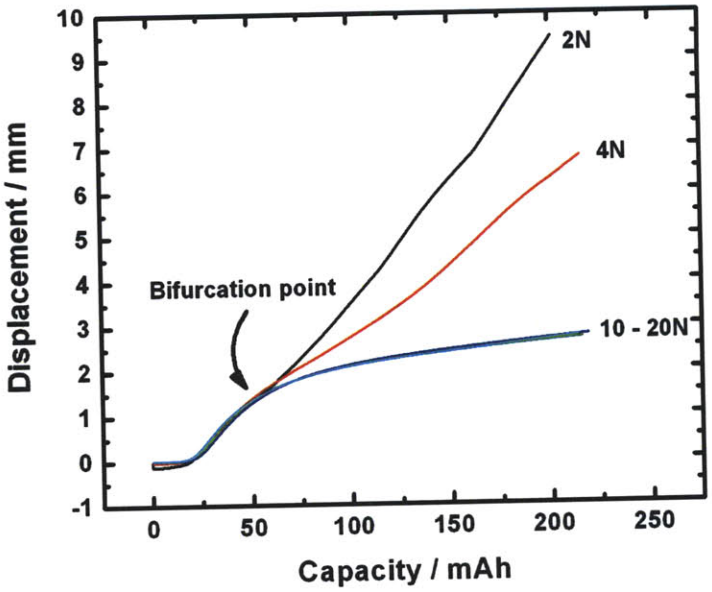


Figure 4-13. Displacement versus capacity actuation curves for packaged disc samples at discrete mechanical loads. The bifurcation point is indicated.



Figure 4-14. Representative deformation of an actuator suppressed from folding (left) and an actuator that has folded (right).



Figure 4-15. Cross section of an aluminum-based actuator suppressed from folding. The bifurcation manifests itself through a curvature discontinuity point near the center of the sample. The scale bar is 1 mm.

4.5 Summary

In this chapter, we have demonstrated an actuation mechanism based on electrochemical alloying of lithium with a host metal, in this case, aluminum. An out-of-plane bending is created through a bilayer structure with materials of significantly different molar volume with displacements up to 6 mm from a 1 mm thick disc at 100 mAh discharge. A controlled folding geometry provided displacement amplification and achieved almost 12 mm displacement in 250 mAh for a 1.5 mm thick sample. Virtually all of the deformation comes from plastic deformation. Displacement results have been modeled according to Stoney's equation and using effective plastic moduli even though deformation is beyond the linear regime. Further, the bifurcation point is well-predicted with the current model and two post-bifurcation shapes are observed depending on the external mechanical load – one with cylindrical deformation and one with a curvature discontinuity creating a dimple in the top of the sample.

4.6 References

1. Timoshenko, S. & Woinowsky-Krieger, S. *Theory of plates and shells*. (McGraw-Hill: New York, 1959).
2. Melendres, C. & Sy, C. Structure and cyclic discharge behavior of LiAl electrodes. *Journal of The Electrochemical Society* **125**, 727-731(1978).
3. Huang, T. & Brittain, J. Effect of defect structure upon the mechanical behavior of beta-LiAl through dislocation damping and hardness studies. *Metallurgical Transactions A* **13A**, 2173-2176(1982).
4. Freund, L. & Suresh, S. *Thin Film Materials: Stress, Defect Formation, and Surface Evolution*. (Cambridge University Press: New York, 2003).
5. Kuriyama, K., Saito, S. & Iwamura, K. Ultrasonic study on the elastic moduli of the NaTl (B32) structure. *J. Phys. Chem. Solids* **40**, 457-461(1979).
6. Howatson, A., Lund, P. & Todd, J. *Engineering Tables and Data, 2nd Edition*. 41(Chapman & Hall: New York, 1991).
7. Tabor, D. A simple theory of static and dynamic hardness. *Proceedings of the Royal Society of London, Series A* **192**, 247-274(1948).
8. Huang, T. & Brittain, J. The mechanical behavior of beta-LiAl. *Materials Science and Engineering* **93**, 93-97(1987).

5 Actuation Devices Based on Electrochemical Alloying

While open cell testing provides insight on the capability of the active actuation element, it is necessary to assemble a useful device that can be used outside of the inert atmosphere of the glove box for any practical use. This was achieved by sealing the components in a metal polymer laminate packaging with the copper current collectors protruding out, making a pouch cell (Figure 5-1, left). While the actuation mechanism remains the same, the packaging tends to force the lithium to remain conformal to the surface of the active actuation electrode during deformation and adds additional stiffness which the active electrode must work against. The deformation regimes are the same as discussed in Chapter 4 and are shown in Figure 5-1. In the non-linear deformation regime, the sample takes a 'bottlecapped' shape with significantly increased curvature near the edges relative to the center, shown in the middle sample in the figure. Bifurcation leads to the sample appearing to 'fold', as seen in the sample on the right. In this chapter, we discuss the actuation behavior and properties of these devices and different control mechanisms.



Figure 5-1. Packaged aluminum-based actuators in different deformation states. From left to right, an as assembled actuator, an actuator discharged into the non-linear deformation regime, and a bifurcated actuator.

5.1 Materials Selection

In the open cell test setup, we focused on using aluminum as the active actuation element, however, many metals form intermetallics with lithium. In nearly all cases, the intermetallic has a larger molar volume than the pure host metal. As such, this particular actuation mechanism can be applied over a range of materials. Figure 5-2 shows the molar volume ratio of an intermetallic to the pure host metal as a function of lithium content. Aluminum has the highest partial molar volume with respect to lithium of the materials listed. Tin, on the other hand, has one of the lowest, making for an interesting comparison. These metals were also chosen for the active actuation element due to their electrochemical stability with the given electrolyte as well as their non-toxicity.

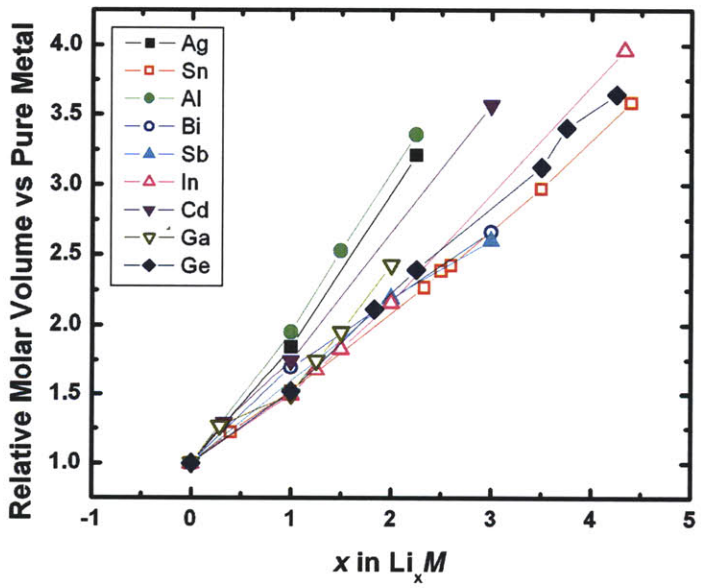


Figure 5-2. Plot of molar volume per host metal relative to the molar volume of the pure host metal versus lithium content. Many metals show an increased molar volume with added lithium. Aluminum has a high partial molar volume while tin has a low partial molar volume with respect to lithium.

Lithium metal was used for the counterelectrode to provide the lithium source. It is also soft[1] and easily conforms during deformation of the device. Electrochemically, an advantage of using lithium metal as the counterelectrode is that the device can be self-powered. For example, the activity, a, of lithium in LiAl is less than for the pure metal taken at a standard state (unit activity).[2] The Nernst equation (Equation 1.3):

$$E = E^0 + \frac{RT}{nF} \ln \frac{a_O}{a_R} \tag{5.1}$$

where E is the electric potential, E^0 is the standard potential of the reaction, R is the universal gas constant, T is the temperature, z is the number of electrons involved in the reaction, F is the Faraday constant, a_O is the activity of oxidation species, and a_R is the activity of the reduction species, relates the activity of the active species to the electric potential. For Li + Al → LiAl, LiAl is the reduction species and the Nernst equation indicates LiAl will have a positive electric potential with respect to pure lithium. In fact, many pure metals and their associated lithium intermetallics have positive electric potentials relative to pure lithium.[3-5] This means that upon assembly, a lithium/electrolyte/*M* cell is initially in a charged state. The Li-*M* intermetallic can be formed simply by short-circuiting the cell. Since this alloying is also the mechanical actuation mechanism, these cells can be self-powered: as electrical energy is dissipated, mechanical energy can be extracted spontaneously and simultaneously. Naturally, the cell can also be driven by conventional electrochemical protocols.

The self-amplified mechanism described in Chapter 4 is necessitated by the use of lithium metal though. Due to its high molar volume (12.99 $cm^3\ mol^{-1}$), the stripping of lithium metal results in a volume loss that is typically greater than the expansion gained through alloying. For example, the reaction Li + Al → LiAl actually results in a net

volume change of -15.1%. Theoretically, utilizing the volume change directly would lead an overall contraction of the cell. Further, large void formation has been observed in monolithic electrodes upon full lithiation which could lead necking and eventually to isolation of parts of the electrode. Therefore, it is more reliable to use the self-amplified mechanism.

5.1.1 Lithium-Aluminum System

Lithium forms three equilibrium intermetallic phases with aluminum: LiAl, Li_3Al_2, and Li_9Al_4. The phase diagram is shown in Figure 5-3. Their potentials upon first formation versus lithium and volume versus pure aluminum are shown in Table 5-1.[6,7] The initial discharge reaction in a Li/Al cell is Li + Al → LiAl and has an equilibrium potential of 0.370 V. While higher lithium intermetallic stoichiometries exist, the facile kinetics of this initial reaction prevent their formation until full conversion of the aluminum electrode to LiAl. Our utilization of a self-amplifying, unimorph design requires limiting the reaction to a fraction of the total thickness of the aluminum.

The crystal structure of aluminum is FCC while the crystal structure of LiAl is NaTl. The NaTl structure consists of two interpenetrating diamond lattices, one shifted by ½ along one principal axis (Figure 5-4). During lithiation, the aluminum atoms must undergo significant restructuring to accommodate this phase change, leading to irreversible mechanical behavior.

Table 5-1. Potential and change in volume with respect to pure aluminum for the lithium-aluminum intermetallic compounds.

Compound	V vs Li/Li+	Molar volume vs Al
LiAl	0.370	195%
Li_3Al_2	0.150	253%
Li_9Al_4	0.050	336%

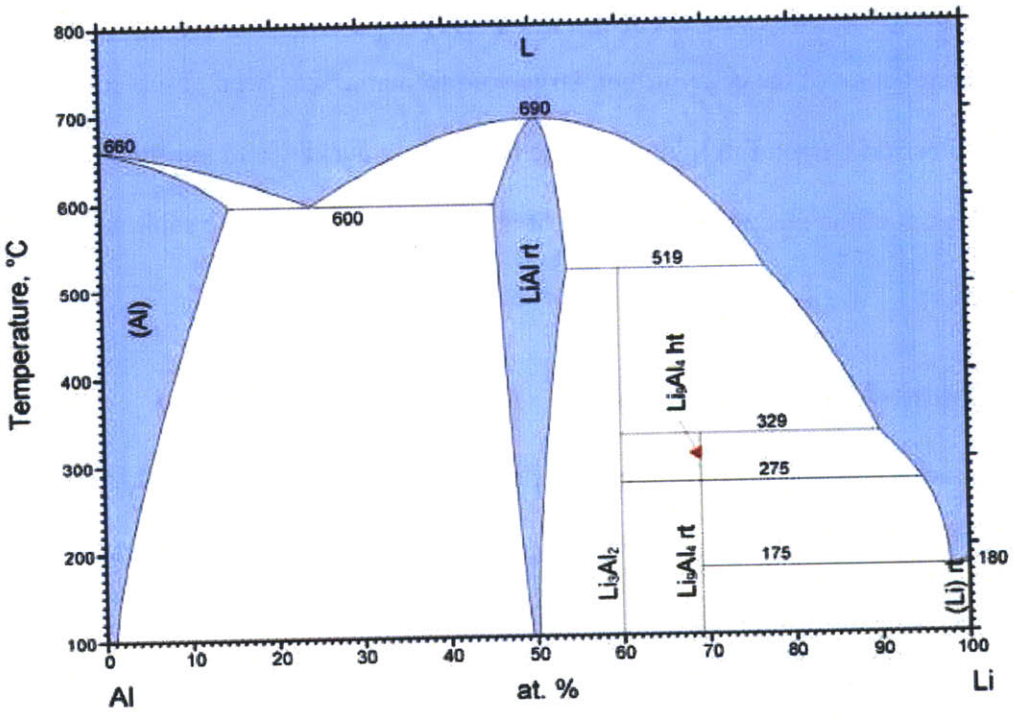


Figure 5-3. Phase diagram for the lithium - aluminum system.[8] Only three equilibrium intermetallics form between Li and Al.

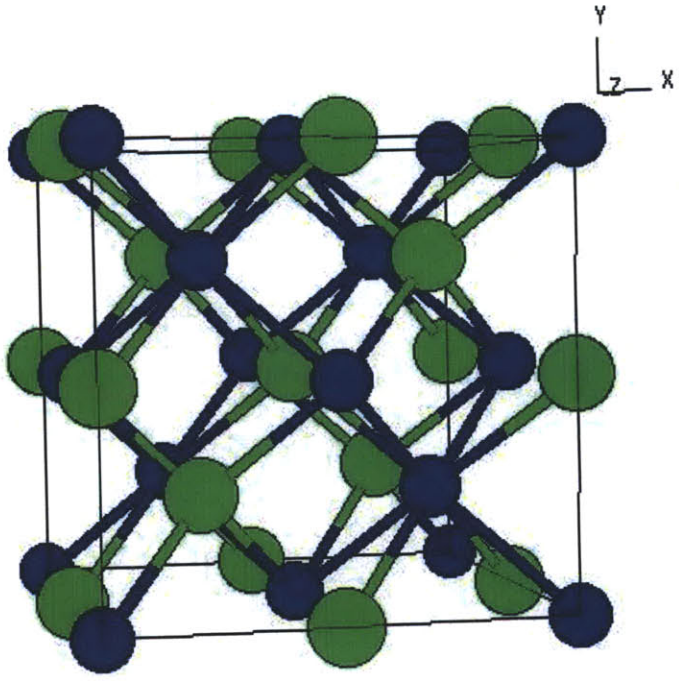


Figure 5-4. The NaTl crystal structure of LiAl. The structure consists of two interpenetrating diamond lattices.[9]

5.1.2 Lithium-Tin System

The lithium-tin system shows seven equilibrium intermetallic stoichiometries. The phase diagram is shown in Figure 5-5. Their potentials upon first formation versus lithium and volume versus pure tin are shown in Table 5-2.[10]

Table 5-2. Potential and volume change with respect to pure tin for the lithium-tin intermetallics.

Compound	V vs Li/Li+	Molar volume vs Sn
Li_2Sn_5	0.760	122%
LiSn	0.660	152%
Li_7Sn_3	0.530	227%
Li_5Sn_2	0.485	239%
$Li_{13}Sn_5$	0.485	243%
Li_7Sn_2	0.420	297%
$Li_{22}Sn_5$	0.380	359%

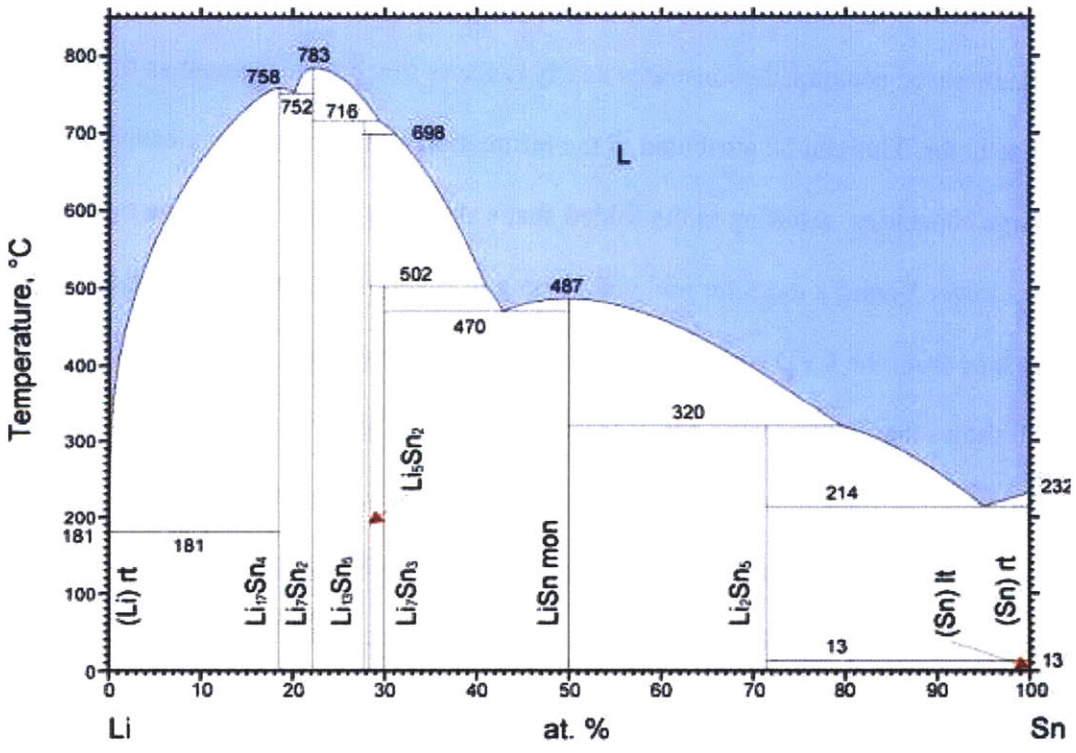


Figure 5-5. Phase diagram for the lithium - tin system.[11] Seven Li – Sn intermetallics can form equilibrium phases.

5.2 Results and Discussion

5.2.1 Self-powered Actuation – Aluminum Versus Tin

In this set of experiments, ¾ in diameter, 1 mm thick discs of aluminum and tin were assembled into separate pouch cells with a 24 mm diameter Whatman separator and a counterelectrode of lithium metal. Both types of working electrodes and the lithium metal electrode were spot welded to a copper current collector. Aluminum-based actuators were vacuum-sealed in a metal laminate packaging while tin-based actuators were vacuum-sealed in a polyethylene-based packaging. Both were then discharged through a fixed 10 ohm resistor for 10 hours.

Representative self-powered actuation results for both lithium-aluminum and lithium-tin actuators are shown in Figure 5-6, along with their discharge current profiles. The aluminum-based actuator demonstrates nearly twice as much displacement as the tin-based actuator. This can be attributed to the bifurcation of aluminum at extensive discharge capacities, resulting in the folded shape shown in Figure 5-1 on the right. Tin, with its lower Young's modulus and yield strength, is suppressed from folding due to the spring load from the LVDT measuring the displacement. Separate testing without an LVDT shows that the tin-based actuator will also fold at lighter loads which would give similarly high displacements. The critical curvature for bifurcation should be similar for both materials as the only material property in Equation 4.8 is Poisson's ratio, which doesn't significantly vary between metals, and the displacement at bifurcation should be 1.7 mm. Tin-based actuators displaced against the LVDT showed the higher-order bifurcation exhibited by aluminum-based actuators displaced against higher loads (Figure 4-15).

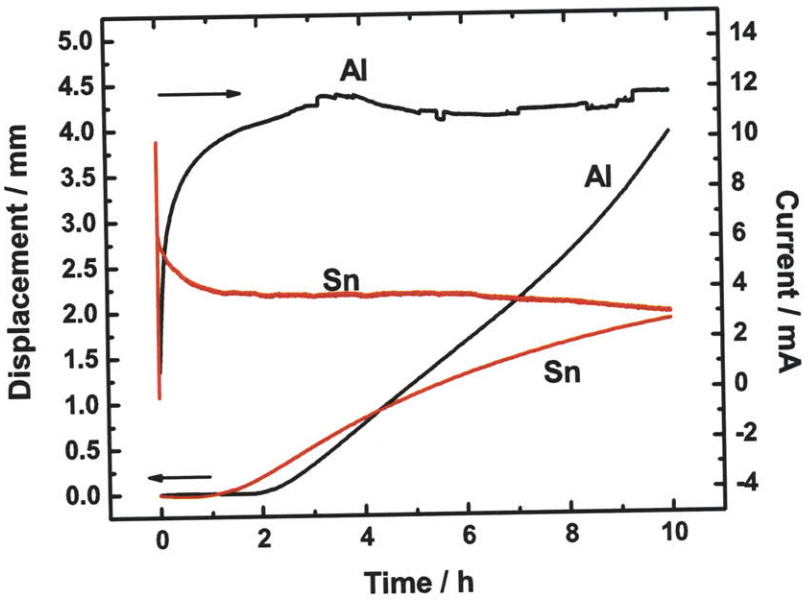


Figure 5-6. Displacement and current curves for aluminum- and tin-based actuators undergoing discharge through a fixed 10 ohm resistor.

The displacement rate *dy/dt* of the aluminum-based actuator is also greater than for the tin-based actuator. While the mechanical property differences may bear some effect, it is also necessary to consider the rate at which these samples are discharging. The current versus time electrochemical response when going through a self-powered discharge is nearly opposite for these two systems (Figure 5-6). For the aluminum cell, the current starts near zero, gradually increases, and plateaus around 11 mA. For the tin cell, the current starts high, peaking around 10 mA and then decays with time as the intermetallic film grows.

These electrochemical differences can be explained by the cell impedance. As assembled, both have low frequency impedances in the range of 10^5 ohms, likely owing to surface

oxide layers. This impedance for the lithium-tin system drops quickly to around 40 ohms initially upon discharge, but quickly grows to greater than 100 ohms with continuing discharge (Figure 5-7b), causing the current to decay and decreasing the overall rate of discharge capacity. The impedance evolution of the tin electrode with discharge capacity is consistent with literature results.[12] The increase in charge transfer resistance is attributed to a growing solid-electrolyte interphase (SEI) layer on the surface of the tin, particularly pronounced at low discharge currents.[12]

For the lithium-aluminum system, the low frequency impedance decreases quickly with discharge capacity, settling around 30 ohms (Figure 5-7a) as a complete intermetallic film forms on the surface of the electrode[13] reducing the aluminum/electrolyte interfacial area. The impedance grows slowly as the film continues to thicken, but does not increase by more than a factor of two. The LiAl doesn't show significant SEI formation,[14] maintaining a relatively low impedance. Therefore, the discharge capacity increases faster in the aluminum actuator, which leads to tin displaying a greater displacement per capacity dy/dQ as seen initially in Figure 5-8. Again, the depression of displacement of tin-based actuators at greater capacities is due to the suppression of folding caused by the LVDT.

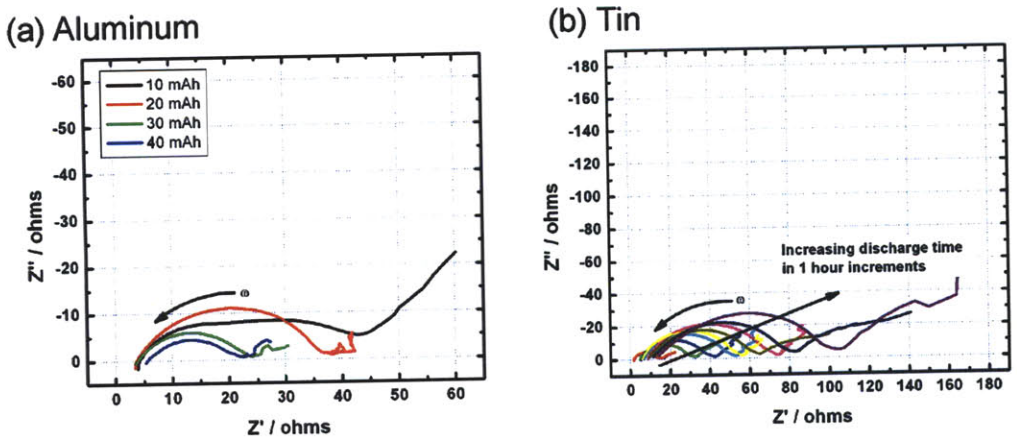


Figure 5-7. Nyquist plots taken between 0.01 Hz and 1 MHz for (a) aluminum- and (b) tin-based actuators at various states of discharge. The charge transfer resistance for the aluminum electrode decreases as LiAl is formed initially. For the tin electrode, the impedance grows quickly with increasing discharge capacity.

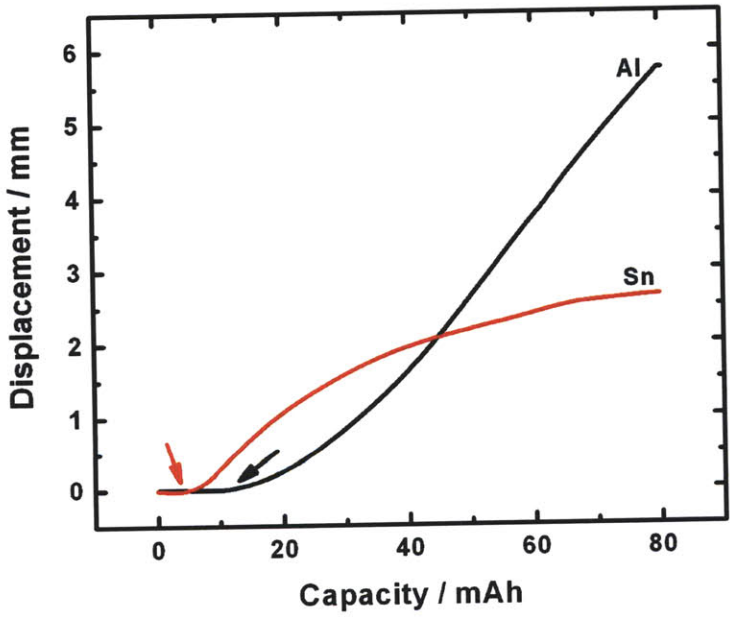


Figure 5-8. Displacement versus capacity curves for aluminum- and tin-based actuators. Tin shows an initially greater displacement per capacity which is later suppressed by the force of the LVDT. The arrows indicate the incubation capacity – the minimum capacity needed before measurable deformation.

This is the opposite of what is expected from the partial molar volumes shown earlier, where aluminum has a greater lithium partial molar volume versus tin, 1.05 cm^3 $(mol\ Al)^{-1}$ $(mol\ Li)^{-1}$ to 0.58 cm^3 $(mol\ Sn)^{-1}$ $(mol\ Li)^{-1}$, respectively. However, as we saw for the aluminum, this volume expansion is anisotropic, manifesting itself primarily in the thickness direction so the partial molar molumes shouldn't have a significant effect on the bending. However, the material properties play a significant role in the deformation of these samples. From Stoney's equation (Equation 4.4), the curvature is dependent on the effective moduli ratio of the film to the substrate. Inferring these values from the Vickers hardness as was done in Chapter 4, the moduli ratio for tin is 2.64 ($\sigma_{y,Sn}$ = 38.5 MPa and $\sigma_{y,Li\text{-}Sn}$ = 103 MPa) and for aluminum it is 2.21. This will give tin an increased curvature and, therefore, greater displacement, for a given film thickness. Applying the constant total thickness, plastic deformation model, the calculated displacements are shown in Figure 5-9. Tin has a greater displacement per capacity as initially observed in the experimental measurements. These models do not account for packaging restrictions or external forces, so the absolute displacements are significantly greater than the measured displacements. The depression in measured displacement per capacity in the tin-based actuator at larger is due to the increase in external force applied by the spring-loaded LVDT suppressing the folding mode of bifurcation.

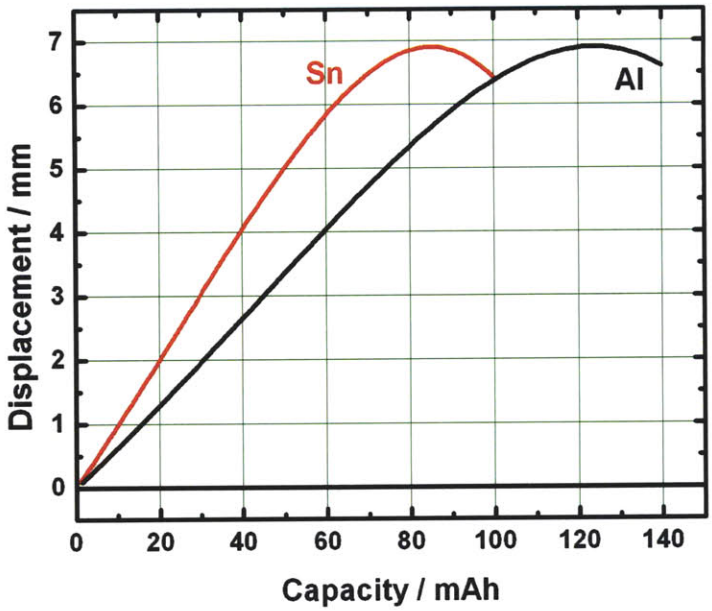


Figure 5-9. Calculated displacement versus capacity models for tin- and aluminum-based actuators from the constant total thickness, plastic model presented in Chapter 4, using the same mismatch strain for both systems. Tin displays a greater displacement per capacity due to greater ratio of yield strength of the film versus substrate.

Common to both curves is an initial period of zero displacement even though capacity is increasing. This 'incubation' is related to the time needed for a sufficient intermetallic film to nucleate and coalesce in order to provide enough stress to induce bending, overcoming the bending stiffness, D, of the substrate (based on Equation 4.3, corrected for spherical bending):

$$D = \frac{Eh^3}{12(1-\nu)} \tag{5.2}$$

Here, we can use the elastic modulus since the displacements under consideration are much less than the substrate thickness. The Young's modulus for aluminum is 70 GPa whereas for tin it is only 47 GPa.[15] Assuming similar Poisson's ratios for aluminum and

tin, aluminum has a bending stiffness 1.49 greater than tin. The incubation on a capacity basis for aluminum is greater than for that of tin, 12 mAh versus 5 mAh, or 2.4 times greater. However, this does not account for other sources of stiffness such as the packaging, other cell components, and the external LVDT or the actual film thicknesses. The tin-based actuator was packaged in a non-metallized polyethylene-based packaging that is less stiff than the metallized packaging used for the aluminum-based actuator. This would decrease the overall stiffness of the tin-based actuator relative to the aluminum-based one, helping to explain the discrepancy between the incubation capacity ratios and the bending stiffness ratios.

5.2.2 Galvanostatically Discharged Aluminum Actuators

This section discusses aluminum-based actuators of the same construction described in Section 5.2.1. This set of actuators was discharged galvanostatically (constant current) up to 100 mAh capacity at various fixed currents between 0.5 mA and 10 mA.

The displacements versus capacity for the galvanostatically discharged samples are shown in Figure 5-10 with two different samples plotted for most currents. Throughout the capacity range, the samples discharged at 2 mA or less show decreased displacement compared to samples discharged at 4 mA or more. At 100 mAh, the displacements for samples discharged at 2 mA or less end up between 2.5 – 3.0 mm, slightly less than the typical 3.25 – 3.75 mm for samples discharged at 4 mA or higher. The cross-sections of some of these samples after discharge and after removal from the packaging are shown in Figure 5-11. The lighter strip is the aluminum and the darker

coating on the top surface is the LiAl intermetallic. Increased curvature is observed at currents of 4 mA or higher, further confirming the increased displacement. The self-powered sample shown above (Figure 5-6) maintains a current around 11 mA for a majority of the discharge and also has a displacement in the upper range. This implies there is a larger bending stress at higher film growth rates leading to the increased curvature and greater displacements. This is unaccounted for in the analytical model presented in the previous chapter.

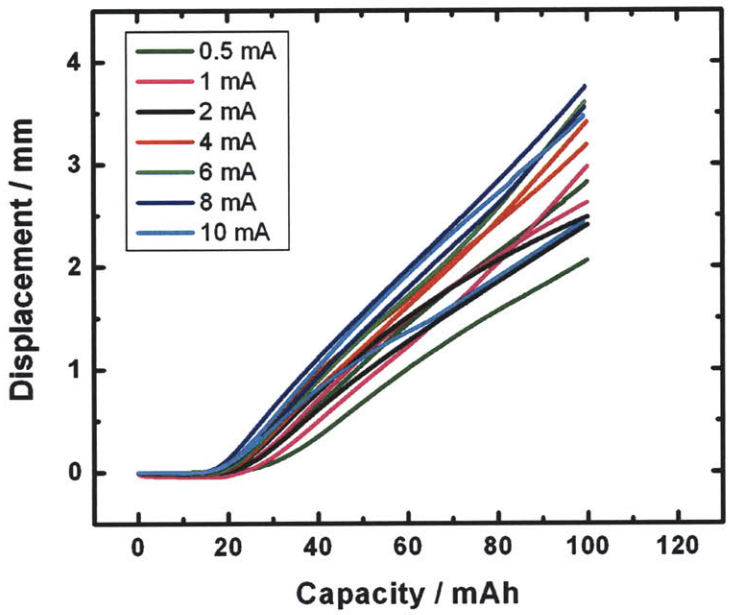


Figure 5-10. Displacement versus capacity curves for aluminum-based actuators discharged galvanostatically between 0.5 and 10 mA. Greater displacements are observed at 4 mA and greater.

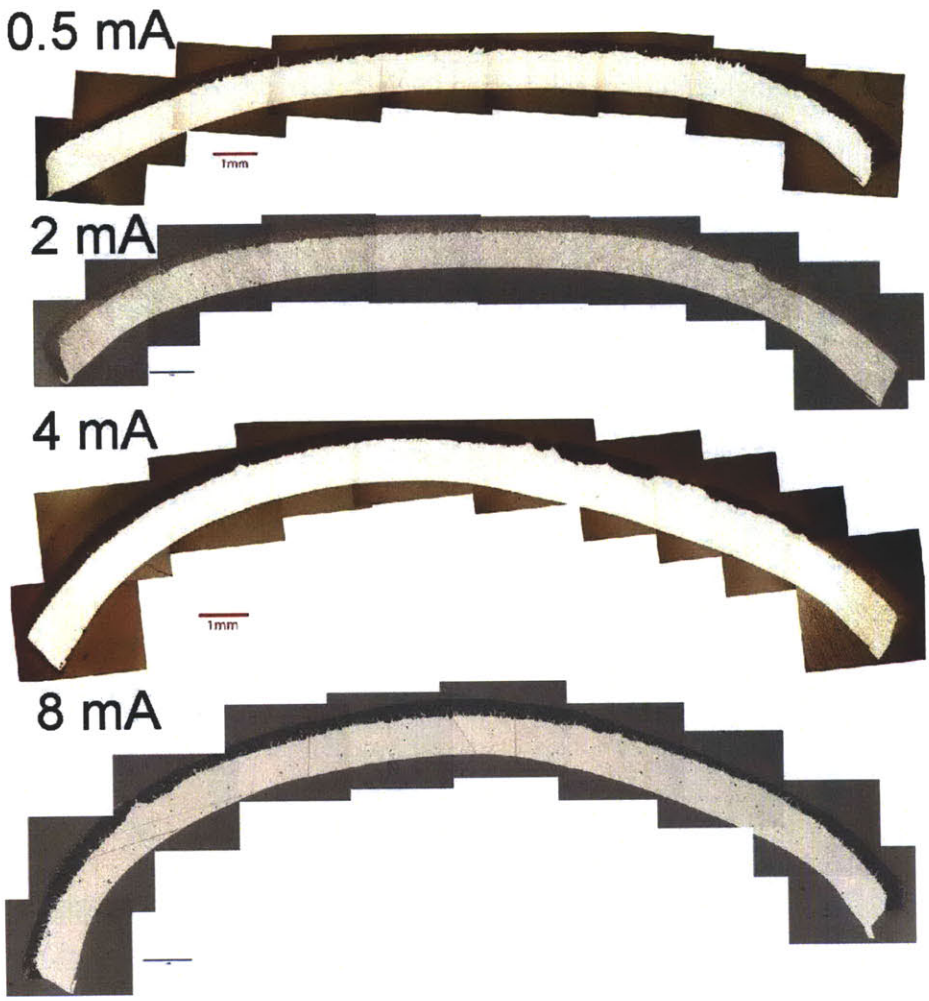


Figure 5-11. Cross sections of galvonstatically discharged samples at 0.5, 2, 4, and 8 mA after removal from the packaging. All samples were discharged to 100 mAh. The scale bar for each picture is 1 mm. Increased curvature is seen at higher currents.

Electrochemical impedance measurements also indicate a progressive change at the electrolyte/LiAl interface at higher currents (Figure 5-12). These impedance measurements were measured after allowing the cells to relax after discharge. It is clear that at higher currents, there is a reduced charge transfer resistance, R_{ct}, interpreted from the diameter of the high frequency depressed semicircle. This is related to the exchange current density, i_0, by:

$$R_{ct} = \frac{RT}{AFi_0} \tag{5.3}$$

where R is the universal gas constant, T is the temperature, A is the reaction area, and F is the Faraday constant. The exchange current density is the current in the absence of net electrolysis and at zero overpotential. A decrease in the charge transfer resistance can be attributed to either an increase in the reaction area or an increase in the exchange current density. The exchange current density can also be expressed as:

$$i_0 = Fk^0 c_{Li^+}^{(1-\alpha)} c_{Li}^{\alpha} \tag{5.4}$$

where k^0 is the reaction rate constant, $c_{\mathrm{Li}}{}^{+}$ is the concentration of lithium ions in the electrolyte, c_{Li} is the concentration of lithium in LiAl, and α is the transfer coefficient. An increased concentration of lithium at the surface of the LiAl would increase the exchange current density. The LiAl phase is not a line compound but has a stoichiometry range between $x = 0.85 - 1.17$ in $\mathrm{Li_xAl}$ (atomic percentages of 0.46 – 0.54). This does not account for the factor of four increase in the exchange current density. It is more likely that an increase in the reaction area allows for a reduced charge transfer resistance. Microstructural analysis (discussed below) reveals more cracking of the intermetallic film at higher discharge currents, which would increase the reaction area.

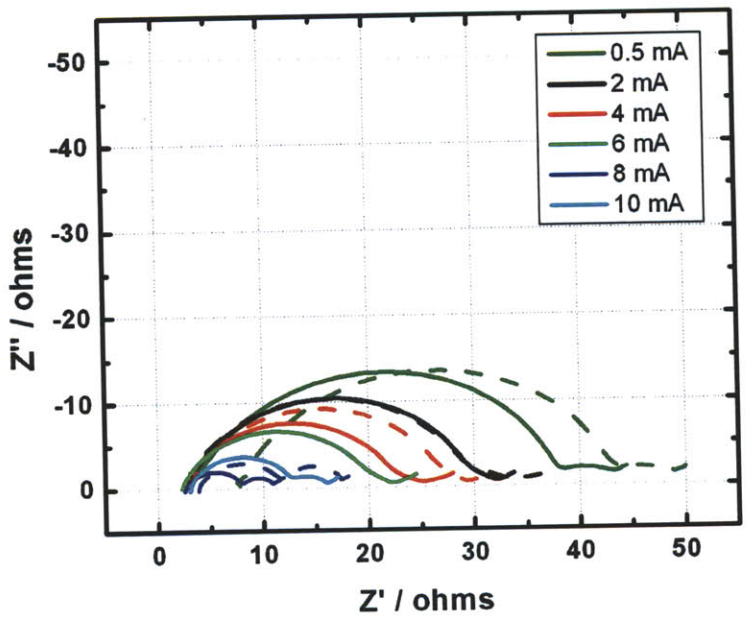


Figure 5-12. Nyquist plots for aluminum-based actuators discharged galvanostatically to 100 mAh. Dashed lines indicate a separate sample. The charge transfer resistance is seen to decrease at higher currents.

A closer look at the intermetallic film reveals a columnar growth morphology (Figure 5-13 and Figure 5-14), similar to what has been observed in literature.[17] From here, we can define feature sizes by 'heights' and 'widths' which are measured parallel and perpendicular to the growth direction, respectively. The feature heights are bounded by cracks and boundaries perpendicular to the growth direction which are signs of stress relief within the film layer. The feature widths are bounded by cracks and boundaries parallel to the growth direction and are indicative of the nucleation and coalescence of the intermetallic phase. The feature heights at discharge currents of 2 mA or below are greater than 40 μm, larger than the feature heights at discharge currents of 4 mA or greater which are less than 35 μm, indicating that there is an increased amount of stress

built up in the film at higher currents, consistent with the curvature and displacement data. The feature widths remain fairly constant around 25 um (Figure 5-15). At higher currents, the nucleation rate of LiAl on the surface of the aluminum should be greater, but this appears to have little effect on the feature widths. Therefore, it is more likely influenced by the microstructure of the aluminum. It has been observed that there is preferential lithium diffusion in the grain boundaries of the aluminum[18] which would fix these feature widths independent of current.

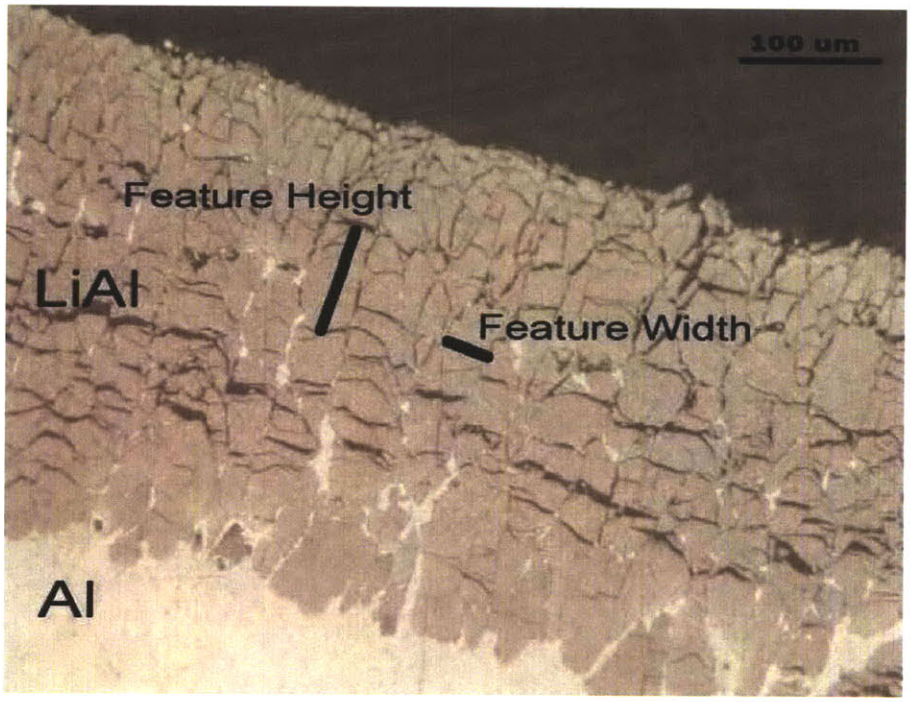


Figure 5-13. Image illustrating the columnar morphology of the LiAl intermetallic film. Feature heights and widths are defined by their orientation to the LiAl/Al interface. This was for an actuator galvanostatically discharged at 10 mA to 100 mAh.

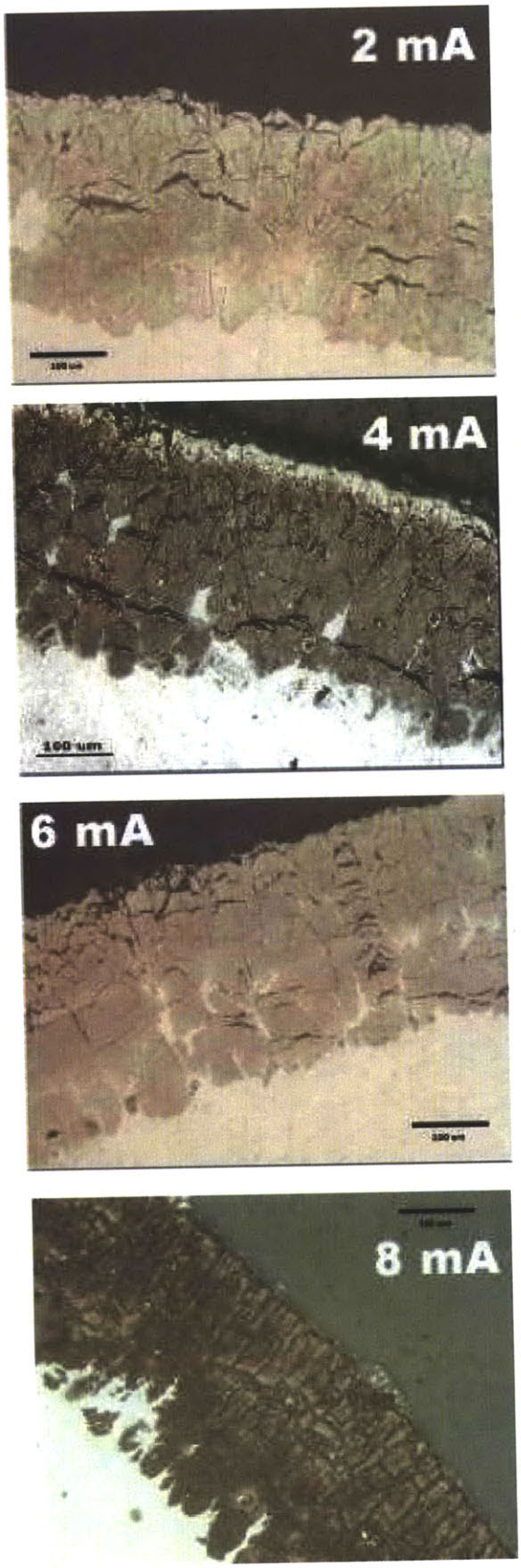

2 mA
4 mA
100 um
6 mA
8 mA

Figure 5-14. (Previous page) Optical micrographs from separate samples of the microstructure of intermetallic films from aluminum-based actuators for samples discharged at 2, 4, 6, and 8 mA to 100 mAh.

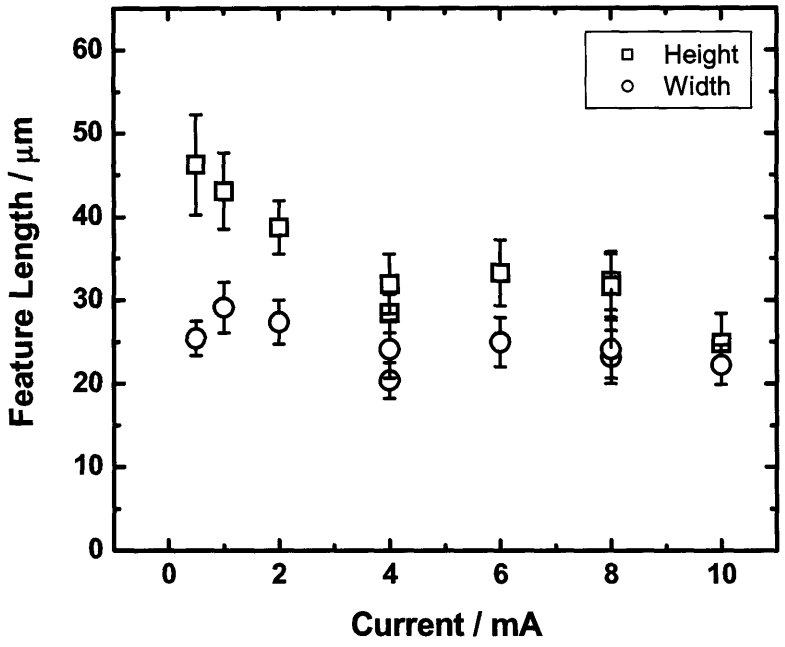


Figure 5-15. Feature heights and widths for samples discharged galvanostatically to 100 mAh. Feature heights decrease with increasing current while feature widths do not significantly vary.

5.2.3 Self-powered Aluminum Electrochemistry, Morphology, and Microstructure

In this section, similar actuators were constructed as in the previous two sections. These samples were actuated through self-powered discharge through a fixed 10 ohm resistor for a prescribed time of 2, 4, 6, 8, or 10 hours. The displacements were measured using the spring-loaded LVDT.

The displacement and current curves for these samples are plotted in Figure 5-16 versus capacity. All of the currents plateau between 11 – 13 mA after 20 mAh.

Correspondingly, the displacement curves are mostly similar. The current response, I, can be explained through the Butler-Volmer equation shown in Equation 5.5 which predicts the overpotential-current relationship of an electrode.

$$I = Ai_0 \left\{ \exp\left[\frac{(1-\alpha)nF}{RT} \eta \right] - \exp\left[-\frac{\alpha nF}{RT} \eta \right] \right\} \tag{5.5}$$

Here, I is the current, A is the electrode area, i_0 is the exchange current density, F is the Faraday constant, R is the universal gas constant, T is temperature, n is the number of electrons involved in the reaction, and η is the overpotential ($E - E_{eq}$). The first exponential term in the braces represents the contribution from the anodic reaction while the second exponential term represents the cathodic contribution, as both the forward and backward reactions are occurring simultaneously. At high enough overpotentials, one term will dominate over the other.

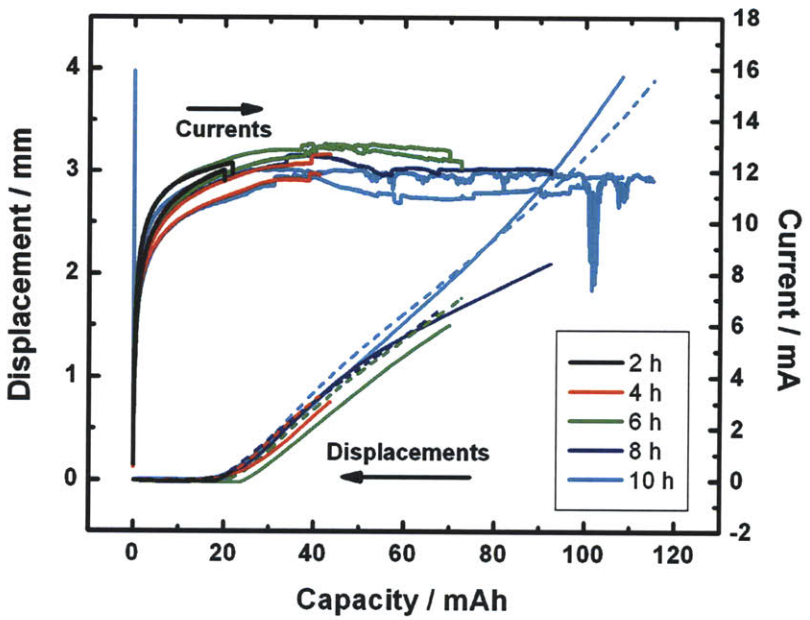


Figure 5-16. Displacement and current curves versus capacity for aluminum-based actuators discharged through a fixed 10 ohm resistor for 2, 4, 6, 8, or 10 hours. The displacements are reasonably reproducible in the overlapping time periods while the current is between 11 – 13 mA for a majority of the discharge.

The charge transfer resistance was measured using electrochemical impedance spectroscopy. Figure 5-17 shows the Nyquist plots on a complex impedance plane for most of these samples. The solid and dashed lines indicate separate samples. The charge transfer resistance is between 15 – 25 ohms, measured as the diameter of the high frequency depressed semicircle. This corresponds to an exchange current density of 0.35 – 0.60 mA cm^{-2} from Equation 5.3. This is extremely dependent on the composition and concentration of the electrolyte[18] and has been measured for 1 M $LiClO_4$ to be 15 – 17 mA cm^{-2} in propylene carbonate (PC) or 3 mA cm^{-2} in dioxalane[6,17] and for 1 M LiBr in PC around 5 mA cm^{-2}.[18] The low exchange current density measured for the actuation devices are likely due to the low activity of Li in $LiPF_6$[19] compared to LiBr.[18,20]

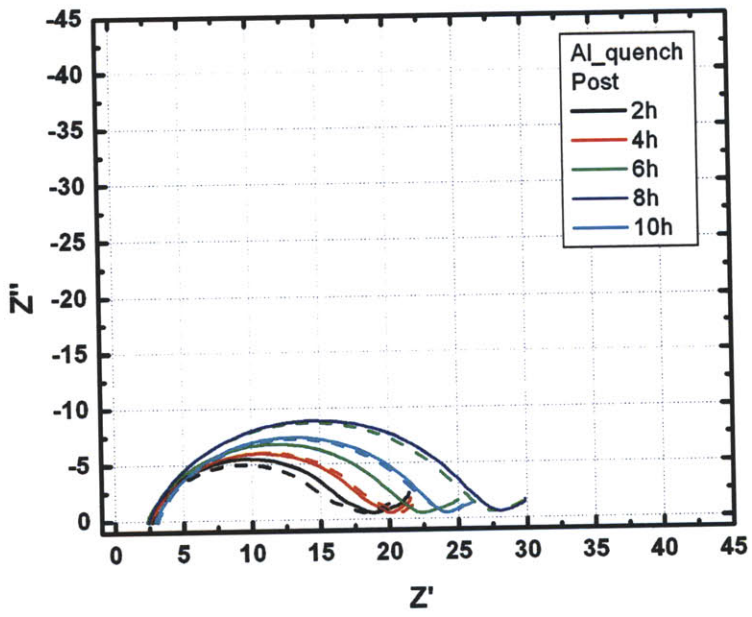


Figure 5-17. Nyquist impedance plots for aluminum-based actuators discharged through a fixed 10 ohm resistor for 2, 4, 6, 8, and 10 hours. The discharge capacities for these samples are greater than for those shown in Figure 5-7 and show increasing impedance with increasing discharge.

The transfer coefficient was taken to be 0.5. This is in line with the measured values for 1 M $LiClO_4$ electrolyte.[6,17] Transfer coefficients typically range from 0.3 – 0.7 and can be approximated by 0.5 in the absence of actual measurements.[21]

In order to measure the overpotential at the aluminum electrode, a sample with a lithium metal reference electrode was constructed, shown schematically in Figure 5-18. These samples were discharged through a 10 ohm resistor in one hour intervals with one hour rest periods in between. The voltages between each pair of electrodes for two separate samples are shown in Figure 5-19. The overpotential can be taken as the difference between the working potential of the aluminum relative to the reference electrode during discharge versus the equilibrium cell voltage during the open circuit rest

periods, as indicated by the green arrows in the figure. The overpotential ranges between -0.12 to -0.15 V for the first few discharge intervals before the deformation causes the voltage readings to go awry.

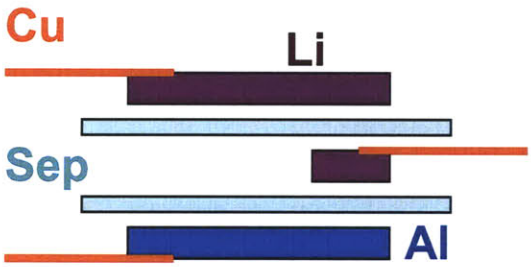


Figure 5-18. Schematic of a three electrode cell showing placement of a lithium metal 'flag' reference electrode in between the aluminum working electrode and lithium metal reference electrode.

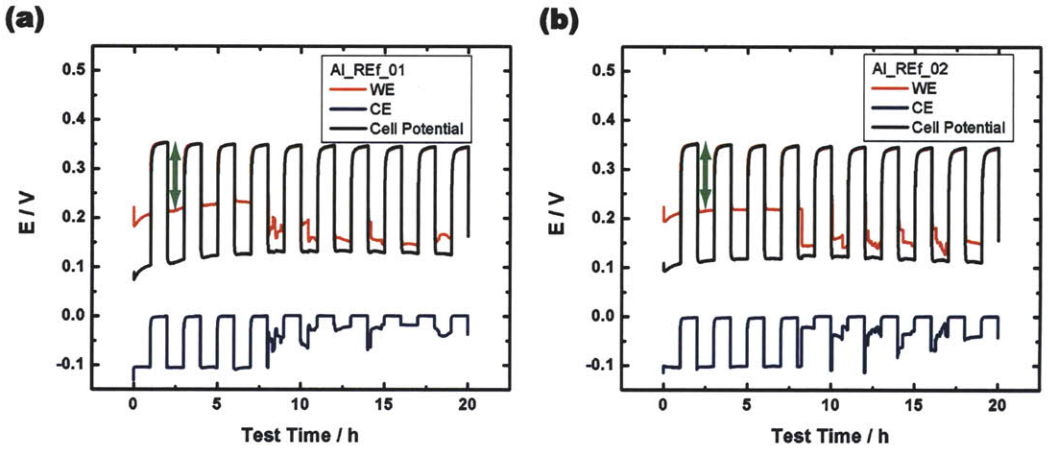


Figure 5-19. The potential of the aluminum working electrode and lithium metal counter electrode versus a lithium metal reference electrode and the overall cell voltage for two separate actuators. The overpotential at the aluminum electrode is indicated by the green arrows.

For the range of exchange current densities (0.35 to 0.60 mA cm^{-2}) and overpotentials (-0.12 to -0.15 V), the range of expected currents is -10 to -31 mA from Equation 5.4. The negative value merely indicates the discharge process due to the negative overpotential, and we will refer to absolute current values in this discussion. The

measured currents (typically 11 – 13 mA) lie within the lower end of this range. The overpotential starts high at the beginning of discharge. This is also where the exchange current density is at its lowest due to the high charge transfer resistance and presence of an aluminum/electrolyte interface. Therefore, the current should never approach the high end of the current range calculated with the largest values of the overpotential and exchange current density. Further, the exchange current densities are likely overpredicted as the reaction area increases due to cracking in the intermetallic film. Correcting for this would shift the calculated currents to lower values, but would still agree with the measured values.

The curvature evolution of the self-powered aluminum-based actuators can be seen from the series of cross-sections shown in Figure 5-20, taken from separate samples discharged for two, four, six, or eight hours. After two hours, there is a very thin intermetallic film across the whole surface of the disc, but there is virtually no bending. At longer discharge times, the film thickness continues to grow and the curvature increases, providing the large displacements. Some of the cross-sections show small unreacted areas on the aluminum surface (circled in Figure 5-20) which we attribute to gas bubbles in the electrolyte and non-wetting of the surface. This does not have a significant impact on the overall deformation of the discs.

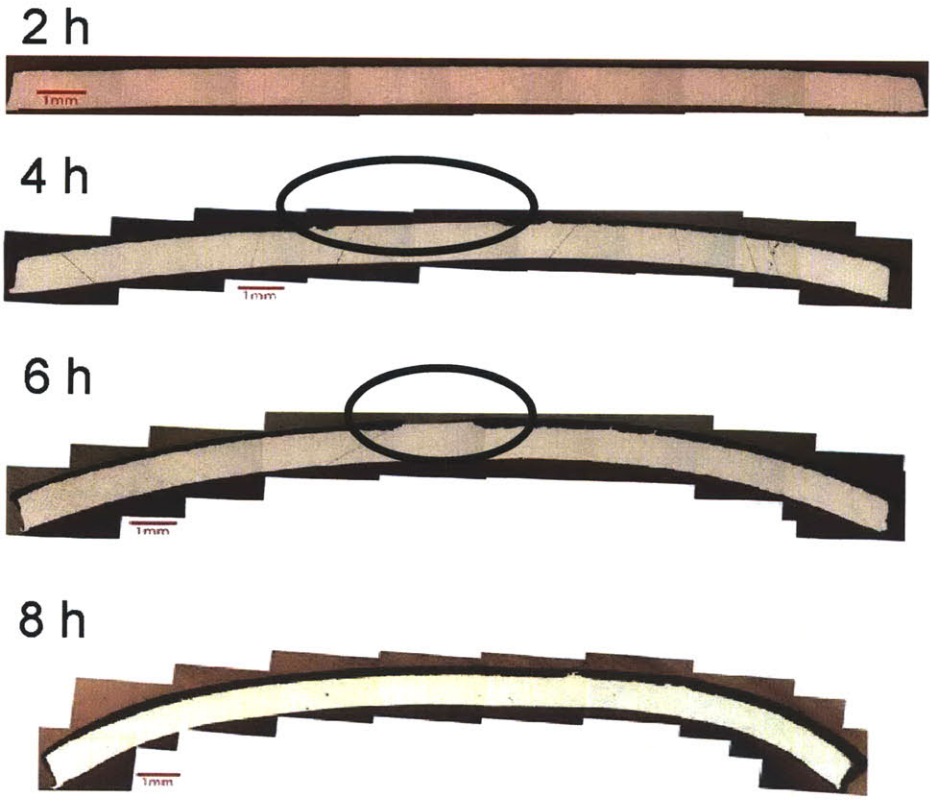


Figure 5-20. Cross sections of aluminum-based actuators discharged through a fixed 10 ohm resistor for the indicated time illustrating the evolution of the intermetallic film thickness and overall curvature during discharge. Scale bars are 1 mm. Unreacted areas are circled.

The average thickness of the intermetallic films grows linearly with discharge capacity (Figure 5-21). The data include these samples, galvanostatic samples (the data at 100 mAh), as well as other self-powered samples that were discharged for 24 h (see next section). The linearity indicates that over this range, the film maintains a single phase. Combined with calculations of the theoretical thickness for the known intermetallic phases, it is clear that only the LiAl phase is forming. These calculations were done based on the original reaction area of the sample as discussed in Chapter 4. The formation of LiAl is further confirmed by x-ray diffraction analysis on samples discharged for four

and 10 hours (Figure 5-22). In both of these samples, only aluminum and LiAl peaks are detected. There are no indications of lithium intermetallics of higher stoichiometry. The aluminum peaks likely come from the penetration depth of the x-rays, which is why they are more prominent in the sample discharged for four hours.

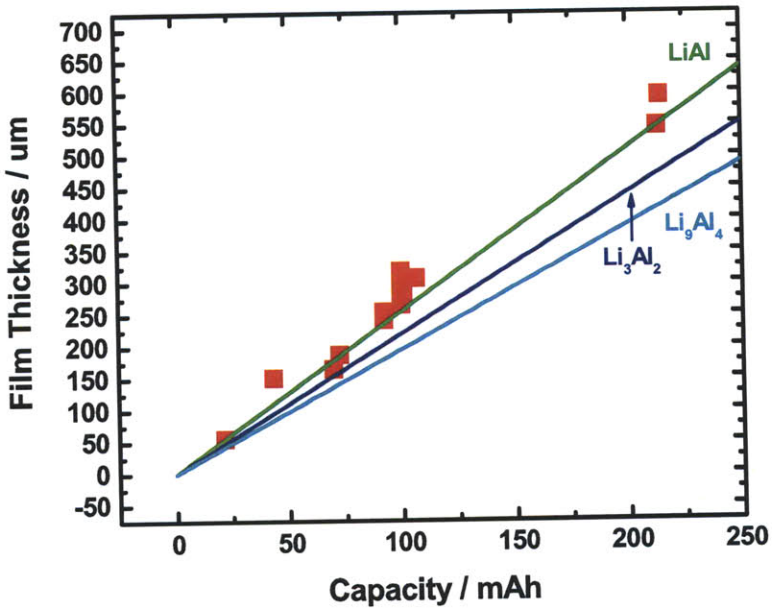


Figure 5-21. Film thickness versus capacity for aluminum-based actuators discharged through a fixed 10 ohm resistor for a given time. Also plotted are the expected thicknesses of the three Li-Al intermetallics. The data are linear and follow the LiAl line indicating that as the reaction product.

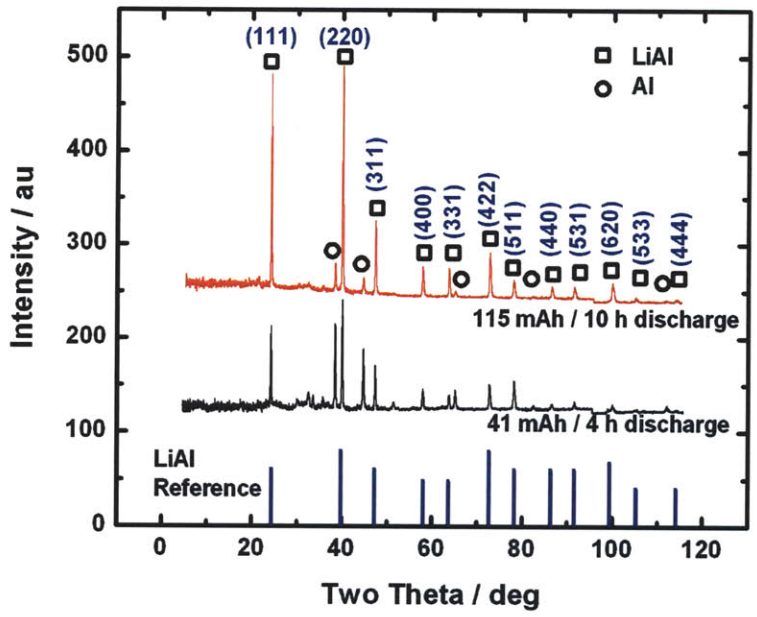


Figure 5-22. XRD spectra for aluminum-based actuators discharged through a fixed 10 ohm resistor. The only phases detected are LiAl and Al. LiAl reference intensities with corresponding planes are also given.

Two-dimensional (2D) x-ray spectra do not indicate any texturing present in the LiAl intermetallic film or aluminum substrate. Figure 5-23 shows a 2D spectrum centered at 20 degrees two-theta for the sample discharged for 10 hours. The bright ring is the diffraction from the (111) plane at 24.367 degrees two-theta. The continuity of the brightness across the range of the detector indicates there is no measurable texture. In Figure 5-22, however, there are clearly discrepancies between the relative peak intensities of the LiAl data and the reference card. The low angle peaks are much more intense than the high angle peaks. These spectra were comprised of integration of the rings from the 2D spectra over five separate measurements. Each 2D spectra spanned a range of 30 degrees two-theta centered at 20, 40, 60, 80, and 100 degrees two-theta and the incident

angle of the x-ray beam was always one-half of the centered two-theta angle. As the incident angle increases for the measurements at higher angles, the volume of sample that is irradiated by the beam decreases. This leads to the overall lower intensities at higher angles. However, within any of these five spectra individually (when the incident angle is not changing), the relative peak intensities are consistent with the reference card. Therefore, there is no observable texture in the LiAl film.

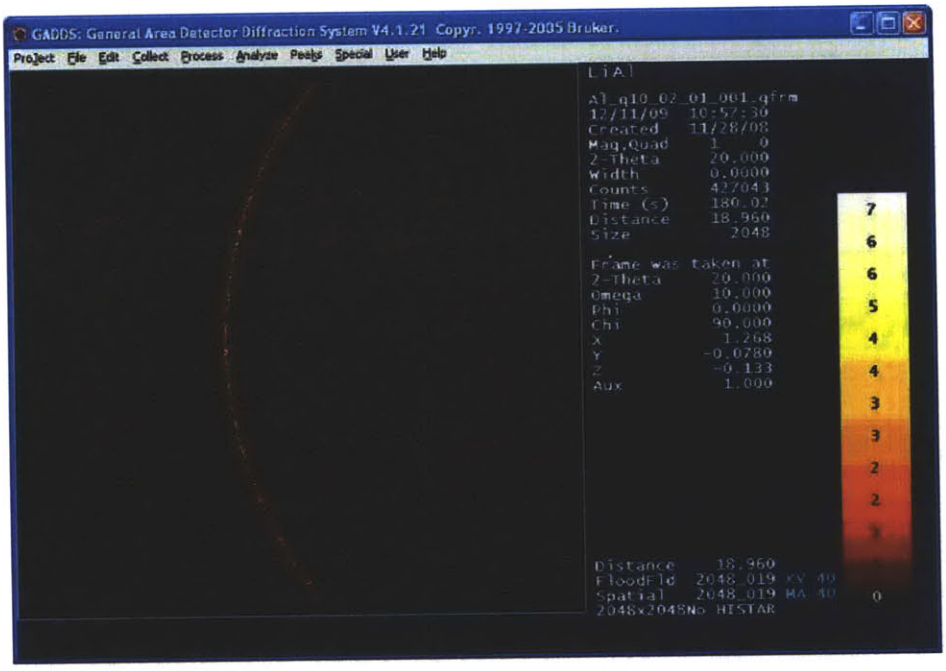
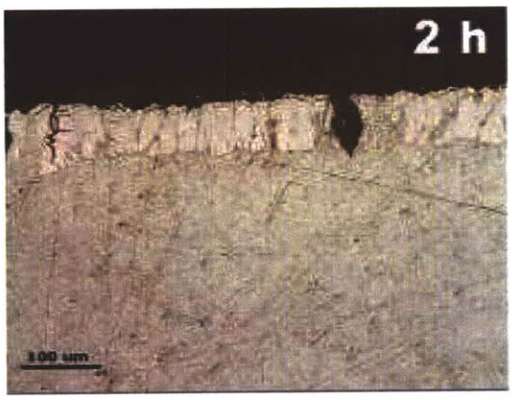
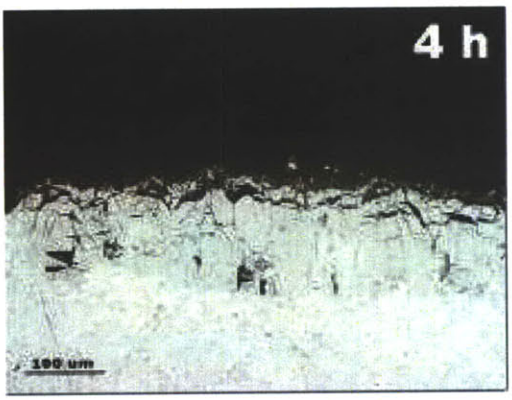


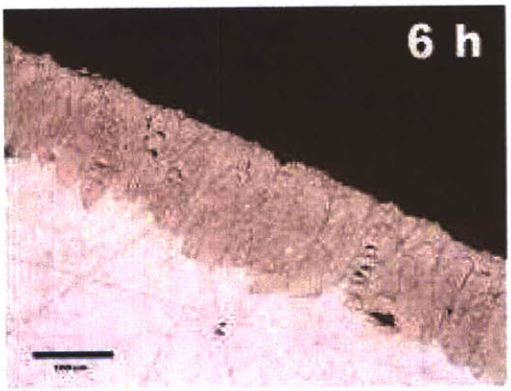
Figure 5-23. Two-dimensional x-ray spectra centered at 20 degrees 2-theta for a sample discharged to 115 mAh (10 h discharge through a 10 ohm resistor). The bright ring is from the (111) plane and the even intensities throughout indicate there is no texturing.

Closer views of the microstructure reveal the same columnar growth morphology as the galvanostatically discharged samples (Figure 5-24). The feature heights approximate the film thickness at a two hour discharge (Figure 5-25), indicating a fairly dense film and little stress buildup. For discharge times longer than two hours, significant cracking occurs reducing the feature heights to between 25 to 37 μm which indicates an

increased stress state within the film. As the feature heights do not continue to decrease, it is assumed the film reaches a steady stress state. The feature widths, however, do not significantly vary, remaining around 20 μm throughout discharge indicating that these are fixed early on in the nucleation and growth process of the film, similar to what was observed in the galvanostatically discharged samples.


2 h
100 um


4 h
100 um


6 h

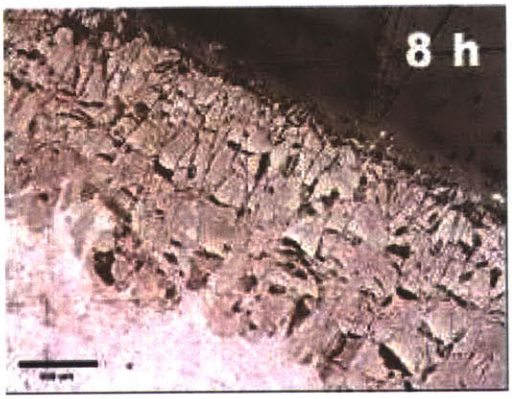

8 h

Figure 5-24. (Previous page) Optical micrographs of the intermetallic film formed for separate samples discharged through a fixed 10 ohm resistor for 2, 4, 6, and 8 hours. The scale bars are 100 μm.

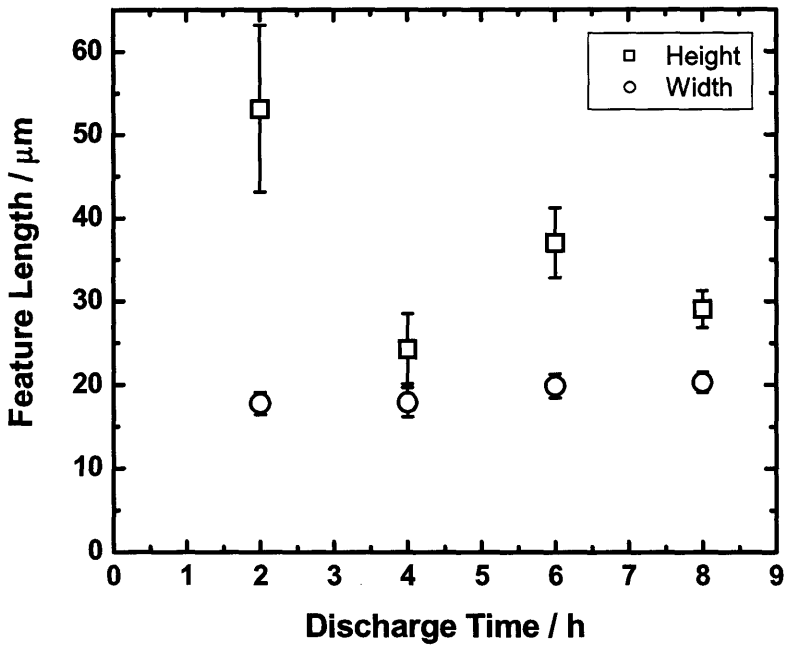


Figure 5-25. Feature heights and widths for aluminum-based actuators discharged through a fixed 10 ohm resistor for a given time. Feature heights decrease with inreasing discharge while feature widths do not significantly vary.

Between the galvanostatic and self-powered microstructure data, the feature widths don't increase with either nucleation rate or discharge time. Their size is fixed early in the process and is likely fixed by the aluminum microstructure size. The film will coalesce around 20 mAh (from the self-powered, 2 hour discharged sample) and is 50 μm thick at that point. The stress in the film is not high enough to cause significant cracking within the film or significant bending in the aluminum. Both events occur as the film grows between 50 μm and 100 μm. Further film growth does not cause significantly greater cracking. Films grown at a slower rate show decreased cracking as well indicating

the film can accommodate stresses given enough time. At increased rate, significantly more cracking occurs even at a given film thickness.

5.2.4 Actuation Energy Density

In order to determine the actuation energy of these devices, aluminum-based actuators of the same configuration in previous sections were discharged through a 10 ohm resistor for 24 hours under discrete constant loads up to 350 N applied by an Instron materials testing machine. Displacement curves for tests up to 20 N were shown in Figure 4-13. Above 20 N, the displacement curves decrease with increasing load at any given capacity. The displacements at 200 mAh and corresponding work-per-cycle (defined as $\sigma\varepsilon$, the stress multiplied by the actuation strain[22]) are shown in Figure 5-26. At fixed loads of 4 N and below, there is enormous displacement due to the bifurcation of the actuators as shown in Figure 5-1 on the right (also see Figure 4-13). Above this threshold, folding is suppressed (Figure 5-1 middle), but the displacement at 200 mAh remains fairly constant at 2.75 mm up to 20 N (also see Figure 4-13) before decreasing with increasing loads. The device fails at 350 N due to compromised packaging and internal shorting; the actuation may still be able to proceed in a more robust construction. Nevertheless, this will be taken as the blocked force to give a lower limit to the actuation energy density. The work output is maximized at 925 kJ m^{-3} at 250 N load.

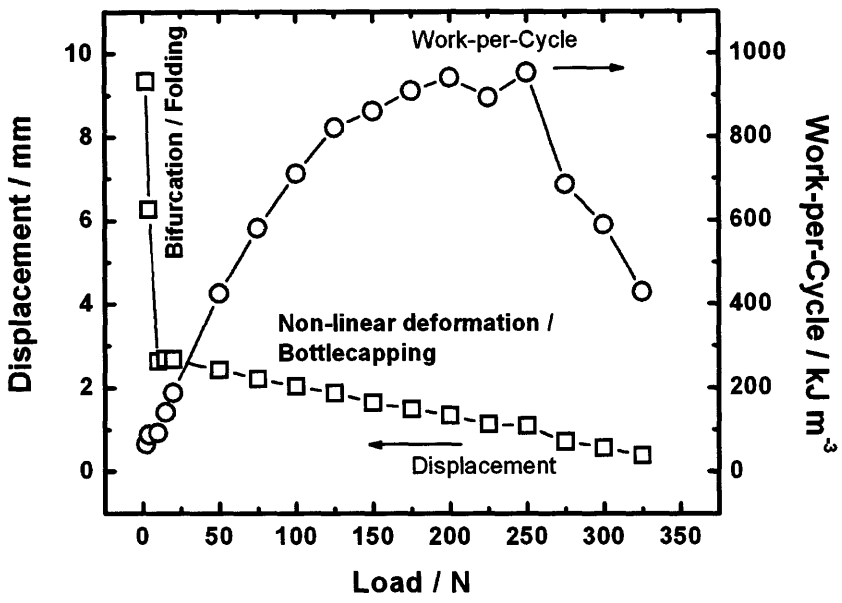


Figure 5-26. Displacement at 200 mAh and work-per-cycle for aluminum-based actuators discharged through a fixed 10 ohm resistor at discrete external mechanical loads. Large displacements are achieved at low loads due to bifurcation/folding whereas smaller displacements are realized at higher loads as the samples take a 'bottlecapped' shape.

The suppression of folding can be rationalized by considering the opposing bending moments. The growth of the intermetallic film will generate a bending moment on the order of 10^{-2} to 10^{-1} N m (from Equation 4.1), depending on the thickness of the film. The applied moment from a 4 N load is 0.04 N m (from Equation 4.2), on the order of the film-induced moment. The packaging and other components also add extra stiffness. At greater loads, these forces exceed the moment generated by the film growth, suppressing the folding. Indeed, at higher loads, the samples take a dramatically 'bottlecapped' shape where there is large curvature near the edges of the sample and the center of the sample is convex (there is a discontinuity in the curvature) as shown in Figure 5-27.

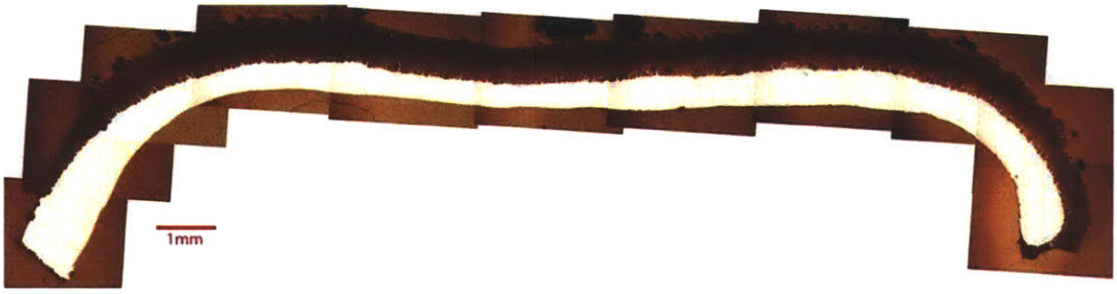


Figure 5-27. Cross-section of an aluminum-based actuator discharged through a fixed 10 ohm resistor for 24 hours under 6 N load. The center of the sample is convex compared to the typical concave downward.

Taking 2.75 mm as the free displacement and 350 N as the blocked force, the actuation energy density of this device is 1700 kJ m^{-3} based on the active aluminum actuation element. While this is less than one percent of the theoretical value for full conversion of the Al (2188 MJ m^{-3}, from Section 1.1), it is nevertheless very high compared to other (reversible) actuation technologies. Shape memory alloys (SMA's) provide a useful comparison as they are amongst the highest energy density active materials. Conducting polymers are also convenient as their actuation mechanism is similar (ion insertion between polymer chains). Electrochemical actuators based on lithium alloying compares favorably to SMA's which have typical work densities from 100 – 1000 kJ m^{-3}.[23] Similarly, these work densities exceed that of typical conducting polymers (100 kJ m^{-3}) which have a peak energy density of only 1000 kJ m^{-3}.[23]

Further accounting for the density of the aluminum, the weight-based specific energy is 625 J kg^{-1}. This exceeds the specific energy of 460 J kg^{-1} for SMA's[24] and the specific energy of 44 J kg^{-1} for conducting polymers.[25] The high specific energy makes these actuators much more attractive for weight critical applications.

The mechanical power output of the device, however, is limited as it relies on mass transport and phase changes for the actuation mechanism. This, combined with the

plastic deformation necessary for the large displacements, makes these devices best suited to prolonged, single-use applications.

5.3 Summary

In this chapter, we have detailed the actuation properties of a packaged device based on electrochemical alloying of lithium with tin or aluminum. The differences in partial molar volume with respect to lithium do not affect the actuation of these materials significantly. Rather, material properties are more influential. Tin-based actuators have been shown to be more sensitive to external loadings due to their lower Young's modulus and yield strength. Displacements nearly 10 times the original thickness of the active element can be realized. Actuators have been demonstrated to be self-powered but can also be controlled via conventional electrochemical means yielding similar displacement results. The discharge rate and overall state-of-discharge show marked effects on the morphology of the intermetallic microstructure. More stress-relief cracking is evident at longer discharge times and higher discharge currents. Further, the actuation energy density was found to be 1700 kJ m^{-3}, comparable or superior to shape memory alloys and conducting polymers.

5.4 References

1. Linden, D. & Reddy, T.B. *Handbook of Batteries*. (McGraw-Hill: New York, 2002).
2. Dey, A.N. Electrochemical Alloying of Lithium in Organic Electrolytes. *Journal of The Electrochemical Society* **118**, 1547-1549(1971).
3. Besenhard, J., Yang, J. & Winter, M. Will advanced lithium-alloy anodes have a chance in lithium-ion batteries? *Journal of Power Sources* **68**, 87-90(1997).
4. Wang, X., Sone, Y. & Kuwajima, S. In Situ Investigation of the Volume Change in Li-ion Cell with Charging and Discharging: Satellite Power Applications. *Journal of the Electrochemical Society* **151**, A273 - A280(2004).

5. Wang, X. et al. Understanding volume change in lithium-ion cells during charging and discharging using in situ measurements. *Journal of the Electrochemical Society* **154**, A14 - A21(2007).
6. Garreau, M. et al. Cycling behavior of lithium and aluminum-lithium electrodes in propylene carbonate and dioxolane electrolytes. *Proceedings of the workshop on lithium nonaqueous battery electrochemistry* **80-7**, 158-180(1980).
7. Rao, B., Francis, R. & Christopher, H. Lithium-aluminum electrode. *Journal of the Electrochemical Society* **124**, 1490-1492(1977).
8. McAlister, A. Aluminum-lithium binary diagram. *ASM Alloy Phase Diagrams Center* (2006).at <http://www.asminternational.org/AsmEnterprise/APD>
9. Crystal lattice structures web page. at <http://cst-www.nrl.navy.mil/lattice/>
10. Winter, M. & Besenhard, J. Electrochemical lithiation of tin and tin-based intermetallics and composites. *Electrochimica Acta* **45**, 31-50(1999).
11. Sangster, J. Lithium-tin binary diagram. *ASM Alloy Phase Diagrams Center* (2006).at <http://www.asminternational.org/AsmEnterprise/APD>
12. Wang, C., John Appleby, A. & Little, F.E. Electrochemical study on nano-Sn, Li4.4Sn and AlSi0.1 powders used as secondary lithium battery anodes. *Journal of Power Sources* **93**, 174 - 185(2001).
13. Kumagai, N., Kikuchi, Y. & Tanno, K. Cycling behaviour of lithium-aluminum alloys formed on various aluminum substrates as negative electrodes in secondary lithium cells. *Journal of Applied Electrochemistry* **22**, 620 - 627(1992).
14. Ding, F., Liu, Y. & Hu, X. Characteristics of lithium-gel battery based on a Li-Al alloy anode. *Electrochem. Solid-State Lett. (USA)* **9**, 72 - 5(2006).
15. Howatson, A., Lund, P. & Todd, J. *Engineering Tables and Data, 2nd Edition.* 41(Chapman & Hall: New York, 1991).
16. Melendres, C. & Sy, C. Structure and cyclic discharge behavior of LiAl electrodes. *Journal of The Electrochemical Society* **125**, 727-731(1978).
17. Epelboin, I. et al. Behavior of secondary lithium and aluminum-lithium electrodes in propylene carbonate. *Journal of the Electrochemical Society* **127**, 2100-2104
18. Baranski, A. & Fawcett, W. The formation of lithium-aluminum alloys at an aluminum electrode in propylene carbonate. *Journal of the Electrochemical Society* **129**, 901-907(1982).
19. Valoen, L. & Reimers, J. Transport properties of LiPF6-based Li-ion battery electrolytes. *Journal of the Electrochemical Society* **152**, A882-891(2005).
20. Taghikhani, V., Modarress, H. & Vera, J. Individual anionic activity coefficients in aqueous electrolyte solutions of LiCl and LiBr. *Fluid Phase Equilibria* **166**, 67-77(1999).
21. Bard, A. & Faulkner, L. *Electrochemical Methods: Fundamentals and Applications.* (John Wiley & Sons: Hoboken, NJ, 2001).
22. Xi, B. et al. Poly(3-methylthiophene) electrochemical actuators showing increased strain and work per cycle at higher operating stresses. *Polymer* **47**, 7720-7725(2006).
23. Madden, J. et al. Artificial muscle technology: physical principles and naval prospects. *IEEE Journal of Oceanic Engineering* **29**, 706-728(2004).
24. Kohl, M. *Shape Memory Microactuators.* (Springer: Berlin, 2004).
25. Spinks, G. & Truong, V. Work-per-cycle analysis for electromechanical actuators. *Sensors and Actuators A* **119**, 455-461(2005).

6 Controlled Folding Aluminum-based Actuator Design and Performance

In Chapter 5, circular actuators were demonstrated to fold at high capacities if actuated against low mechanical loads. This gave dramatic displacements almost 10 times the original thickness of the device upon bifurcation. In this chapter, we present a modified actuator to control this folding along a given axis and to ensure large displacements.

6.1 Materials and Methods

The same materials used for the circular disc actuators in Chapter 5 were used here. The modification made to ensure folding was to mask the surface of the disc such as to only expose a strip ¼-inch wide across one diameter (Figure 6-1a). In addition, a rectangular geometry was utilized providing an overall larger sample with greater mechanical advantage. The masking material was Krylon® spray paint. These samples were 22 mm by 26 mm and the reaction area was placed across the shorter width (Figure 6-1b). Different thicknesses of these rectangular actuators were tested and compared as well. The rectangular actuators were sealed in a stiffer metallized polymer packaging material with a formed well for the sample.

As the curvature develops across the exposed reaction area, the masked regions provide 'lever arms' to amplify the displacement. The aspect ratio of the reaction area ensures unequal principal curvatures from the onset of deformation, as discussed in Chapter 4. A larger curvature will develop around the longer axis of the reaction area as the bending moment is greater around the longer axis (from Equation 4.1).

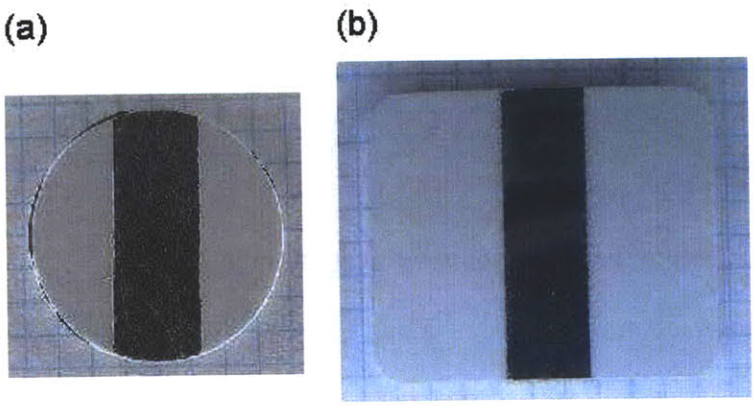


Figure 6-1. Controlled folding samples in (a) a circular geometry and (b) a rectangular geometry. The center strip is the reaction area of exposed aluminum while the rest of the surface has been masked.

In addition to the testing equipment mentioned in previous chapters, the rectangular actuators were electrochemically controlled using a BioLogic VMP3 battery tester/potentiostat. The displacements were measured using Keyence GT2-H12L digital contact sensors and Keyence GT2-71N/72N digital amplifiers. The actuators were held in test fixtures such that the actuator forced up a piston which was restricted only to vertical displacement.

6.2 Controlled Folding Circular Actuators

Masked circular actuators were discharged in a self-powered mode through a 10 ohm resistor similar to the unmasked disc actuators in Chapter 5.2. Both sets were measured using a spring loaded LVDT. The resulting displacements and currents versus time are shown in Figure 6-2a and also compared with a typical actuation behavior of unmasked disc actuators, which will be referred to as 'full disc' actuators.

6.2.1 Actuation Results

The corresponding displacement versus capacity density curves are shown in Figure 6-2b. The areal capacity density normalization is equivalent to absolute film thickness in a sample and gives a convenient way to compare samples with different reaction areas or geometries.

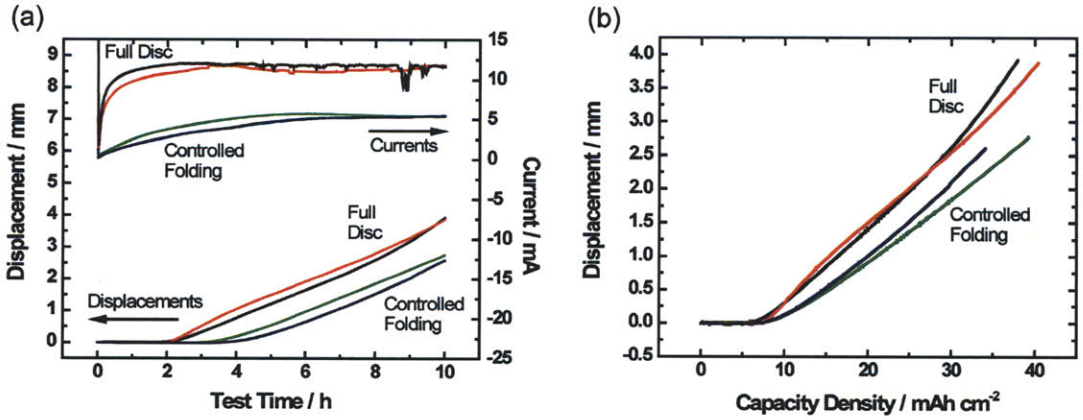


Figure 6-2. (a) Displacement and current versus time and (b) displacement versus capacity density compared between unmasked ('full') disc and controlled folding disc actuators. The full disc actuators demonstrate higher rates on both scales.

The masking reduces the reaction area to 42% of the full disc – 1.19 cm^2 versus 2.85 cm^2. This should increase the resistance of the cell by a proportional amount and correspondingly decrease the current. The decreased current is observed, but it's not necessarily proportional to the decreased area throughout the discharge because the geometry of the reaction area has also changed. Electric field variances and internal impedances also have effects and differences in the resulting current profiles can be seen. The current for the full disc actuators reach 12 mA within 1 hour. The current for the controlled folding actuators slowly increase to 5 mA in 5 or 6 hours. For at least half of the test, they are well below 42% of the current density of the full disc actuators.

Both full disc and controlled folding samples show similar displacement rates (dy/dt) after their initial incubation. The full disc samples show a slightly greater displacement per capacity density (dy/dq) though. This is due to the smaller arc length in the controlled folding sample (1/4 in versus 3/4 in) which decreases the displacement per unit thickness of the intermetallic film even with the amplification of the lever arms (Equations 4.5 and 4.6). The calculated displacements from the model outlined in Chapter 4 are shown in Figure 6-3. Relatively, the controlled folding actuator should have less displacement per areal capacity density than a full disc, agreeing well with the measurements accounting for the shift in incubation capacity. The measured displacements were done on packaged actuators with an external force from the spring-loaded LVDT, therefore, the absolute displacements are significantly less than the calculated values as discussed in Chapter 4.

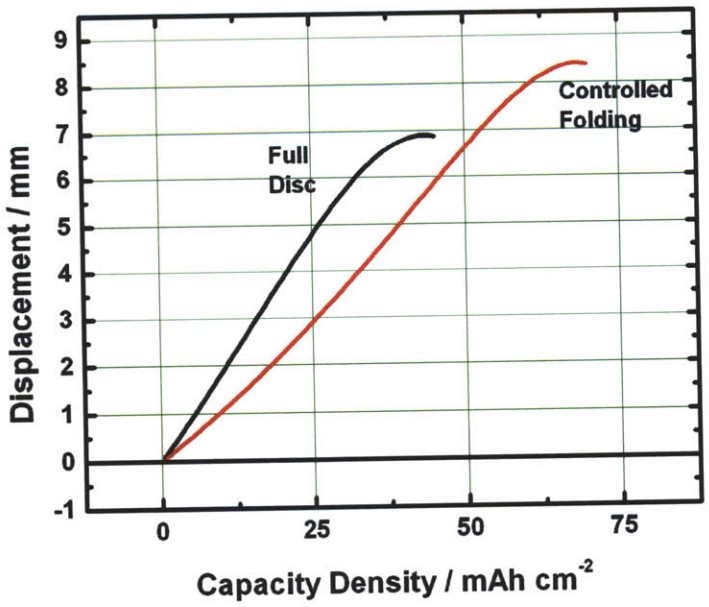


Figure 6-3. Calculated displacements for a full disc and controlled folding actuator.

The advantages of the controlled folding samples are that it can reach a larger displacement in a predictable manner and it can reach a given displacement with less capacity compared to a full disc sample (greater dy/dQ). The aspect ratio of the reaction area is controlling the bifurcation whereas for a full disc, the instability could manifest itself along any diameter. By using the lever arms to amplify the displacement though, there should also be a corresponding reduction in the load capacity of these types of actuators.

6.2.2 Microstructure

Cross-sections of the sample are shown in Figure 6-4 both across and parallel to the folding axis. The masking clearly blocks any reaction from occurring over the lever arms. The growth of the intermetallic here shows almost half of it is above where the original surface of the aluminum was. The longitudinal cross-section shows virtually no bending. The significant compression along the bottom surface though creates regions of local buildup as evidenced by its deviation away from a smooth, flat surface.

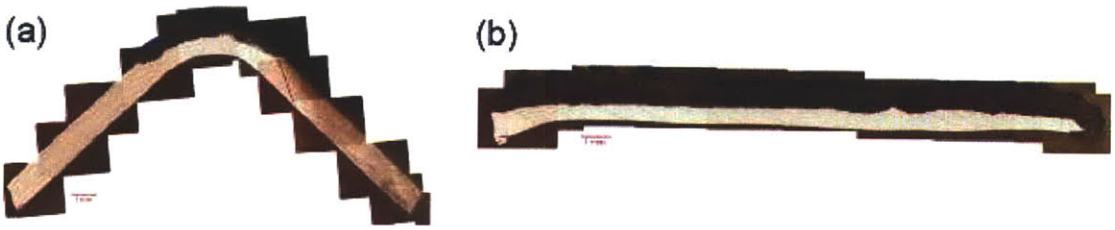


Figure 6-4. Cross sections of the actuation element in a controlled folding circular actuator (a) perpendicular and (b) parallel to the folding axis after actuation and removal from the packaging.

6.3 Controlled Folding Rectangular Actuators

Moving to a rectangular geometry for a controlled folding actuator provides a few advantages over the circular geometry. First, it provides two edges of support as the actuator is bending. A circular actuator is only supported on two points of the disc and must rely on the packaging or other external means for balance. Second, a rectangular geometry also provides an easier method to change the length of the lever arms as well as the width of the reaction area individually. These two are inherently linked given a circular geometry. Although neither of these variables were systematically tested for this thesis, the ability to change the lever arm length and reaction area width provides flexibility moving forward in tailoring actuation properties for specific applications.

Controlled folding rectangular actuators were pre-lithiated at 10 mA for 1.5 h to bring these beyond the incubation period and initiate the displacement. Further actuation was done through a 221 ohm resistor in self-powered mode or galvanostatically at various fixed currents. Actuation tests without this pre-lithiation step resulted in localized 'hot spots' of reaction creating isolated regions of significant intermetallic build-up. This created a 'dimple' or 'divot' on the opposite side of the electrode from the localized deformation.

6.3.1 Self-Powered Actuation Results

Initial tests were conducted on 1.0 mm thick samples, however, these provided inconsistent results and were very sensitive to external mechanical loads. Modified designs were attempted with little success including machining grooves or a channel opposite of the reaction layer. Pre-bending the cells led to enhanced displacements

(Figure 6-5), however, the exact reproducibility of the pre-bend was poor as they were manually aligned and deformed over an allen wrench. As this was done on a packaged device, it was impossible to guarantee alignment between the pre-bend and the exposed reaction area. Bends were made to different apex heights – 0.5, 1.0, and 1.5 mm – all of which exhibited greater displacement at a given capacity than the best non-bent samples. Pre-bending introduces plastic deformation in the aluminum, decreasing the effective Young's modulus and, correspondingly, the flexural rigidity, D, of the substrate given in Equation 4.2:

$$D = \frac{Eh^3}{12\left(1-\nu^2\right)} \tag{6.1}$$

where E is the Young's modulus, h is the thickness, and ν is Poisson's ratio. A given bending moment (i.e. a given capacity), will subsequently induce greater curvature yielding enhanced displacement.

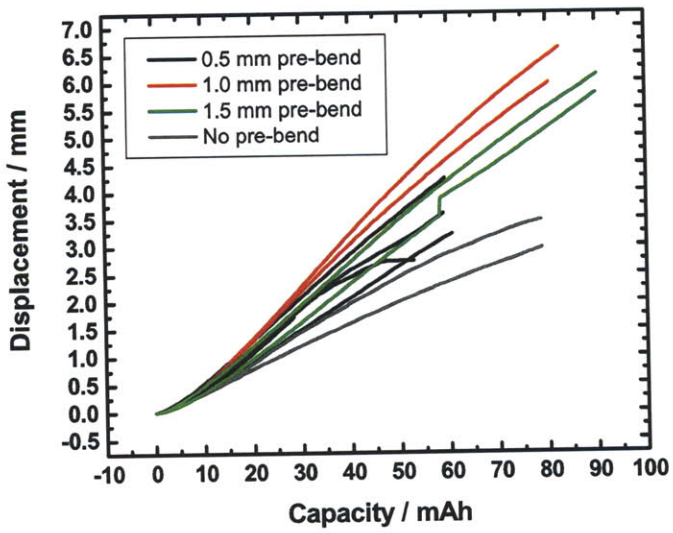


Figure 6-5. Displacement versus capacity curves for samples pre-bent prior to discharge compared to non-pre-bent samples all under a 200 g load. Pre-bent samples exhibit greater displacements.

Instead, moving to 1.5 mm thick aluminum gave much more consistent and slightly greater displacement per capacity than 1.0 mm thick samples, although slightly less than some of the pre-bent samples (Figure 6-6). The sharp jumps in the displacement curves result from intermittent internal shorting of the cell. The 1.5 mm samples had similar displacements up to 400 g external load with only a slight decrease in displacement at 600 g and 800 g. While increasing the thickness should decrease the displacement by the flexural rigidity argument given above, this is not observed. From another standpoint, this increased flexural rigidity will also allow the sample to withstand greater external mechanical loads without any effect, something that could be suppressing the displacement of the 1.0 mm samples.

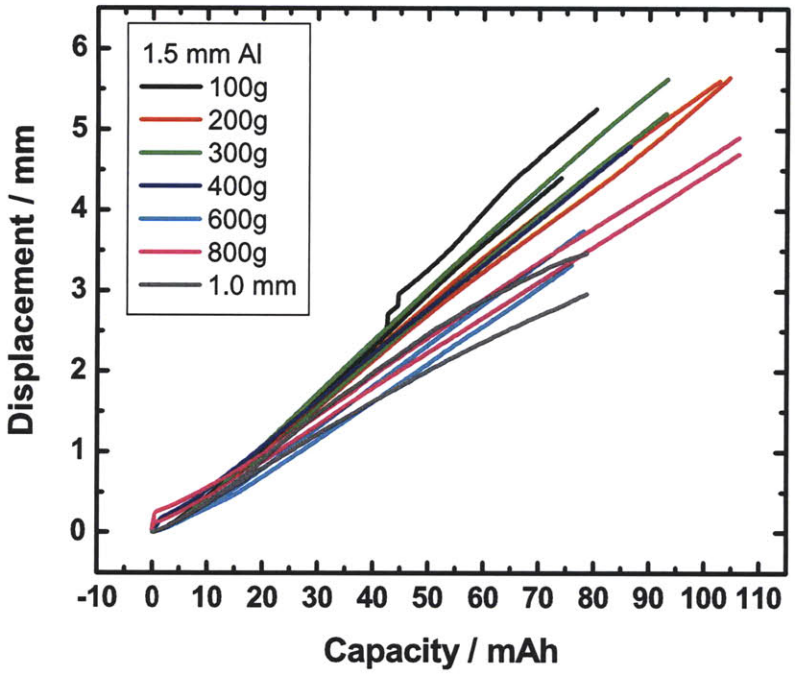


Figure 6-6. Displacement curves for 1.5 mm thick, controlled folding, rectangular actuators at various fixed loads. These exhibit greater displacement and less load sensitivity than 1.0 mm thick samples.

6.3.2 Displacement Rate Control via Galvanostatic Discharge

Galvanostatic testing of 1.5 mm thick rectangular aluminum-based actuators yileded a maximum stable displacement rate of ~0.55 mm h^{-1} at 10 mA. Figure 6-7 plots the displacement and cell voltage versus capacity for these samples discharged at different currents. For any given displacement curve, the capacity axis can be converted to a time axis by dividing by the current. Therefore, the observed slopes are indicative of displacement rate, dy/dt, however these rates can not be compared directly between samples discharged at different currents from this plot. All of the displacement curves

start out with a similar slope. At 10 mA or higher, there is an inflection in the displacement curves (Figure 6-7) creating a bimodal characteristic in the displacement rates. This point occurred at 55 mAh for 10 mA discharge current, 40 to 50 mAh for 15 mA, 20 mAh for 20 mA, and 10 mAh for 25 mA. As the capacity of the inflection point decreased with increasing current, this led to an overall smaller displacement as the current increased as well. This inflection also corresponded to irregular and noisy voltage spikes, all of which occurred at negative voltages (Figure 6-7), hinting that the reduced displacement rate may be related to plating lithium on the reaction surface and possible shorting through the separator. For stable actuation, separate potentiostatic tests were conducted confirming the maximum displacement of 0.55 mm h^{-1} by discharging at 1 mV (an overpotential of ~350 mV). The maximum current was predictably around 10 mA but decreased in the later stages of discharge.

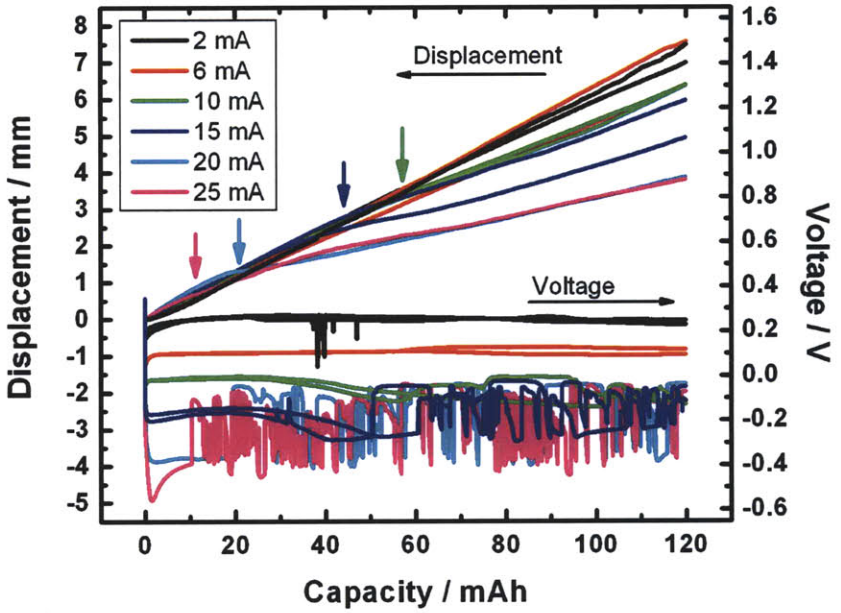


Figure 6-7. Displacement and potential versus capacity for galvanostatically discharged rectangular controlled folding actuators. At high currents, an inflection in the displacement curves correspond with irregularities in the potential curves, as indicated by the vertical arrows, giving a bimodal displacement rate.

Increasing the thickness of the aluminum even farther to 2.0 mm reduced the displacement per capacity. The bending moment per unit length around the periphery, M, imparted by the film is given in Equation 4.1:

$$M = \frac{1}{2} h_s \varepsilon_m M_f h_f \tag{6.2}$$

where h_s is the substrate thickness, ε_m is the mismatch strain, M_f is the effective modulus of the film, and h_f is the film thickness. The imparted bending moment increases proportionally to the substrate thickness. However, the flexural rigidity of the substrate increases by h_s^3 as shown in Equation 6.1. As the flexural rigidity increases faster than the bending moment, the displacement is expected to be lower for a given capacity (equivalently, film thickness and time, for galvanostatically discharged samples).

As the reaction area was the same as for the 1.5 mm samples, only currents up to 10 mA were tested to avoid significant lithium plating. The average displacement rates for both 1.5 and 2.0 mm samples are shown in Figure 6-8. The error bars indicate the standard deviation of the instantaneous displacement rates in the data for a given sample, which includes thermal drift in the sensor. The maximum displacement rate dropped to ~0.30 mm h^{-1}. Applying the model described in Chapter 4, the calculated displacements versus capacity are shown in Figure 6-9. As mentioned above, for galvanostatic tests, the capacity scale can be converted to a time scale by dividing by the current. The predicted displacement from Equation 4.6 for a 1.5 mm sample remains greater than the predicted displacement for a 2.0 mm sample by a factor of 1.78 – 1.94. The actual displacement rates for the 1.5 mm samples are a factor of 1.61 – 1.92 greater, agreeing well with the calculations.

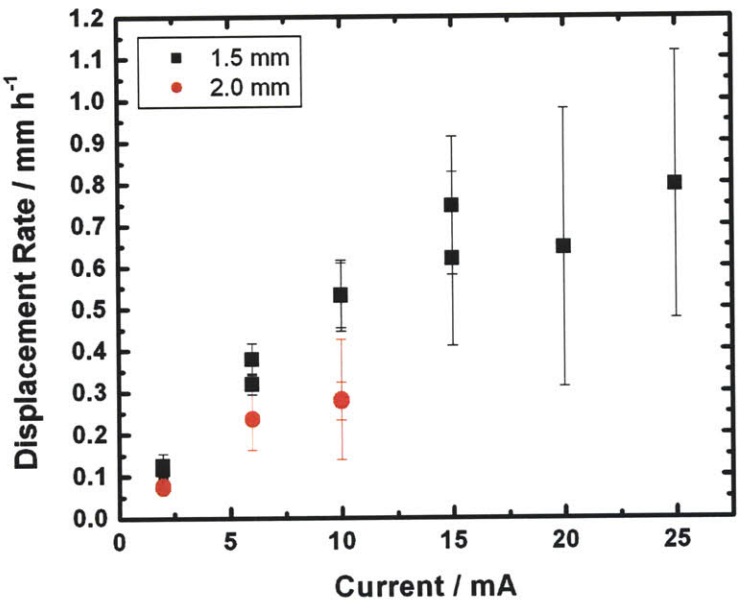


Figure 6-8. Displacement rate versus galvanostatic current for 1.5 mm and 2.0 mm thick rectangular controlled folding samples. The standard deviation of the displacement rate increases significantly at high currents due to the bimodal slopes in the displacement curves (Figure 6-7).

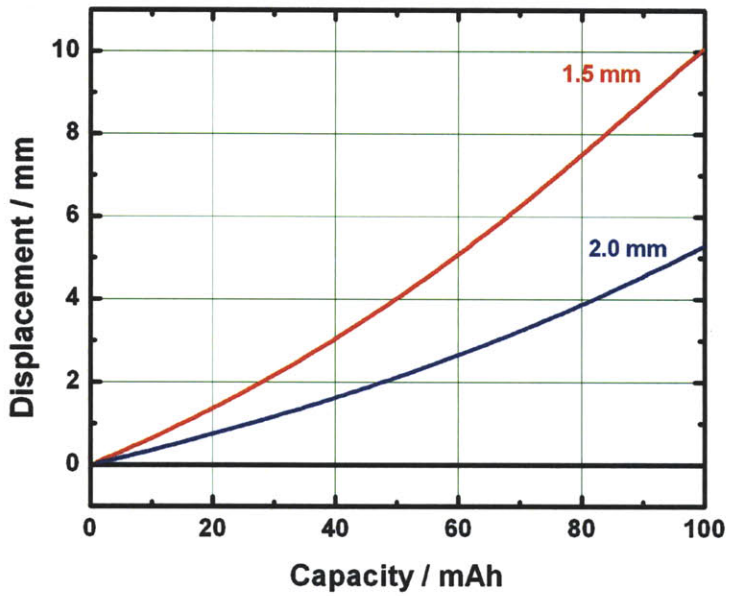


Figure 6-9. Calculated displacements versus capacity for controlled folding rectangles 1.5 and 2.0 mm thick. The displacement for a 1.5 mm thick actuator is 1.78 – 1.94 times greater than for a 2.0 mm thick actuator.

6.4 Summary

Controlled folding actuators have been demonstrated capable of the large displacements seen at low mechanical loads for the disc actuators. Folding was controlled by masking disc and rectangular samples such that the reaction area had an aspect ratio of ~1:3 and the bending was primarily around the longer axis. Full disc samples demonstrated greater displacements on a time and capacity density basis than controlled folding discs. This is attributed to the reduced reaction area and difference in reaction area geometry. The controlled folding rectangular actuators were sealed in a stiffer packaging material and showed more reliable displacements if they were pre-bent before discharging. Controlled folding rectangular actuators of 1.5 mm thickness showed

improved consistency and load capability than 1.0 mm thick samples. These devices exhibited a maximum stable displacement rate of 0.55 mm h^{-1} at 1.5 mm thick. Increasing the thickness to 2.0 mm drops the maximum displacement rate to 0.30 mm h^{-1} agreeing with the displacement model introduced in Chapter 4.

7 Displacement Rate Control of Self-Powered Actuators

In practice, time-based rate control (*dy/dt*) is of critical interest. Certainly, galvanostatic control can be easily translated to a time basis, but translating a self-powered device to a time scale is not so trivial. In this chapter we will detail three different methods of controlling the displacement rate of self-powered electrochemical actuators: external resistance, duty cycle, and sample thickness. The first two methods regulate the discharge capacity of the cell whereas the third method uses mechanical stiffness to adjust the displacement rate.

7.1 External Resistance

In the previous chapter, self-powered actuators were discharged through a fixed 10 ohm resistor, which is typically less than the internal resistance of the cell. Reducing the external resistance will not increase the displacement rate significantly because it is already limited by the internal resistance. Increasing the external resistance should decrease the displacement rate. Ideally, there would be a linear correlation based on Ohm's Law as the current should also decrease proportionally to the increased resistance.

In these tests, we used ¾ in diameter aluminum-based actuators as described in Chapter 5.2 and discharged them through fixed resistors of 10, 50, 221, 325, 550, and 1480 ohms, after a pre-lithiation discharge up to 20 mAh to overcome the incubation. The displacements were measured using a spring-loaded LVDT. The displacements and resulting displacement rates are shown in Figure 7-1. Between 10 and 325 ohms, the displacement rate drops quickly from around 0.5 mm h^{-1} to 0.02 mm h^{-1}. At low resistances though, there is greater variability due to the influence of the internal

resistance. At resistances even greater than 325 ohms, the displacement rate drops much more slowly as the external resistance dominates the overall impedance. At 1480 ohms, the displacement rate is 0.005 mm h^{-1}.

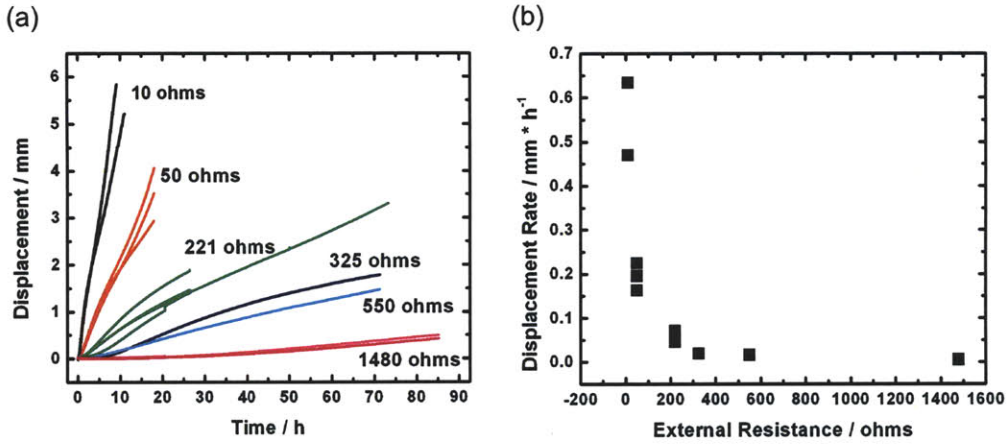


Figure 7-1. (a) Displacement curves for self-powered, aluminum-based disc actuators with different fixed external resistances. (b) Average displacement rates for curves in (a). Increasing the external resistance decreases the displacement rate, but the resolution is low.

The influence of internal impedance can also be seen in the current response at different external resistances. The current response up 220 ohms shows variation early on whereas above that, the current response is very flat (Figure 7-2). As discussed in Chapter 4, the low frequency impedance of the cell initially starts very high and drops as the capacity increases. At early times, this varying impedance can still dominate over the external resistance or, at least, significantly contribute to the total impedance, which is why the current varies with time at low resistances. At high resistances, the current response is very flat indicating that the external resistance is much greater than the internal impedance.

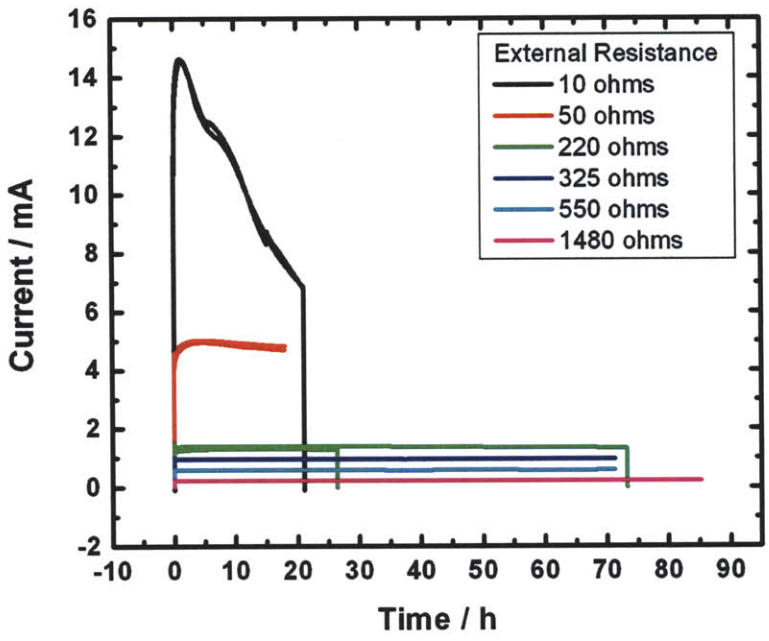


Figure 7-2. Current response for self-powered aluminum-based disc actuators undergoing self-powered discharge at various fixed resistances. At high resistances, the current profiles are flat because the external resistance dominates over the internal impedance.

The sensitivity of the displacement rate to external resistance is very high at low resistances, making it difficult to finely tune the displacement rate to a given value. Utilization of this method is only useful at extremely low displacement rates where the external resistance completely dominates over the internal resistance of the device.

7.2 Duty Cycle

Duty cycle control was demonstrated on tin-based actuators. The actuator construction was similar to those described in Chapter 5.2 with the exception of substituting a tin disc for the aluminum, maintaining the ¾ in diameter and 1.0 mm thick geometry.

Duty cycle control refers to opening and closing the circuit in periodic intervals by means of a relay or switch. The percentage of duty cycle refers to the ratio of the time when the circuit is closed ('on' or 'active' state) to the total open ('off' or 'inactive' state) and closed period. In these tests, a tin-based actuator was discharged through a 10 ohm resistor in alternating 10 minute intervals between continuous discharge (100% duty cycle) and a lower percentage duty cycle controlled by an electronic relay (National Instruments 9481). The lower percentage duty cycles were 84%, 66%, 50%, 33%, and 16%, each maintaining a closed duration of one second with the off duration adjusted appropriately for the specified duty cycle. Thus, for the given 10 minute interval, a higher percentage duty cycle will allow the actuator to discharge more as the circuit spends more total time in the closed position passing more current.

Figure 7-3a shows the displacement and current versus time during periodic duty cycle discharge. The slope of the displacement curve changes noticeably between intervals of continuous discharge and lower percentage duty cycles. It is also clear that the displacement rate increases with increasing duty cycle percentage. The average displacement rate for a given duty cycle percentage is shown in Figure 7-3b and ranges from 0.35 mm h^{-1} for 100% duty cycle to 0.02 mm h^{-1} for a 16% duty cycle. The dotted line shows the ideal expected behavior based on the 100% duty cycle displacement rate. The deviations from ideal, especially at lower percentage duty cycles, are attributed to the electrochemical relaxation that can occur during the off intervals. Therefore, a fraction of the time during the on interval is spent re-polarizing the cell before actually discharging, leading to the non-ideal behavior. Tin shows a lower displacement rate than aluminum, as discussed in Chapter 5. However, we demonstrate that by using a simple switch or relay

mechanism, it is possible to finely tune the displacement rate and change it easily during operation. Similarly, running the actuator at a lower percentage duty cycle continuously could provide an overall slower steady-state displacement rate. Naturally, the switch or relay would require its own power source.

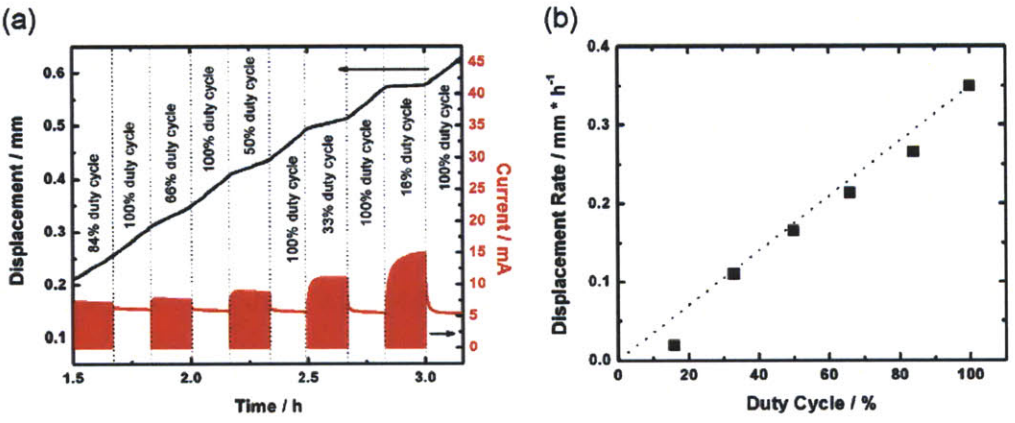


Figure 7-3. (a) Displacement and current response for a tin-based actuator under self-powered discharge through a 10 ohm resistor with varying duty cycles. (b) Average displacement rate during each duty cycle segment. The displacement rate varies linearly with duty cycle percentage.

A detailed view of the current and voltage for a 16% duty cycle is shown in Figure 7-4. The current is zero while the circuit is open, but when the circuit is closed, the current resumes and decays over the one second closed duration. The current during the closed interval of the duty cycle is higher than during the continuous discharge because the cell voltage has a chance to relax during the open interval. There is also a longer time-scale relaxation phenomenon occurring as the current during the closed periods increases with subsequent cycles. Immediately after opening the circuit, the cell quickly recovers the *iR* polarization, ~0.125 V for the tin actuator. Given time, there is also a relaxation of the concentration polarization. For lower percentage duty cycles, there is more time for the concentration polarization to relax, leading to a further increase in current when the

circuit is closed again. There is also a sharper decrease of the current during the closed intervals for lower percentage duty cycles as this polarization rebuilds. These variations are not resolved on the time scale shown in Figure 7-3a which is why they appear as solid bands.

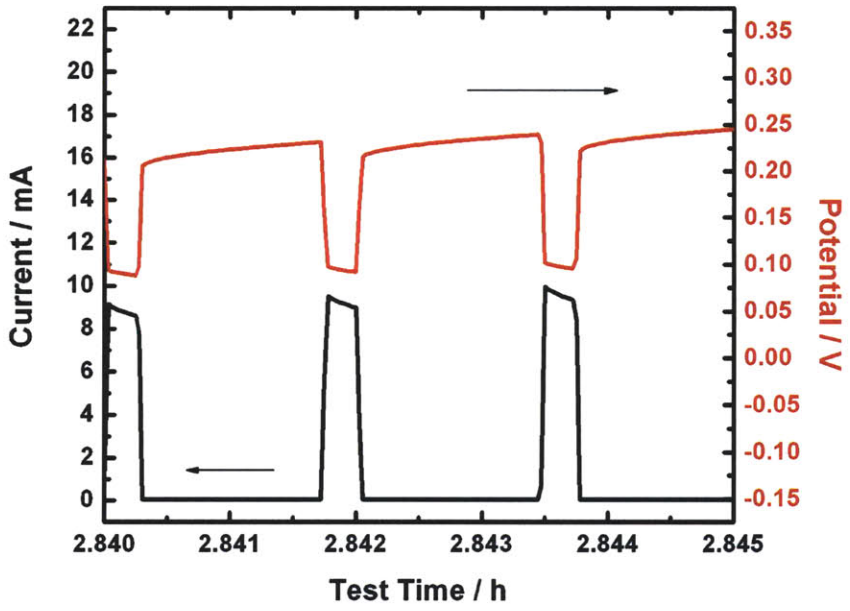


Figure 7-4. Current and voltage response during a 16% duty cycle through a 10 ohm resistor for a tin-based disc actuator. During off times, the current is zero and the voltage increases due to relaxation in the polarization. This increases the current compared to continuous discharge when the circuit is switched back on.

7.3 Substrate Thickness Effects

Thickness effects were briefly discussed in the previous chapter for the controlled folding rectangular actuators. Here, we further investigate the effects of thickness on aluminum disc based actuators. Actuators were constructed similar to those described in Chapter 5.2. Aluminum discs, ¾ in diameter were used as the active element with

thicknesses of 0.5, 0.75, 1.0, 1.27, and 2.0 mm. These were all actuated under self-powered discharge through a fixed 10 ohm resistor for 10 hours with no pre-lithiation under the LVDT spring load. As these actuators have the same reaction area and are discharged similarly, the capacity and, therefore, film thickness, are expected to evolve similarly among these samples.

Figure 7-5 shows the resulting displacement curves versus time for actuators of different thicknesses. The average displacement rates after the incubation period are shown in Figure 7-6. Thinner substrates have greater displacement rates. The displacement rates range from 0.14 mm h^{-1} for 1.50 mm samples to around 0.95 mm h^{-1} for 0.50 mm samples. In addition, the incubation capacity also decreases as the disc gets thinner. Both of these phenomena are attributed to a reduced bending stiffness (Equation 4.3) of a thinner substrate. For a given film thickness, there will be increased curvature in a thinner substrate. For a thicker substrate, a thicker film is needed to generate enough bending moment to induce deformation. Also, the critical curvature for bifurcation (Equation 4.8) will decrease linearly as the substrate thickness is reduced. Thinner substrates will bifurcate earlier than thicker substrates yielding more dramatic displacements sooner. For 0.5 mm thick samples, the critical curvature for bifurcation is 19.0 m^{-1} giving a displacement of about 0.9 mm. This is approximately where the displacement curves for the 0.5 mm samples begin to increase in slope, agreeing well with the calculation.

The displacement of the 1.27 mm samples is much closer to the 1.5 mm samples than the 1.0 mm samples (Figure 7-5), where it should be expected to be more equidistant between the two. The displacement rate of the 0.75 and 1.27 mm samples also appear to

be slightly depressed (Figure 7-6). Indeed, the displacement rate for 1.27 mm samples was 0.15 mm h^{-1}, virtually the same as the 0.14 mm h^{-1} for 1.50 mm samples. The reason for this is that these samples were harder as the raw material came from a different vendor (ESPI Metals) than the other three thicknesses (Alfa Aesar). The hardness of the ESPI samples were measured by an independent vendor to be 40% greater than the Alfa samples, $HV = 38$ kg mm^{-2} versus $HV = 27$ kg mm^{-2}. In the analytical model, this will increase the effective plastic moduli of the substrate by a similar amount, decreasing the curvature (Equation 4.4) and subsequently the displacement (Equation 4.5). The displacement difference predicted by the model varies slightly depending on the exact curvature, but can be approximated to be directly proportional with the curvature difference. Therefore, the displacement rate of the ESPI sample is expected to be 40% less than the displacement rate of an Alfa sample at the same thickness. If the displacement rates vary linearly with substrate thickness, the expected displacement rate for 1.27 mm samples, extrapolated from the 1.0 and 1.5 mm sample data, is 0.30 mm h^{-1} but the measured displacement rate is 0.15 mm h^{-1}, 50% less. The predicted drop of 40% would result in a 0.18 mm h^{-1} displacement rate. While this 50% difference from the expected displacement rate is slightly greater than the 40% prediction, it is reasonably close considering the resolution of the measurement and that model was developed for an unrestricted, open cell sample.

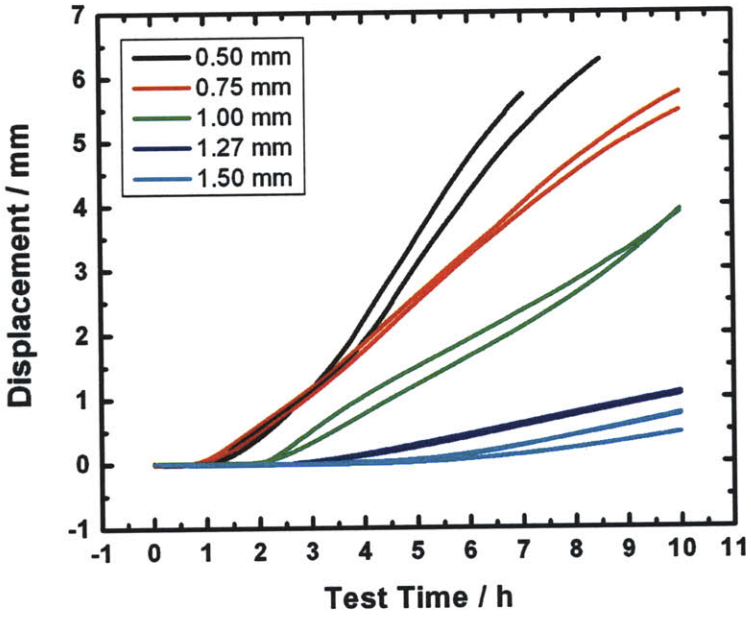


Figure 7-5. Displacement curves for aluminum-based disc actuators of different thickensses. Thinner samples show increased displacement and less incubation.

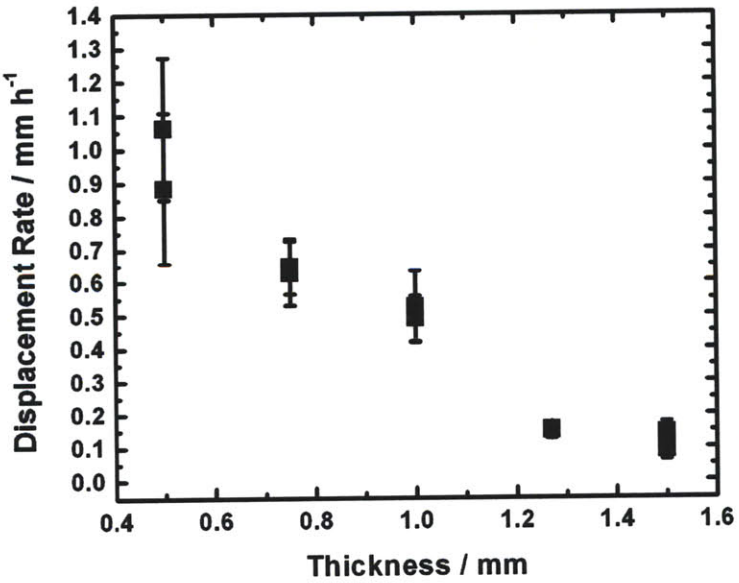


Figure 7-6. Average displacement rate after incubation for aluminum-based disc actuators of different thicknesses.

As for the incubation capacity, a thicker sample requires a larger bending moment in order to initiate displacement. This occurs as the intermetallic film grows thicker and varies as the product of $h_f h_s$, both of which are changing at the same time. The nominal incubation capacities increase in ~5 mAh increments as the samples increase in thickness in 0.25 mm increments. A given moment, M, should induce a curvature, κ, of:

$$M = EI\kappa \tag{7.1}$$

Therefore, plotting the bending moment (Equation 4.1) versus the inertia (Equation 4.3, or bending stiffness EI) for the observed incubation capacities should result in a linear relation, which it does (Figure 7-7). We can use this equation of linear elasticity as the overall displacement is less than the thickness of the substrate at the end of incubation.

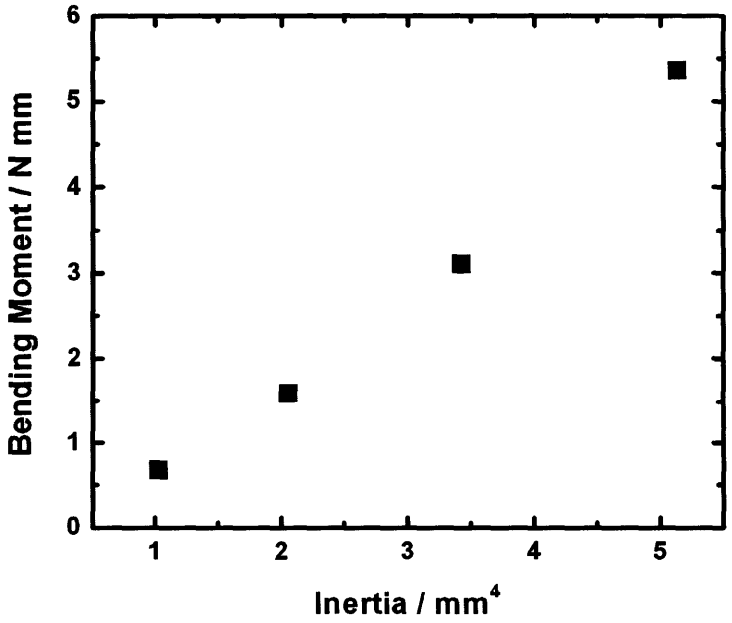


Figure 7-7. Bending moment versus inertia at the observed incubation capacity for aluminum-based disc actuators of different thicknesses. The linear trend verifies the increased bending moment needed to overcome the bending stiffness of the samples.

7.4 Summary

In this chapter, we have discussed three methods to control the displacement rate of a self-powered actuation device. Increasing the external resistance or introducing a duty cycle for a self-powered actuator can serve to decrease the displacement rate compared to a short-circuited sample by limiting the rate of discharge. Due to the magnitude of the internal impedance, varying the external resistance does not provide fine tuning of the displacement rate which drops from 0.5 mm h^{-1} to 0.02 mm h^{-1} going from 10 ohms to 325 ohms in a nonlinear fashion for an aluminum-based actuator. Using a duty cycle allows better control over the displacement rate, as the displacement rate varies linearly with duty cycle percentage between 33% - 100% duty cycle. At extremely low duty cycles, the displacement rate drops significantly from the duty cycle percentage. Some of the current must contribute to non-Faradaic processes due to the electrochemical relaxation afforded during the relatively long off state. Tin-based actuators have demonstrated a maximum displacement rate of 0.35 mm h^{-1} at 1.0 mm thick.

The displacement rate of aluminum-based actuators was shown to be inversely proportional to the thickness of the active element ranging from 0.14 mm h^{-1} for 1.50 mm thick samples to around 0.95 mm h^{-1} for 0.50 mm samples. Also, the bending moment needed to impart deformation was shown to be proportional to the bending stiffness of the samples. This led to increased incubation capacities for thicker samples. Finally, evidence was presented that harder samples show depressed displacements and displacement rates.

8 Future Directions

8.1 Intercalation Oxides and Graphite

Clearly the standard construction of a battery is not optimized for actuation purposes. The stacked and laminated constructions are amenable to manufacturing processes though. Dramatic changes, such as with the HOPG microactuator, are necessary to realize the full actuation potential of many of these materials. One of the drawbacks is the increased diffusion lengths in these monolithic structures which limits the bandwidth. Other constructions should be investigated in order to determine if high bandwidth and large strains can be realized simultaneously. One direction may be to use dense thin films with a solid electrolyte layer. Thin film batteries have been tested as actuators, however the actuation mechanism was lithium plating and the battery failed at low stresses due to the weak construction.[1]

More in-depth testing with other battery electrode materials may also prove fruitful. The battery community is primarily interested in electrical energy and power with size and weight constraints. Some materials that may be useful for actuation may have been overlooked or dismissed in the current literature.

8.2 Metal Alloying

In the case of metal alloys, the self-amplified design has shown to be advantageous for achieving very large displacements. The substrate geometries tested have been quite limited though. Even within the controlled folding rectangular geometry, it would be interesting to determine the effects of changing the width of the reaction area and changing the length of the lever arms.

More rigorous and systematic testing of the effects of material properties on the actuation behavior should also be pursued. In particular, cold-working the aluminum to different states of hardness should impact the observed incubation and the displacement rate by changing the effective Young's modulus used in the plastic deformation model. We have already seen deviations from expected results from using aluminum of different hardness during the testing of actuators of different thicknesses. Using other materials with different moduli and yield strengths would also go a long way in verifying the analytical model.

On a microstructural level, the effects of discharge rate lead to more questions. A galvanostatic study to different depths of discharge (similar to the self-powered 'quench' study) would lend more insight to the microstructural evolution of the intermetallic film. In addition, in-situ x-ray diffraction could shed light on the cause of increased displacement and reduced impedance seen at higher currents. Similar to the work-hardening variations above, it would be interesting to systematically vary the grain size of the starting aluminum to see if that had effects on the feature dimensions of the intermetallic film. Other characterization techniques, such as inductively coupled plasma (ICP) mass spectrometry could be utilized to determine if there were any composition gradients within the intermetallic film which has been observed.[2,3]

Similar to the commercial battery situation, the current construction of these devices puts soft material in series with the active element in the actuation direction. While the displacements are very large and should overwhelm the creep from the lithium and separator, it may also be useful to use a construction similar to the HOPG actuators

where the soft materials are removed from the actuation axis in order to achieve slightly better actuation, more on the level of the open cell actuators.

Finally, a finite element model could be developed to better understand the actuation mechanism of these devices. This would further aid the prediction of the effects of numerous variables on the actuation properties. Numerical methods have been developed to predict curvature due to mismatch strains for thin films on substrates.[4-6] Modifying these models to apply to the system under consideration would certainly be beneficial. In order to validate these models, it would also be useful to implement a large-scale curvature measurement technique and determine the curvature variations across the diameter of a cell. This would likely need to be done with a cell post-mortem in order to measure the curvature of the active element itself in case the packaging isn't conformal.

8.3 References

1. Barvosa-Carter, W. et al. Solid-state actuation based on reversible Li electroplating. *Smart Structures and Materials 2005 - Active Materials: Behavior and Mechanics, Mar 7-10 2005* **5761**, 90-97(2005).
2. Garreau, M. et al. Cycling behavior of lithium and aluminum-lithium electrodes in propylene carbonate and dioxolane electrolytes. *Proceedings of the workshop on lithium nonaqueous battery electrochemistry* **80-7**, 158-180(1980).
3. Epelboin, I. et al. Behavior of secondary lithium and aluminum-lithium electrodes in propylene carbonate. *Journal of the Electrochemical Society* **127**, 2100-2104
4. Fruend, L. Substrate curvature due to thin film mismatch strain in the nonlinear deformation range. *Journal of the Mechanics and Physics of Solids* **48**, 1159-1174(2000).
5. Giannakopoulos, A. et al. Elastoplastic analysis of thermal cycling: layered materials with compositional gradients. *Acta Metallurgica et Materialia* **43**, 1335-1354(1995).
6. Masters, C. & Salamon, N. Geometrically nonlinear stress-deflection relations for thin film/substrate systems. *International Journal of Engineering Science* **31**, 915-925(1993).